PLASMA CHARACTERIZATION OF A SINGLE AND DOUBLE SPLIT RING RESONATOR FOR MICROPROPULSION

by

ROBERTO DEXTRE

A DISSERTATION

Submitted in partial fulfillment of the requirements
for the degree of Doctor of Philosophy
in
The Department of Mechanical and Aerospace Engineering
to
The School of Graduate Studies
of
The University of Alabama in Huntsville

HUNTSVILLE, ALABAMA

2018

In presenting this dissertation in partial fulfillment of the requirements for a doctoral degree from The University of Alabama in Huntsville, I agree that the Library of this University shall make it freely available for inspection. I further agree that permission for extensive copying for scholarly purposes may be granted by my advisor or, in his/her absence, by the Chair of the Department or the Dean of the School of Graduate Studies. It is also understood that due recognition shall be given to me and to The University of Alabama in Huntsville in any scholarly use which may be made of any material in this dissertation.

Roberto Dextre Date

DISSERTATION APPROVAL FORM

Submitted by Roberto Dextre in partial fulfillment of the requirements for the degree of Doctor of Philosophy in Aerospace Systems Engineering and accepted on behalf of the Faculty of the School of Graduate Studies by the dissertation committee.

We, the undersigned members of the Graduate Faculty of The University of Alabama in Huntsville, certify that we have advised and/or supervised the candidate on the work described in this dissertation. We further certify that we have reviewed the dissertation manuscript and approve it in partial fulfillment of the requirements for the degree of Doctor of Philosophy in Aerospace Engineering.

Dr. Kunning G. Xu	Date	Committee Chair
Dr. Kurt Polzin	Date	
Dr. Robert Frederick	Date	
Dr. David Landrum	Date	
Dr. Jason Cassibry	Date	
Dr. Keith Hollingsworth	Date	Department Chair
Dr. Shankar Mahalingam	Date	College Dean
Dr. David Berkowitz	Date	Graduate Dean

ABSTRACT

The School of Graduate Studies
The University of Alabama in Huntsville

Degree ____Doctor of Philosophy_________ College/Dept. Engineering/Mechanical and Aerospace Engineering

Name of Candidate______Roberto Dextre_______________________________________

Title Plasma Characterization of a Single and Double Split Ring Resonator for Micropropulsion

Split Ring Resonator (SRR) devices are based on microstrip technologies that are capable of producing small-scale plasmas, i.e. microplasmas. Multiple configurations exist for the production of microplasma, the microstrip has proven to be a low-power, low-cost, easily adaptable design for implementation into a satellite micropropulsion system. Various acceleration schemes exist for plasma-based micropropulsion systems for small satellites. In this work, electrostatic acceleration is considered for the thruster. Theoretical calculations for electrostatic acceleration mechanisms are examined with SRR microplasma sources. In this work, the microplasma properties from a single split-ring resonator and a concentric split-ring resonator are characterized. The microplasmas were generated in low pressure argon as low as ~350 mTorr-Ar and ranging from 4.7 to 11 W microwave power. Simulations of the SRR-generated electric fields were performed to understand the electric field intensity and vector behavior of the devices. Single and double Langmuir probe measurements were used to determine the plasma properties. This research also utilized a 2D spatial contour plot to understand the distribution of the plasma properties. For the purpose of electric propulsion we seek to understand how to improve the SRR and Concentric SRR (CSRR) to determine the maximum possible electron temperature and plasma densities while obtaining a uniform plasma property distribution. Compared to the single ring, the concentric ring showed an increase in peak electron temperature from 8.2 eV to 9.5 eV. A different trend was observed for the plasma number density as the concentric device recorded a peak density of 1.2 x 10^{17} /m^3 while the concentric device obtained 8.5 x 10^{16} /m^3. The 2D spatial distribution plots along with electric field simulations show the induced coupling effect of the CSRR caused increased electron temperature and increased uniformity in the spatial profiles of electron temperature and plasma density. The driving frequency of the concentric split-ring resonator source was also varied to determine the effects of the change in operating frequency on the microplasma properties. An operational frequency was experimentally found to be 796 MHz and the device was additionally tested at ±10 MHz. A simulation of the electric field was performed to understand the behavior in the device. The results show multiple peaks in plasma properties due to the effect of the nested ring. The electron temperature when operating at the resonant frequency, -10 MHz, and +10 MHz, was found to be 9.5, 8.5, and 7.6 eV, respectively. Different trends were observed for the plasma property distributions as the concentric device was operable with two points of ignition due to the coupling effect of the fringing electric fields. Results of this research and continuing research can show if this technology has a competitive advantage over other current micropropulsion systems today.

Abstract Approval: Committee Chair

Dr. Kunning G. Xu

Department Chair

Dr. Keith Hollingsworth

Graduate Dean

Dr. David Berkowitz

ACKNOWLEDGEMENTS

The work described in this thesis would not have been possible without the assistance of a number of people who deserve special mention. First, I would like to thank Dr. Gabe Xu for his suggestion of the research topic and for his guidance through the stages of the work. Second, the other members of my committee have been very helpful with comments and suggestions. Dr. Emmanuel Waddell with the LSAMP and Adriel Johnson Fellowship program also deserves special thank you for the support throughout my academic career. NSF EPScOR CPU2AL also deserves a special thank you for its financial support to help me obtain this degree.

I would also like to thank my family and friends who encouraged me to begin work on this degree. I’d like to thank my girlfriend, Diana Zorzon, for pushing me and stressing me out in the same time. I love you and your craziness. Thank you to Baila Huntsville and the salsa community for giving me the best kind of stress relief possible through dance and friendships. You guys are the real heroes! Thank you to my friendships from my alma mater, Binghamton University. I miss you guys and I think it’s obvious to say that without my Bachelor’s in Mechanical Engineering, this wouldn’t be possible. I’d also like to thank Ryan Gott for all of the quotes in the beginning of my chapters. I stole all of them from your thesis, sorry. The PERL undergraduates and graduates, all of you played a role into helping me complete this dissertation. Thank you! I wish all the best for the future of PERL students. Peace, I’m out! *mic drop*

TABLE OF CONTENTS

LIST OF FIGURES

LIST OF TABLES

NOMENCLATURE

3MT = Microwave Microplasma Microthruster
A = Probe area
A_2 = Exit Area
c = Speed of light
EP = Electric propulsion
e = electronic charge
F = Thrust
f = Frequency
I_0 = Electron Saturation Current
I- = Ion Saturation Current
HFSS= High Frequency Structure Simulator
k = specific heat ratio
K = Boltzmann Constant
$\dot{m}$ = Mass Flow Rate
m = electronic mass
M = ion mass
n_e = Electron number Density
n = Ion number density
p_1 = Chamber Pressure
p_2 = Exit Pressure
p_3 = Reservoir pressure
Pd = Pressure-distance product
Q = Quality Factor
RF = Radio frequency
R = Gas Constant
SRR = Split Ring Resonator
T_1 = Chamber Temperature
v_2 = Exit Velocity
Z_{in} = Input Impedance
Z_0 = Characteristic Impedance
$\mathrm{I_{SP}}$ = Specific impulse
λ = Wavelength
ε_r = Dielectric Constant
θ = Phase Offset Angle
α = Attenuation Factor
λ_D = Debye Length
λ_{mfp} = Ion-neutral Mean Free Path
α_c = Collisionality Factor
φ = DC potential

Chapter 1.

Introduction

> *A simple intuition, a single observation, can open vistas of unimagined potential. Once caught in the web of an idea, the researcher is happily doomed, for the outcome is always uncertain, and the resolution of the mystery may take years to unfold.*
>
> \- Wade Davis

This dissertation aims to understand the formation of microplasmas with split ring resonators (SRR). A variety of characteristics of a SRR can impact the microplasma properties and this research seeks to understand how certain physical and operational parameters of the SRR affect the microplasma. When designing a SRR, a few factors need to be considered. The dielectric constant and thickness, the geometric characteristics of the microstrip structure, gap width, and angle placement are all factors that can dramatically impact the microplasma. Some of these factors have been studied by other researchers, but a complete understanding is still missing. In particular, this research seeks to understand the effect of the ring width, addition of a nest ring, and off-resonant operation on the resulting microplasma for application to a plasma microthruster. While the overall research is geared towards a new in-space micropropulsion device, this dissertation is more concerned with the physics and behavior of the plasma produced by the SRRs. A better understanding provided by this research can prove useful for improving the microplasmas produced by the SRR for micropropulsion and terrestrial applications.

1.1 Micropropulsion and Plasma Propulsion Overview

Rocket propulsion or thruster systems can be classified based on the energy source, propellant, and acceleration mechanism. The energy source can vary between chemical, electric, or nuclear while the propellant can vary between solids, liquids, and gaseous propellants [1]. The primary difference between plasma-based and chemical-based propulsion is the energy source. Chemical engines rely on chemical reactions, generally exothermic combustion, to generate energy for acceleration. They are thus limited in performance by the chemical energy stored in the molecules. Electric propulsion (EP) decouples the propellant chemistry from the acceleration mechanism with the use of an external energy source for acceleration. EP devices can thus deliver higher acceleration. The acceleration mechanism or method of producing thrust in EP thrusters includes electrothermal, electromagnetic, and electrostatic acceleration.

Electrothermal propulsion is similar to chemical rocket propulsion. For both, thrust is produced by accelerating a hot gas through a converging-diverging nozzle. The primary distinction between electrothermal and chemical rockets is the heat source. In electrothermal propulsion, the propellant is heated electrically with a resistor, arc, or other plasma source before it is thermodynamically expanded and accelerated out of the exhaust nozzle [2]. In chemical rockets, combustion of the propellant produces the hot gas which is accelerated through the nozzle. Electrostatic propulsion uses externally applied high electric fields to accelerate the charged particles in the plasma to high velocities (~4 km/s) [1]. This can be accomplished with the use of a screen-accelerator grid system, commonly implemented in ion engines. For electromagnetic propulsion, the Lorentz force is used to accelerate the plasma, which requires both electric and magnetic fields [3].

For micropropulsion systems, specific impulse (I_{SP}) is an especially important performance parameter. Specific impulse is a measure of efficiency of propellant consumption, similar to miles-per-gallon in automobiles. A high I_{SP} is desirable for efficient operations, particularly with size-limited spacecraft using limited propellant storage. The I_{SP} can vary depending on the configuration of the device. For a resistojet, the I_{SP} can range from 150 s to 330 s, but for an ion engine, the I_{SP} can range from 1600 – 5000 s. Both resistojets and ion engines are classified as EP thrusters, but the ion engine generates a plasma. Figure 1 shows the regions of propulsion system performance capabilities and it shows the different thrust and I_{SP} ranges of different types of EP thrusters [1]. From the figure, an electrostatic type would be best for high I_{SP}, low thrust requirements, while an electrothermal type thruster would be the opposite.

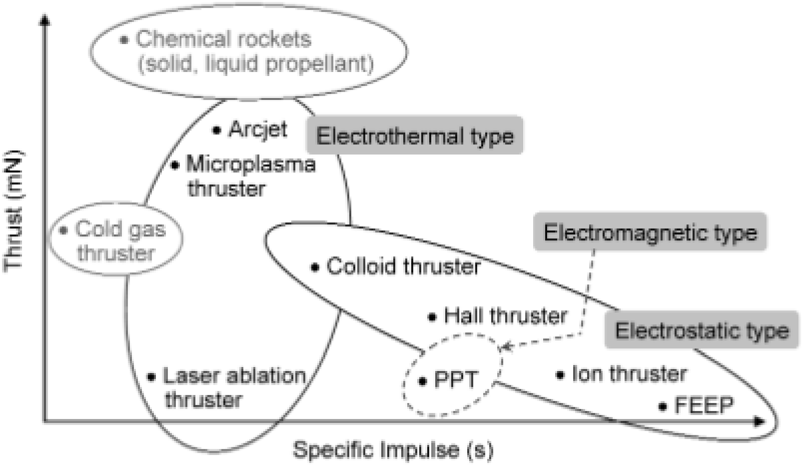

Figure 1. Regions of propulsion system performance capabilities [1].

Plasma propulsion utilizes a quasi-neutral plasma. Quasi-neutral refers to the balance between the positive and negative charges in the plasma [4]. Some methods to generate the plasma include the utilization of DC, pulsed DC, AC, RF, and microwave energy [3]. This research seeks to study the production of the microplasma in a split-ring resonator via microwave power for potential implementation as a micropropulsive device. The capabilities of the sources and thruster designs presented here potentially have a competitive advantage over existing devices. In order to improve the performance of the thruster, the behavior and relationship between the split-ring resonator source and the generated microplasma must be understood.

1.2 Applications in Small Satellites

Miniaturized spacecraft have recently attracted increased attention around the world. With the utilization of small satellites, overall mission costs can decrease and the launch rates can increase. Smaller spacecraft also have simpler structures, systems, and design requirements which can lead to shorter development periods. To be fully comparable and have the same capabilities as large spacecraft, the propulsion system also needs to be miniaturized and implemented into a small satellite.

Spaceworks’ 2018 forecast details the nano/microsatellite market by recording observations or trends in the past year. One of the projections included in the report stated that as many as 2,600 nano/microsatellites will require launch over the next 5 years. This projection is higher compared to previous years due to an increase of small satellite launch opportunities. Figure 2 shows the history and forecast of nano/microsatellite launches per year. The trends reflect the growing interest in small-satellites due to their compact and robust design and capabilities to accomplish a variety of commercial and scientific missions. These trends also indicate the potential need for improved nano/micropropulsion systems.

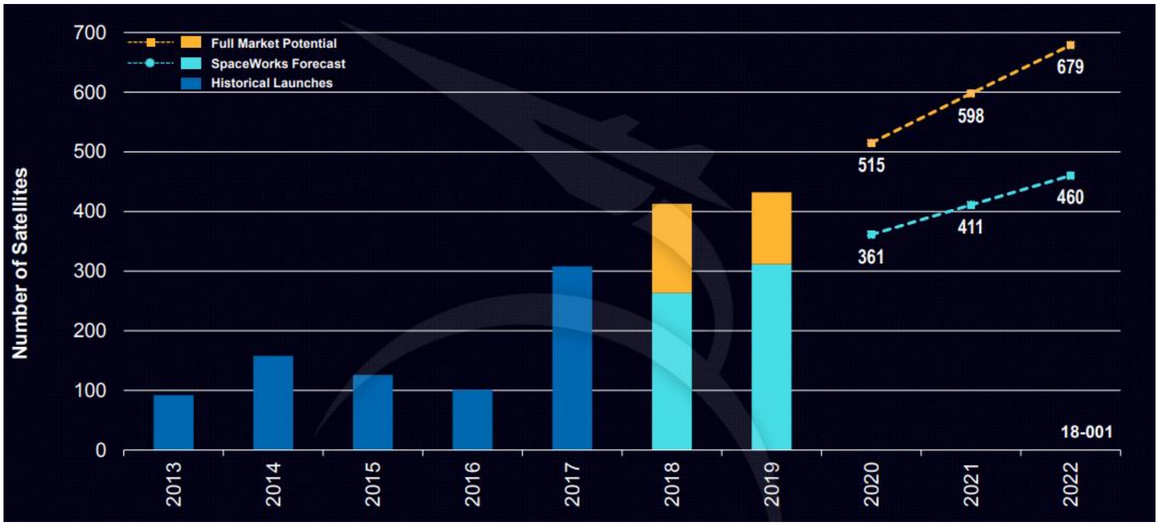

Figure 2. 2018 Nano/Microsatellite Launch History & Market Forecast (1 - 50 kg)[5] **.**

Rocket Lab is a small company that is developing small launch vehicles for the launch of small satellites. Rocket Lab’s mission focuses on increasing commercial space availability by providing frequency launch opportunities to low Earth orbit (LEO). NASA’s Space Launch System (SLS) is also configured to launch small satellites in Engineering Mission (EM) 01 and is planned to carry 13 small satellites. These launch provides give companies and/or universities opportunities to conduct research experiments with small satellites. In some cases, propulsion requirements are needed for these missions and may be achievable using the research presented in this dissertation.

Small satellites require thrust capabilities within the µN to mN range in order to perform objectives such as station-keeping or attitude control. Cold-gas thrusters have fulfilled these roles for existing small satellites due to their simplicity and proven capabilities. However, cold-gas thrusters have low specific impulse, ranging from 40 – 80 s. Thus, EP has an advantage over cold-gas thrusters for miniature satellites due to their very high specific impulse, up to 5000 s. With high I_{SP}, a lower propellant mass is required for the same change in velocity required for the mission. Maintaining a low propellant mass is an important factor when considering the development of a small satellite. While the thrust is low, the total impulse from an EP device can be very high as it can be applied for a long period of time[1]. However, this feature is only useful for deep space missions while the thruster operates continuously. High I_{SP} and low propellant mass makes EP preferable for small maneuvers and long duration use. However, some disadvantages for electric propulsion include the need for a separate dedicated power source. This leads to an increase in mass and complexity when delivering power to the propulsion system. Also, any maneuvers that require a fast response time would be disadvantageous for an electric propulsion device. With such a high I_{SP}, an increase in spacecraft velocity through applying low thrust and small acceleration can be achieved, but only after a long time.

The potential for an improved micropropulsion system exists. Various microthrusters have been proposed for station-keeping and attitude control applications including microelectric propulsion systems or microplasma/ion thrusters. This research studies the capabilities of a resonator microstrip device and its potential application as a microplasma source for a microplasma thruster device.

1.3 Problem Statement

The objective of this research is to study the generation of low power microwave microplasmas with SRRs and understand the fundamental relation between the resonator design and the microplasma properties. The application goal of this research is to implement the resonator and microplasma in a micropropulsion system. The SRR has proven effective for a variety of microplasma devices in the literature. The SRR has a small discharge gap, approximately 500 μm, where the plasma is generated. Figure 3 provides an example of an SRR device used in this research. The device shown has proven capable of ionizing microplasmas within the designated discharge gap.

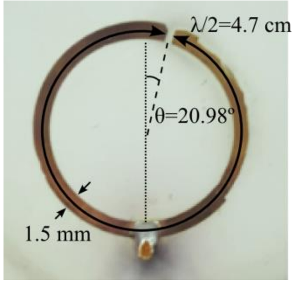

Figure 3. Example of split-ring resonator device used.

This ignition occurs as the electric field is concentrated within this gap to induce ionization at wavelengths greater than the circumference of the ring. The energy expended in producing the microplasma should correlate to the energy inputted from the device, as explained in the following sections. By understanding how these factors impact the microplasma properties, we can control them for efficient thrust production in a micropropulsion device.

1.4 Research Contribution

Previous work has shown that split ring resonators are capable of generating high plasma densities with very little power [6]. Characterizing a plasma produced by different types of microstrip resonators can open possibilities for new and improved plasma sources. This research utilizes different designs for microstrip resonator microplasma sources. With a change in geometry in the resonator, impedance and resonant frequency changes are observed. This can lead to plasma characteristics, such as volume, temperature, and density to be affected. Operational changes, such as frequency impacts the oscillations of the particles exposed to the electromagnetic field emitted from the resonator. This leads to changes in properties such as the plasma number densities. The contribution of this research mainly focuses on the behavior and physics of the plasma properties produced corresponding to the geometric and/or operational parameters changed. This is to help understand the behavior of these resonator structures and the impact induced on the microplasma generated.

One of the main differences among the resonator devices will be the geometric characteristics of the microstrip structure on the substrate. Previous work has shown the utilization of a simple ring design while changing the thickness of the ring, adding multiple rings [7], linear microstrips [8], different gap placements and gap widths [7]. Geometrically, this dissertation focuses on the addition of a nested concentric ring and the change in ring width. Operationally, this dissertation focuses on varying the frequency of the microwave signal and seeing the impact of off-resonant operations on a microplasma. New understanding of microplasmas and microstrip structure behavior can be achieved as we analyze the plasmas generated using these resonators. The focus of this dissertation is to see what different kinds of microplasma formations can be produced and how microstrip structures correspond to the plasma properties observed.

With this research, there is increased potential for implementation into micropropulsion technology. If these microstrip structures show a competitive advantage based on the cost-effectiveness and adaptability into electric propulsion, it is likely these microplasma microstrip resonators can lead the new wave of micropropulsion technologies. These devices can lead to a more marketable solution with the added capability of being a scalable device. It can also provide a desirable solution to extend the lifetime of various propulsion systems, due to minimal electrode erosion [9]. This includes the miniature propulsion system used for small satellites. Power efficiency is also increased as this technology requires less than 10 W to operate. This technology would increase maneuverability of spacecraft and expand the range of operation [1]. Furthermore, scaling up from this technology is possible; therefore, this can lead to quick and significant improvements in small satellite capabilities.

Chapter 2.

Background

There is not a discovery in science, however revolutionary, however sparkling with insight, that does not arise out of what went before. – Isaac Asimov

2.1 Plasma and Plasma Properties

Plasma is generated when gas is heated sufficiently to induce ionization. Ionization is a process that involves the conversion of neutral particles into charged particles (positive or negative). Plasma mainly consists of positive ions, negative ions, and electrons. During ionization, energetic electrons collide with neutral atoms and typically removes one of the neutral atom's valence electrons, creating a positive ion and two free electrons. The free electrons are further energized by an external electromagnetic field leading to a cascade of ionization collisions within the gas. This leads to an equal amount of positive and negatively charged particles being produced. Therefore, plasmas are considered electrically neutral on the macroscopic scale (referred to as quasi-neutrality) [4]. Plasmas exhibit some properties similar to gases; however, plasmas are electrically conductive and are affected by external electric and magnetic fields. Also, plasmas can cover a wide range of pressures, temperatures, and plasma densities. Microplasmas refer to the generation of plasmas occurring on a small scale, on the order of millimeters or smaller.

Gas discharge plasmas are commonly used for applications such as light sources, plasma display panels, and lasers[10].

2.1.1 Electron Temperature

Since many terrestrial plasmas are typically in a non-thermodynamic equilibrium state, there can be different temperatures for different groups of particles (electrons, ions, neutrals). Electron temperature is often the most important temperature in plasma discharges because it defines the electron kinetic energy [11]. Due to the small mass of electrons, they have velocities orders of magnitude larger than the heavier ions and neutrals, thus are responsible for most interactions and reactions. Some corresponding parameters that depend on the electron temperature are the electron energy distributions, electron current, and Debye length. The electron's energy affects the ability of the electrons to produce reactions such as ionization. For example, the 1st ionization energy of an argon atom is 15.76 electron-volt (eV). This means for electron impact ionization of an argon atom to occur, the colliding electron must have at least an energy/temperature of 15.76 eV (1 eV = 11,600 K). In practice, the actual minimum electron temperature to ionize argon is 5-10 times higher due to losses.

2.1.2 Electron and Ion Density or Plasma Number Density

Another standard plasma property is the plasma number density, which represents the number of charged particles/m^3. The plasma density can be divided into ion and electron number density as the two may be different. Quasi-neutrality requires that the overall ion number density, n_i, and electron number density, n_e, are the same; but locally that may not be true. With the assumption of quasi-neutrality, the electron and ion densities can be considered equivalent and are often just called the plasma density [12]. A higher plasma number density means an increased presence of charged particles in a unit volume.

2.2 Microplasma

Microplasmas are a regime of plasmas produced at the millimeter or smaller (micron) physical scales, thus micro-plasma. The physical scale of a microplasma distinguishes it from other larger plasmas. Regardless of the size of the plasma produced, the plasma properties are still the same; however, some of the operating conditions can differ. Microplasmas are produced in both vacuum and high-pressure conditions. The power sources for microplasmas can include direct current (DC), pulsed DC, alternating current (AC), radio frequencies (RF), or microwave sources. This research uses microwave excitation to produce low power microplasmas. The discharge type used in this work is a glow discharge. This particular discharge occurs when a breakdown voltage is achieved between electrodes and current passes through a gas. This is distinct from other discharges such as Townsend discharges, which are dominated by emission from neutral atoms exposed to free electrons accelerated by an electric field [13]. In order to produce a stable glow discharge, the pressure-distance (Pd) product must be within a certain range [14]. The applications for microplasmas include bio-MEMS sterilization [15], small-scale materials processing [16], microchemical analysis [17], an excitation source for sensors and chemical analysis [10], [14], remediation of volatile organic compounds [10], [14], synthesis of nanomaterials [10], [14], [18], bacteria sterilization [19], skin tissue treatment [20], surface activation, thin film coating [10], and electric propulsion [1].

2.2.1 PD Scaling

The characteristics of microplasma glow discharges depend on the pressure-distance product which describes the dimensions of the cavities needed in order to spatially confine plasmas. This concept can be described under Paschen's law,

$$V_B = \frac{Bpd}{\ln(Apd) - \ln\left[\ln\left(1 + \frac{1}{\gamma_{se}}\right)\right]} \tag{1}$$

which entails the breakdown voltage required under varying pressures and distances between two electrodes.

Here, V_B is the breakdown voltage, p is the pressure, d is the distance between the electrodes, γ_{se} is the secondary electron emission coefficient, A is the saturation ionization in the gas, and B corresponds to the excitation and ionization energies. The graph of Equation (1) is known as Paschen's curve shown in Figure 4. The curve shows that changing the pressure-distance (*pd*) product impacts the required breakdown voltage to achieve ionization. At low *pd*, the high breakdown voltage is due to the decreased amount of ionizing collisions at low pressures and/or smaller distances. If the *pd* product is closer to or smaller than the mean free path of the electron-neutral collisions, the number of collisions between the electrodes decreases. At high *pd* scales, increased collisions occur. With each collision electrons lose energy, thus reducing the odds of an ionizing collision, thus requiring higher breakdown voltages to ensure ionization to occur. However, since collisions are still occurring at higher *pd* products, only a gradual increase in breakdown voltage is observed.

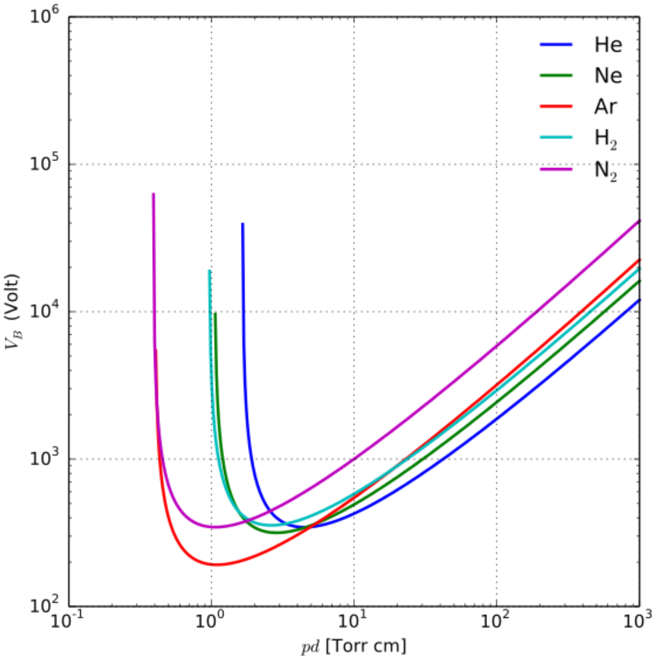

Figure 4. Paschen's Curve obtained for helium, neon, argon, hydrogen and nitrogen with breakdown voltage vs. the Pd product.[21]

Figure 5 shows Paschen curves developed by Iza and Hopwood[9] that compares the standard DC-Paschen curve with the microwave microplasma sources they developed. The DC-Paschen curve describes the breakdown voltage required when using direct current, in the same fashion as Equation (1) and Figure 4. It is noted that a lower breakdown voltage is required for the production of microplasmas compared to the normal DC-Paschen curve. In that work, Iza and Hopwood used a type of microstrip technology known as a split ring resonator (SRR) [9].

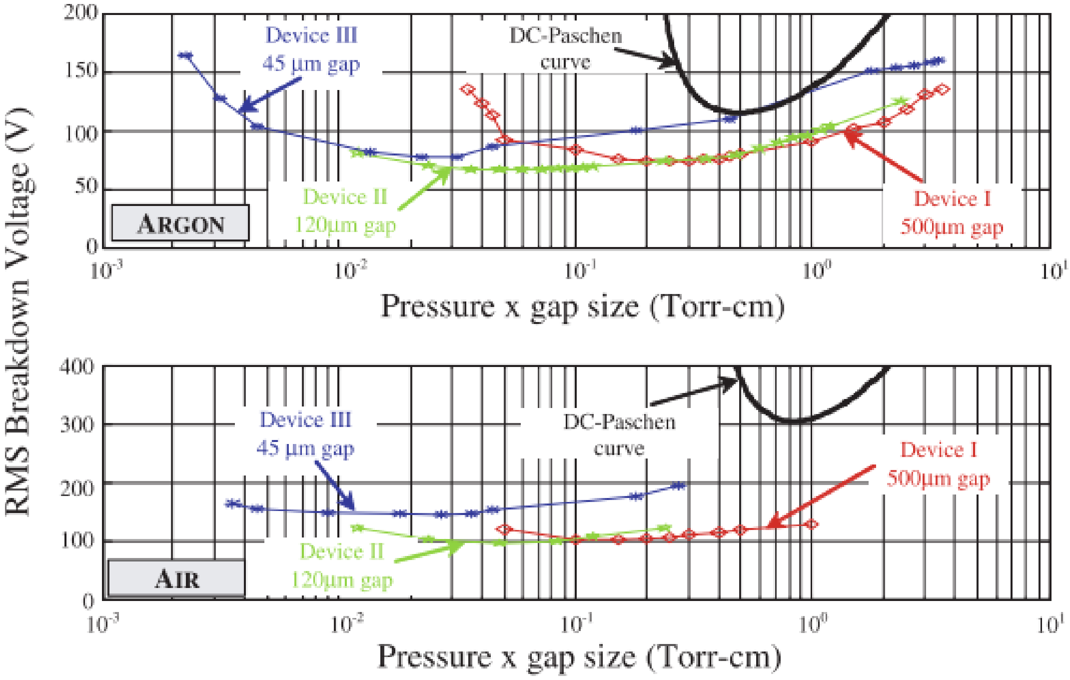

Figure 5. Pd scaling of microplasma devices developed by Iza and Hopwood compared to DC-Paschen curve [9]**.**

In Figure 3, Device I, II, and III all correspond to a different SRR. These devices are shown in Figure 6.

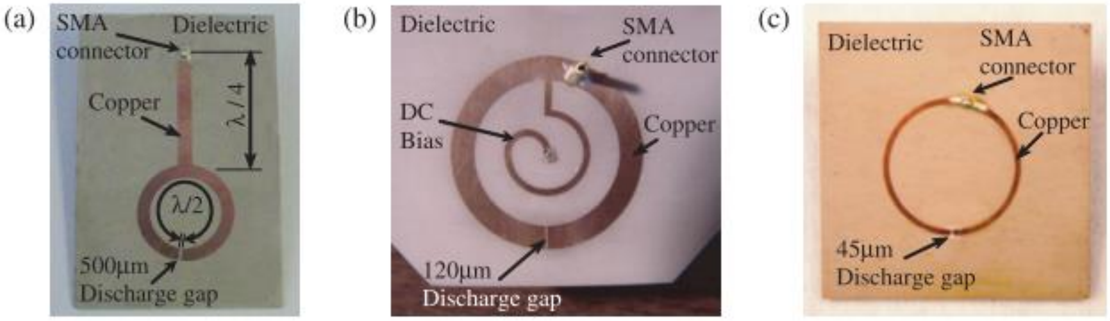

Figure 6. (a) Device I, (b) Device II, (c) Device III [9]**.**

Each SRR has its own distinct characteristics in geometry, impedance, and gap size. When comparing the Paschen curve of each device along with the DC-Paschen curve, it is apparent that Device I and II require the smallest breakdown voltages. This is mainly due to the larger amplitude of the electron oscillation during the ignition process compared to the gap size. This leads to higher voltage requirements for smaller gap sizes to compensate for the higher electron losses [9]. Regardless, all devices can produce a plasma with a lower breakdown voltage compared to the DC-Paschen curve. This shows that utilizing RF for microplasma production requires less voltage than DC.

2.2.2 Research in Microplasmas

Research in microplasmas has focused on the type of sources and configurations used. Ishii [22] and Yokoyama [23] classify three different types of microplasma source modes: the concentrated energy mode, space-limited mode, and mass-limited mode. In concentrated energy mode, the microplasma is generated using a concentrated high electric field at the tips of an electrode. Space-limited mode involves the limitations on the microplasma volume due to solid boundaries. Mass-limited mode involves an initial material such as a powder to initiate the microdischarge [22], [23]. Many configurations for producing microplasmas exist today [14]; however, microstrip-based microplasma was chosen for this research.

2.2.3 Linear Resonator

A microstrip is a conducting transmission line fabricated on a substrate of high dielectric constant and is often referred to as a linear resonator. The design is based on the quarter wavelength resonator which is intended to optimize the RF voltage difference across a discharge gap. This gap is formed between the resonator and a ground electrode. Figure 7 shows the microstrip line and plots the change in voltage with position along the microstrip [8].

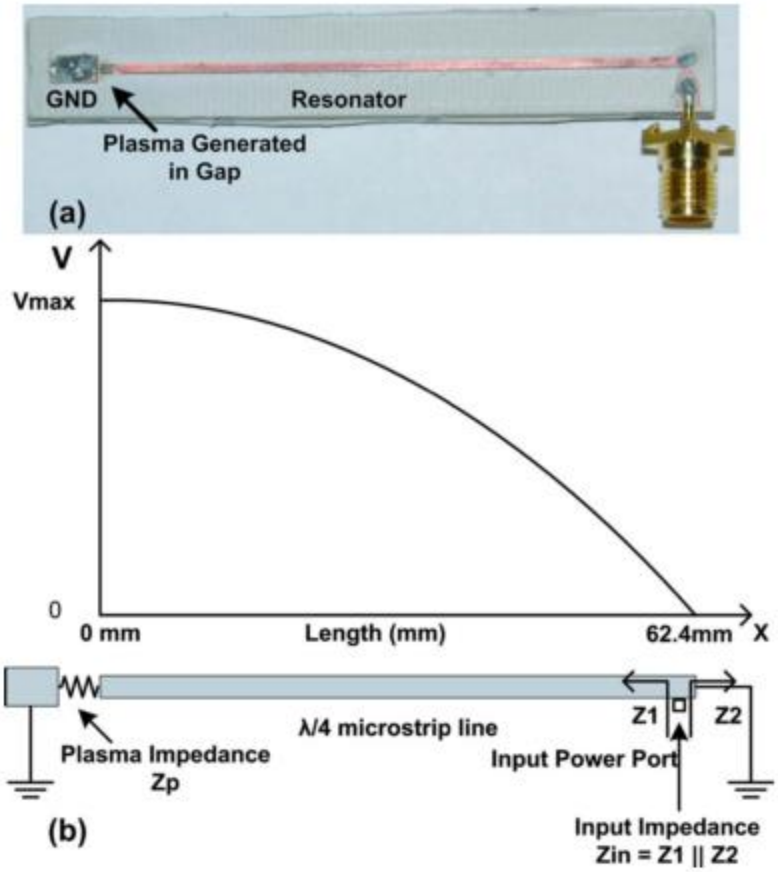

Figure 7. (a) Linear resonator microstrip device. (b) Voltage curve with respect to position on linear resonator [7] .

In Figure 7, the microwave power is connected directly to the resonator strip using an SMA input port shown on the right end. An important experimental design is the matching of the input impedance to the power supply impedance so that no matching network is needed. This impedance is commonly set at 50 Ohms by equipment standards. A range of frequencies can be utilized to develop resonator technology. The resonator shown in Figure 7 was designed at a resonant frequency of 473.9 MHz. Kim and Terashima [25] developed a microplasma source based on microstrip linear resonators that operated at 2.45 GHz frequency. It is important to note there is a shift in the resonant frequency after ignition due to the plasma impedance. Plasma impedance contains both resistive and capacitive components[9]. It is in the form of $Z_p = R_p + jX_p(\Omega)$. Here, Z_p represents the plasma impedance while R_p and X_p are the resistive and capacitive components, respectively. The impedance of the microplasma can be determined from the ratio of forward power to reflected power which can be described by a reflection coefficient labeled as, s_{11}. This is further described in Ref. [9]. When observing the reflection coefficient as a function of frequency, a minimum in the reflection coefficient, where the optimal forward power delivered to the microplasma, is found at the resonant frequency. After ignition, the resistive and capacitive components describing the plasma impedance shifts. With the change in the capacitance, the plasma impedance is affected along with the reflection coefficient behavior as a function of frequency. At this point, the peak reflection coefficient occurs at a new frequency differing from the original resonant frequency.

Another aspect of linear resonators that has been reviewed and utilized for the purpose of this research is the linear array structures developed by Zhang [8]. It has been observed that while powering one linear resonator, a coupling effect is induced on any linear resonators nearby. This effect leads to a propagation of the microplasma throughout multiple discharge gaps while only powering one resonator [8], [24]. Figure 8 shows this concept. With this observation, a similar concept is applied for the concentric ring resonator designs discussed later in this research.

Figure 8. Left resonator powered. Propagation of microplasma across linear array [8]**.**

2.2.4 Split Ring Resonator (SRR)

Similar to the linear resonator, a split ring resonator is a microstrip source constructed with a ring geometry. Proposed applications of the SRR microplasma source in the literature include small scale materials processing, micro-chemical analysis systems, and bio-mechanical system sterilization [10]. The SRR is a conducting ring with a small gap powered at microwave frequencies (0.3-300 GHz) [6]. The ring is designed for a specific resonant frequency and concentrates the maximum change in electrical potential within the gap. This leads to the ionization of the gas at the gap to generate the microplasma. SRRs can be easily and cheaply made using modern photolithography or circuit board milling techniques. An advantage of SRRs is its capability to operate at a range of wavelengths over the designed resonance configuration of the ring, allowing for frequency to control the plasma properties. At resonance, a peak in plasma temperatures and densities is obtained. Figure 9 is a split ring resonator developed by Hopwood showing the relationship between the ring and a stem used for impedance matching[14], [26].

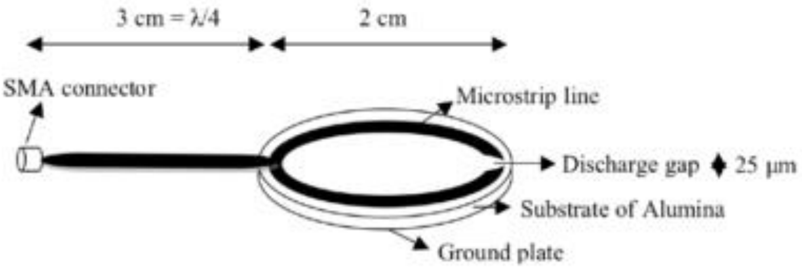

Figure 9. Split ring resonator device by Hopwood [26]**.**

Overall, the purpose of these devices is to produce a desired electromagnetic response. Within the structure of the resonator, the electromagnetic flux induces oscillating currents, which follow the geometry of the resonator until it reaches the discharge gap. This leads to an incident field that is dependent on the linear or SRR resonant properties. An advantage of resonator technology is the ability to allow the device to support resonant wavelengths other than the geometry of the ring. Similar to Figure 7, the peak potential found at the edge of linear resonator shown may be more than what is required to achieve ionization. This would essentially expand the operating frequency of the resonator [26]; however, this trades off with the power required to operate the resonator. At off-resonant frequencies, more power is required. A second advantage of the SRR is its more compact structure compared to a linear resonator at the same frequency. This makes SRRs well-suited for small volume plasma generation such as in microthrusters. SRRs can also generate higher plasma densities with less power than linear resonators [9]. The SRRs can operate over a wide range of frequencies, though the size of the ring shrinks significantly at very high frequencies and fabrication may become difficult.

In order to achieve ignition, the discharge gap potential of the SRR must be high enough to induce ionization. This can be described by a gap voltage equation developed by Iza [9]. This is given as,

$$V_{gap} = 4\sqrt{\frac{Z_o Q}{\pi}}\sqrt{P_{in}} \tag{2}$$

Here, Z_o is the characteristic impedance, Q is the quality factor, and P_{in} is the input power. Typically, this occurs at the resonant frequency where the magnitude of the electric field in the discharge gap is optimal [27]. When operating at the resonant frequency, the impedance of the microwave system and microplasma source should match. This allows the corresponding microwave signal to deliver the maximum amount of power to the device and minimize any signal reflection [28].

The dielectric constant of the substrate on which the microstrip structure is built on affects the resonant frequency of the resonator. The dielectric constant is also called the relative permittivity, a material property that describes the ability to store electrical energy in an electric field. A good electric insulator with high dielectric constant is desired to minimize any leakage of current from the microstrip.

2.2.5 SRR Microplasmas

Iza and Hopwood in 2003 [6] built a low-power microwave SRR microplasma source to operate at 900 MHz from 0.05 Torr up to 760 Torr. The microplasma discharges were self-started with less than 3 W of power and atmospheric discharges were sustained at 0.5 W using argon. The design was fabricated on a RT/Duroid 6010.8 with a dielectric constant of 10.8. A high dielectric constant was used because an increase in dielectric constant leads to a decrease in the wavelength of the microwave signal passing through the device which can lead to a more compact resonator structure. The equation describing this relationship between wavelength and dielectric constant is written as, $c=\lambda f\sqrt{(\varepsilon_r)}$. Here c is the speed of light, λ is the wavelength, f is the frequency, and ε_r is the dielectric constant. The microstrip pattern was created using photolithography and wet etching techniques and an SMA connector was attached perpendicular to the microstrip line. The dimensions of the design correspond to the frequency utilized and the wavelength of the microwave input. However, the thickness of the ring is a parameter that has not been mentioned and was studied in the research in this dissertation. Their microplasma source produced an ion density of 1.3 x 10^{17} /m^3 at 400 mTorr while consuming 0.5 W.

Further work by Hopwood and Iza in 2005 [26] studied an SRR microplasma source designed specifically for operating in air. The resonant frequency of this device was 895 MHz and it was fabricated on an alumina oxide substrate with a dielectric constant of 9.8. The heating of the alumina oxide substrate caused a downward shift in the resonant frequency. This brings up an interesting question in regards to dependency of the resonant frequency on the thermal properties of the material. One design aspect shown in Figure 10 that is different from Iza and Hopwood’s previous designs is this SRR does not include the stem of the ring and the SMA connector is directly attached to the ring. This makes the device more compact.

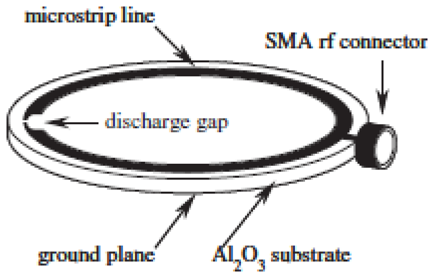

Figure 10. SRR developed by Iza and Hopwood [26]**.**

The same researchers later developed an electrical model of the SRR microplasma sources. The model served as a tool to identify key parameters that control the performance of the device to enhance the microplasma properties. Closed form expressions were used to compare different designs shown in Figure 6. With an electrical model capable of estimating the impedance of the plasma, the plasma properties of the discharge can be estimated as well; including the electron density on the order of 10^{20} /m^3 [9].

Berglund et. al. studied an SRR that removed the dielectric and ground plane material within the gap region while operating at a higher frequency. This design is shown in Figure 11. The removal of the gap was useful to allow gases to pass through the plasma in a controlled fashion. This is useful for applications in fluidic systems. However, the overall expansion of the gap width changes the electric field which leads to a decrease in electric field strength in the gap [27].

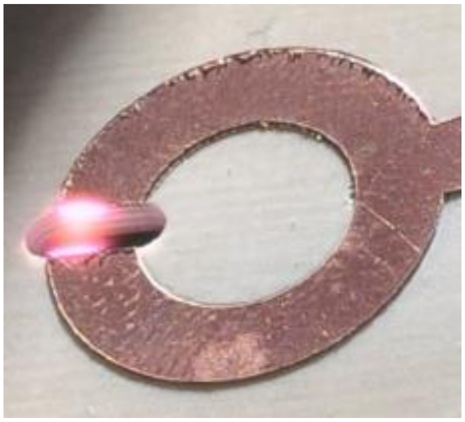

Figure 11. Open gap SRR with plasma ignited in air [27]**.**

Research examining the electromagnetic resonances of the SRR itself, without generation of a microplasma, has also been conducted [29]–[31]. Examining current distributions in the SRR while exposed to magnetic fields can lead to an understanding of the overall electromagnetic behavior of the SRR. With an incident magnetic field penetrating through the SRR, the SRR generates strong electric currents that flow along the ring. Closer to the discharge gap, the electric current on one side vanishes while the current in the middle of the opposite side are maximized. Therefore, charges of opposite sign accumulate at the two extremities of each ring, producing a strong electric field in the gaps [29]. The electric field is the primary factor for ionization within the discharge gap [6]; however, as current passes through the microstrip structure, a magnetic field is produced and can be observed via simulation software.

The most common area of research for the use of SRRs is as a metamaterial structure. Metamaterials can be described as an artificially engineered structure designed to exhibit behaviors such as negative permittivity (ε_r), permeability (μ_r), and refractive index, over a limited range of frequency [30]. Applications such as invisibility cloaks, wave filtering, and perfect wave absorbers are developed due to the extraordinary electromagnetic propagation properties of metamaterials [32]–[34]. Microwave microplasmas generated through a metamaterial has also become of growing interest as the electrical properties of a plasma can potentially be combined with the characteristics of a metamaterial. An example of this is presented by Sakai [35] with the development of a spatially periodic metamaterial structure with negative permeability inside a waveguide. Diffuse microwave plasma is produced throughout this metamaterial exhibiting negative permittivity behavior. This leads to something referred to as a double-negative metamaterial which is capable of allowing multidirectional wave propagation [35].

2.3 Plasma Micropropulsion

The intended application of SRRs in this research is to power plasma micropropulsion for small satellites. The SRR microplasma could be used for all three acceleration mechanisms previously described for electric propulsion: electrostatic, electromagnetic, and electrothermal. These three mechanisms are further described below.

2.3.1 Electrostatic

Electrostatic plasma thrusters utilize a large electric field to accelerate ions. An example of an electrostatic propulsion device is an ion engine. An ion engine uses an electrical grid system to provide the electric field. Figure 12 shows an example of an ion thruster known as the 13-cm Xenon Ion Propulsion System (XIPS) which was first launched in 1997 on the Hughes PAS-5 satellite [4]. Other notable ion engines include the NSTAR and NEXT engines developed by NASA, and the ion engines used on the Hayabusa and Hayabusa 2 asteroid missions. Ion engines have been observed to produce 25 – 250 mN of thrust with 1600 – 5000 s of I_{sp} [36]. Total efficiency is recorded from 50 – 80%. Plasma produced in these thrusters are typically done by electron bombardment. This implies the deposition of energetic electrons leading to electron-neutral collisions inducing ionization. The Hayabusa engines however use RF ionization [37].

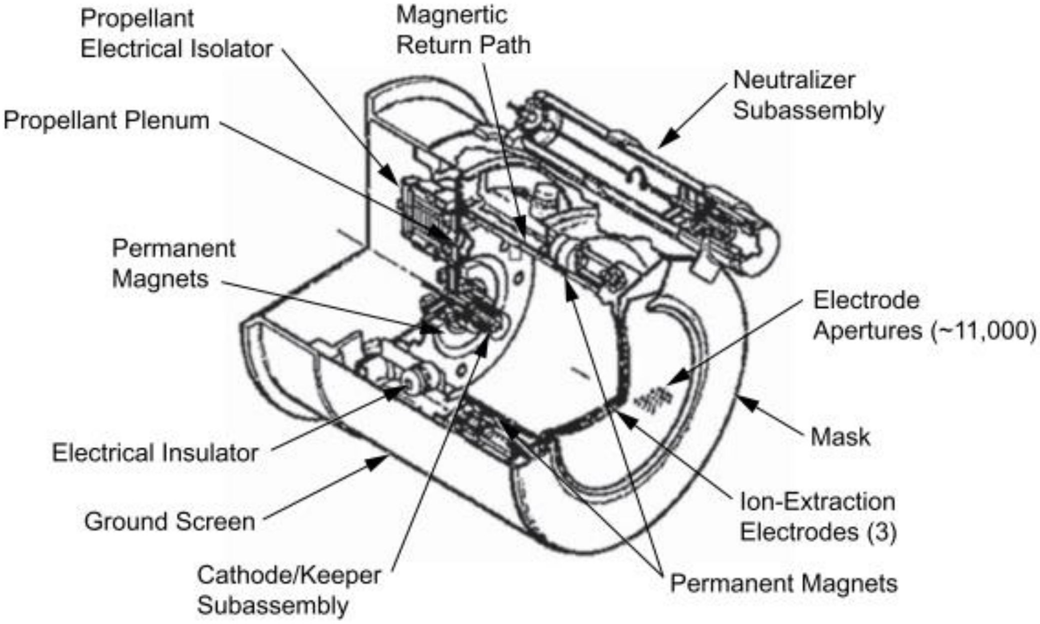

Figure 12. Schematic of the 13-cm XIPS thruster [4]**.**

This electrostatic acceleration mechanism only accelerates the positive ions from plasma and the thrust is primarily determined by the ion velocities exiting the thruster. Figure 12 shows the ion-extraction electrodes that create the accelerating electric fields to produce the exhaust plume. An advantage of an electrostatic thruster is their high specific impulse that scales with the applied voltage on the extraction electrodes. Specific impulse represents the amount of total impulse delivered over mass, essentially reflecting the amount of momentum provided per unit propellant. Due to the decoupling of the acceleration energy from the propellant thermodynamics, high specific impulses in the 1000s of seconds can be achieved. Disadvantages of ion engines include low thrust and erosion that can occur on the grid system when struck by the accelerated ions and the requirement of an additional component, a cathode. This cathode is used as a neutralizer for the plume of the ion engine as only ions are accelerated from the grids. Figure 13 also shows a basic concept schematic of the potential implementation of a microstrip device when designed into an ion micropropulsion system.

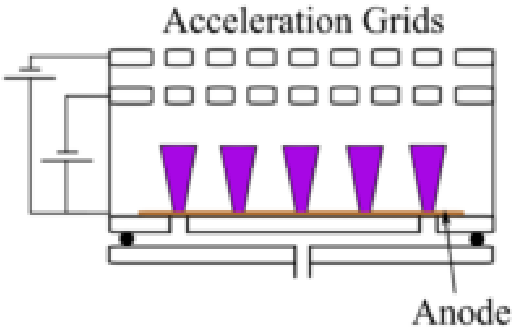

Figure 13. Schematic of electrostatic thruster [3].

Understanding the equations for an electrostatic thruster is important when considering how this research plays a role in micropropulsion implementation. The theoretical performance of an ion engine is given by

$$T = \gamma I_b \sqrt{\frac{2MV_b}{e}} = \gamma J_b A_g T_s \sqrt{\frac{2MV_b}{e}} \tag{3}$$

$$I_{SP} = \frac{\gamma}{g_0} \sqrt{\frac{2eV_b}{M}} \tag{4}$$

Here, T is thrust, I_{SP} is the specific impulse, I_b is the ion beam current, γ is the thrust correction factor that accounts for plume divergence and multiply charged ions, T_s is the screen grid transparency equal to 48.7% based on the MiXI screen grid, J_b is the current density, A_g is the area of the grid, M is the ion mass, and V_b is the beam voltage [4].The main contribution from these equations returns to the emphasis of the plasma properties discussed in this research. The electron temperature and the plasma number density have a significant influence in the current density term in Equation (3). With increased plasma properties, this leads to increased currents in the thruster, providing more thrust. Increased thrust is a desired capability in micropropulsion as high specific impulses can be achieved, but only with low thrust performances.

2.3.2 Electromagnetic

Plasma propulsion systems that require a magnetic field for acceleration is referred to as an electromagnetic propulsion system. Two types of electromagnetic acceleration exist. This includes the use of the Lorentz force and the implementation of magnetic nozzles. Lorentz force, $F = J \times B$, requires the implementation of a high magnetic field and a high current. One example is the magnetoplasmadynamic thruster (MPDT). This thruster is known for its cylindrical geometry with an annular anode surrounding a central cathode. The propellant of an MPDT is ionized when passing through an arc between the electrodes. A schematic is shown in Figure 14 to understand the operation of an MPDT. In this schematic, the self-magnetic field is observed and the interaction with the arc discharge and plasma formation leads to the Lorenz acceleration mechanism [38].

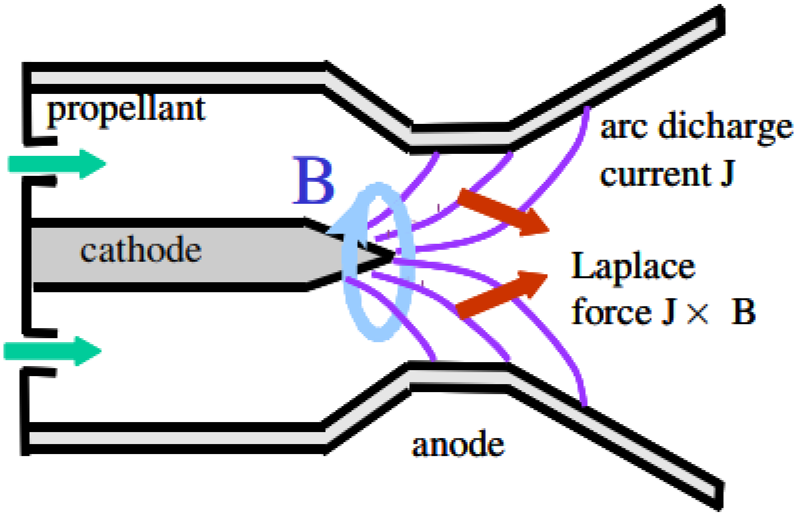

Figure 14. Schematic of a MPDT [38]**.**

Another example of this type of thruster is a pulse plasma thruster (PPT). With a PPT, a pair of conducting electrodes with a propellant medium is operated with a current pulse that ionizes the propellant. The generated current leads to perpendicular self-field-inducing thrust, implying the production of magnetic fields generated from the operation of the thruster itself. Two operating modes for PPTs exist; steady state or pulsed. When operating at steady-state, a small self-field is generated forcing the need for another external magnetic field. Pulsed operation removes the need for an external magnetic field as large current discharges occur. Potential difficulties include material erosion and spot heating for electromagnetic thrusters. However, using this acceleration mechanism can lead to a simple and robust design compared to the electrostatic thruster as no neutralizer cathode or grid systems are needed. Figure 15 provides another example of a schematic of a conceptual electromagnetic thruster designed with an implemented microwave microstrip microplasma device.

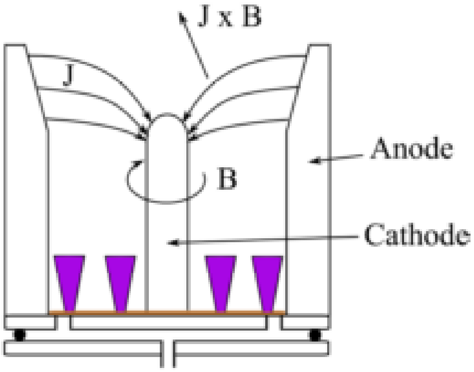

Figure 15. Schematic of conceptual electromagnetic thruster [3]**.**

2.3.4 Electrothermal

Shown in Figure 16, an electrothermal propulsion device consists of the utilization of a micronozzle designed with a thruster chamber. In this case, the thrust is produced similarly to chemical rocket propulsion, where the thermal energy of the propellant is converted to kinetic energy as it accelerates out the nozzle. Analyzing an electrothermal thruster can be done using the isentropic flow equations for a 1D converging-diverging nozzle while assuming the plasma to be a calorically perfect gas. Other assumptions include choked flow, no surface friction or surface heat transfer, and purely axial flow velocity. Plasma can be used as a source of thermal energy providing that the source is capable of increasing gas temperature sufficiently for thrust. Performance limits are also dependent on pressures and nozzle expansion ratios, similarly to chemical propulsion. Lifetime limits exist for the electrothermal thruster as nozzle erosion can occur; however, an advantage of the electrothermal mechanism is the simplicity and ease of fabrication.

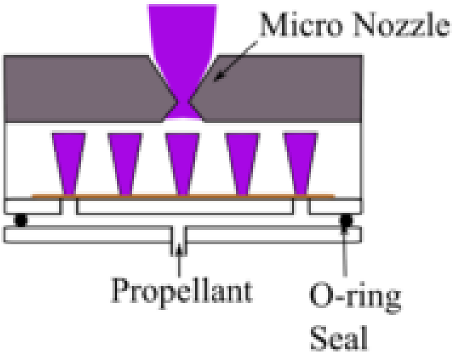

Figure 16. Schematic of electrothermal thruster [3]**.**

As an overview to understand the difference between these different types of acceleration mechanisms, Table 1 shows the parameters of a variety of different thrusters.

Table 1. Performance of some electric thrusters [38]**.**

Thruster	Electric Power (kW)	I_{sp} (s)	T (N)
Electrostatic – Gridded Ion	0.3 – 5	1000 – 4000	10^{-3} – 0.2
Electromagnetic - MPDT	200 – 1000	2000 – 5000	2 – 15
Electrothermal – Arcjet	0.3 – 2	500 – 600	10^{-3} – 5

As observed in this table, electromagnetic thrusters have shown significant advantages in performance. However, due to simplicity, electrothermal thrusters became the first iteration when implementing microstrip technology into a micropropulsion system. Ion thruster concepts are discussed in this dissertation to understand the potential of this type of thruster when designed with microstrip resonators.

Taking into consideration the potential implementation into a micropropulsion system, a side experiment was conducted. A boundary condition experiment focused on the change in microplasma properties when operating the device in an open (infinite boundary condition) environment versus a closed (finite boundary condition) environment. This experiment provided insight on the expected behavior of the microplasma inside a small volume, for example inside a thruster body. A prototype microthruster was build using additive manufacturing for this experiment to provide the closed environment. Due to wall losses and neutralization, as expected, lower electron temperatures were observed in a closed environment. An example of this for the SRR is a decrease of ~2 eV from open to closed environments. Figure 17 shows two prototype microthrusters, the one the left, an Inconel prototype, and on the right, an ABS prototype with an ignited microplasma.

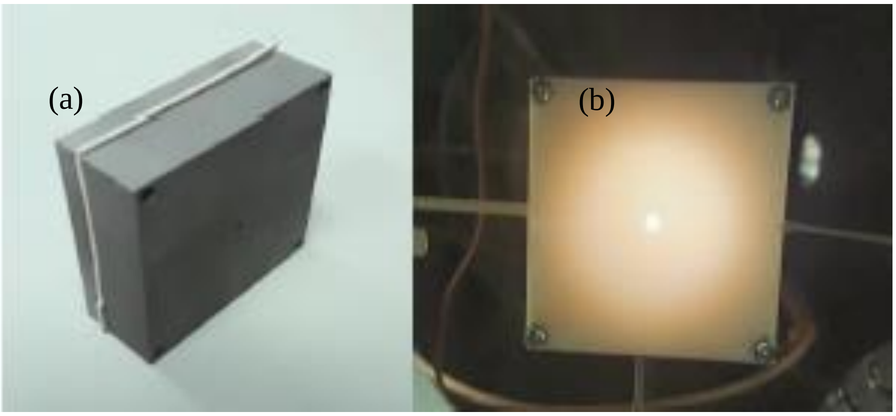

Figure 17. (a) Inconel microthruster prototype. (b) ABS plastic microthruster prototype with SRR ignition.

Comparing the SRRs and CSRRs, is is expected that with higher plasma properties, the performance within a thruster will increase. This is particularly true from the equations given for the electrostatic thruster. In terms of an electrothermal mechanism, as higher plasma populations are produced, this leads to higher amounts of plasma accelerated through a micronozzle or a grid system, increasing thrust.

Chapter 3.

Experimental Approach

Research is what I'm doing when I don't know what I'm doing.

– Wernher von Braun

3.1 SRR Design and Fabrication

The SRR is fabricated with photolithography and wet etching techniques using a RT/Duroid 6010 laminate as the substrate. The 6010 Duroid has a dielectric constant of ~10.2 and has a thin film of 34 μm thick copper cladding on both sides. The SRR is created on one side of the substrate while the back plane is untouched. The central conductor of an SMA connector is soldered to the ring while the grounded body is soldered to the back plane. Figure 18 provides a generic schematic of the split ring resonator and a fabricated SRR source with a 1.5 mm strip width. The mean diameter of the ring is ~20 mm.

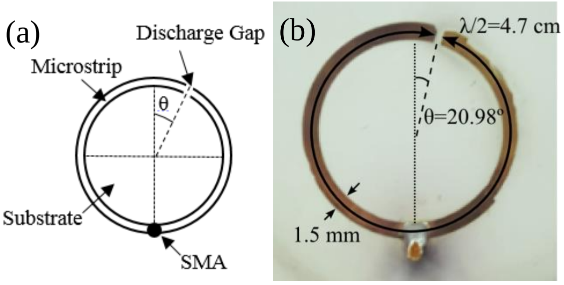

Figure 18. (a) Schematic of SRR. (b) Fabricated SRR by UAH PRC.

The mean circumference of the SRR is designed to be half the wavelength corresponding to the driving frequency and dielectric constant of the substrate given as,

$$\frac{\lambda}{2} = \frac{c}{2f\sqrt{\varepsilon_r}} \tag{5}$$

where, c is the speed of light, λ is the wavelength, and ε_r is the dielectric constant of the substrate. As the microwaves propagate through the device, the dielectric allows the electromagnetic field to mainly develop between the microstrip plane and the ground plane[39]. At the discharge gap the voltage at either end is 180° out of phase with each other and develops a large amplitude electric field that can ionize the gas, as shown in Figure 19.

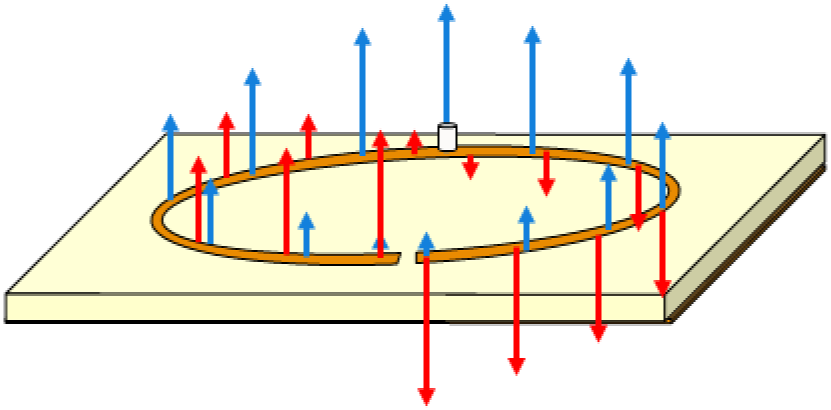

Figure 19. Example of microwave propagation in SRR for current (blue) and voltage (red).

The gap location for maximum power is determined by the phase offset angle, θ. The relationship between the offset angle, the impedances, Z, and the theoretical quality factor, Q is given as,

$$\cos\theta = 1 - \frac{Z_{in}\pi}{Z_0 Q} \tag{6}$$

An example of the positioning of the phase angle can be seen in Figure 18. Assuming the signal input impedance (Z_{in}) is 50 Ohms, the characteristic impedance (Z_0) of the antenna can be determined by the geometry of the SRR. The phase angle requires knowing the quality factor which is given as,

$$Q = \frac{\pi}{\alpha\lambda} \tag{7}$$

where α is the attenuation factor, which is function of the geometry and signal frequency. A relationship between the characteristic impedance Z_0 and α is explored in reference [40]. This new characteristic impedance perturbation method is used to determine the attenuation constant in this dissertation. Commonly, the attenuation factor is defined by,

$$\alpha = \frac{P_L}{2P_0} \tag{8}$$

Here, P_L is the power loss along the per-unit longitudinal length of the conductors while P_0 indicates the real power of the transmission line. Experimentally measuring these parameters and obtaining the overall power loss and real power delivered can be used to obtain the attenuation constant. However, the relationship with the characteristic impedance is also explored to understand how the transmission lines can vary based on frequency, impedance, attenuation, and hence, quality factor. With the assumption that the magnetic field is negligible, the power ratio in Equation (8) can be converted to,

$$\frac{P_L}{2P_0} = \frac{R_S}{2\eta} \tag{9}$$

Here, R_s indicates the surface loss resistance of the conductors [$R_s = \sqrt{(\omega\mu/2\sigma)}$] and η represents the wave impedance, [$\eta = 120\pi/\sqrt{\varepsilon_r}$]; σ is defined as the conductivity, ω is the frequency term, and μ is the permeability. Making the normal perturbation of the transmission of displacement *dn* on each point on the boundary of the transmission line in the direction of the outward normal, a differential characteristic impedance of dZ_0 can be expressed as,

$$\alpha = \frac{R_S}{2\eta} * \frac{1}{Z_0}\left(\frac{dZ_0}{dn}\right) = \frac{R_S\sqrt{\varepsilon_r}}{240\pi}\frac{1}{Z_0}\frac{dZ_0}{dn} \tag{10}$$

This equation defines the relationship between attenuation factor and impedance [40]. Using Equation (10), a theoretical approach to determine the attenuation factor can be achieved using geometrical and experimental parameters. With the attenuation constant, quality factor can be determined, giving a parameter that characterizes the resonator's oscillatory behavior. Particularly, the quality factor may be used to understand conduction and radiation losses in the transmission line. A decreased quality factor implies a narrower transmission line, resulting in an increase in characteristic impedance. With a lower quality factor, larger conduction and radiation losses can occur; therefore, it is important to use a highly conducting material (in this case, copper) to maximize the voltage generated across the discharge gap [9].

3.2 Facilities

A small cylindrical vacuum chamber at the UAH Propulsion Research Center and at NASA's Marshall Space Flight Center was used to conduct the SRR/CSRR experiments. Electrical, pressure, and propellant feedthroughs are attached around the chamber. The chamber pressure was measured with a Baratron gas independent pressure transducer. A schematic of the experimental setup is shown in Figure 20.

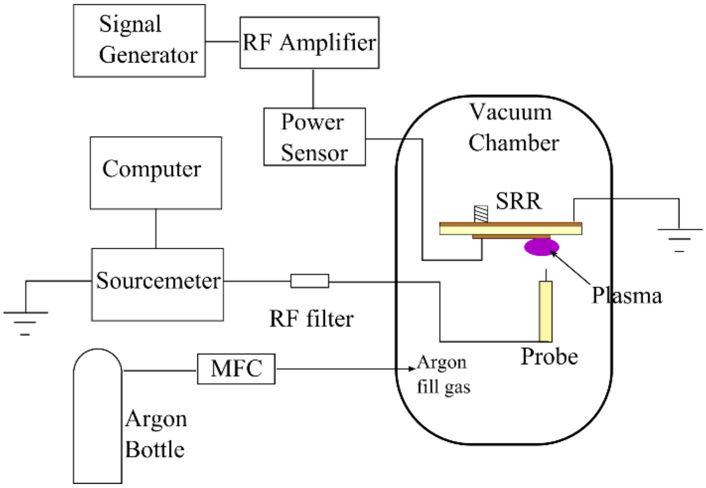

Figure 20. Experimental setup diagram at UAH PRC.

The pre-amplified input power from the microwave generator ranged from -11.0 dBm to -7.0 dBm. The power was increased by +48 dB by the RF amplifier, thus 37-41 dBm. A digital Bird 7020 power sensor measured the forward and reflected power and the voltage standing wave ratio (VSWR) in the circuit. The VSWR measurements were used to convert the total input power to the forward power going to the SRR. Overall, the total forward power sent to the SRR varied from 4.7 to 11.34 W. This power range was chosen based on the capabilities of the RF amplifier, the required ignition power, and the desire to run at < 15 W to meet small satellite power systems. All powers reported from here on are the forward power. Following the power sensor, the transmission line then enters the vacuum chamber and to the SRR. The SRRs were tested at a chamber pressure ranging from ~350 mTorr-argon to 1000 mTorr-argon. The signal then reaches the source and generates the argon microplasma. This same setup was utilized for SRRs and CSRRs for varying frequencies.

3.3 Diagnostics - Single Langmuir Probe

A single Langmuir probe was used to measure the electron temperature and plasma number densities of the microplasma [41] in the SRR width experiment described later. The Langmuir or electrostatic probe in the basic form consists of a conducting tip, typically a small wire or sphere, that is immersed in the plasma and has a variable voltage applied. In this work, a thin tungsten wire is used which is housed in an alumina tube to control the length of the exposed conductor. The current collected from the microplasma as a function of voltage generates a current-voltage curve which is analyzed to determine the electron temperature, and ion and electron densities of the microplasma. In this work, a Keithley 2410 sourcemeter is used to provide the probe voltage and measure the resulting current. Figure 21 shows an example of the alumina tube and Tungsten wire used for the probe in the SRR width experiment.

Figure 21. Langmuir probe from UAH PRC (millimeter units).

The probe tip has a diameter of 0.127 mm, a length of ~1 mm, and the end is located ~4 mm above the SRR/CSRR. A low pass 500 MHz RF filter is implemented to ensure no microwave interference when collecting data. Fundamentally, a Langmuir probe perturbs the plasma providing a boundary where governing equations of plasma motion are used to observe the change in plasma characteristics. With quasi-neutrality existing in the bulk of the plasma, when the bulk plasma is exposed to the probe, a potential difference occurs between the probe surface potential and the plasma potential. The plasma potential is the average electric potential in the plasma. This potential change is concentrated in a thin layer next to the probe surface referred to as a sheath. As a bias voltage is sustained on the probe, current flows into the probe. While the probe, or the electrode, has a potential different from the local plasma potential, the particles distribute themselves spatially around the probe in order to shield the effect of this potential on the bulk plasma. This can be referred to as the plasma attempting to maintain its quasi-neutrality. As mentioned, the I-V, or current-voltage curve, is then produced and utilized to analyze and determine plasma properties. The curve over the bias voltage used in this research is obtained by sweeping the voltage and obtaining a current measurement, point by point. The probe characteristics can then be described as different regions of the curve. These regions include the electron saturation current, the electron retardation region, and the ion saturation current. The saturation current is obtained when sufficient positive or negative biased voltage is applied to measure electron or ion currents, respectively. When the probe current is zero, this is known as the floating potential. The retardation region is represented by the transition between the saturation currents.

Physically, in order for ion saturation to occur, the bias voltage applied must be sufficiently negative compared to the plasma potential in order to repel all incident electrons. As the potential on the probe is increased using the power supply, fewer electrons are repelled and thus the current magnitude decreases due to collecting both positive and negative currents. When the bias voltage is significantly higher than the plasma potential, all ions become repelled and the probe collects only electron current. The floating potential is achieved when the ion and electron current are equal and no there is no net current from the plasma. For a probe to be electrically floating, the potential may rise and fall to what's necessary to maintain zero net current. As electrons are drawn to the probe faster than massive positive ions, the probe floats to a potential lower than the plasma potential so that electrons become slowed and ion collection is enhanced. This forms the electron retardation region. Using the electron retardation region allows the determination of the electron temperature, T_e. This is accomplished by taking the inverse of the slope of a straight line fit on a semi-log scale [42]. A semi-log scale is used to provide a clear demarcation of the plasma potential and electron saturation current. Also, as the basic equation for the sheath currents use an exponential term with electron temperature, it is necessary to take the natural log, leading to,

$$T_e = \frac{V_2 - V_1}{\ln\left(\frac{I_{e2}}{I_{e1}}\right)} \tag{11}$$

Here, *1* and *2* refer to any points on the line in the electron retardation region [42]. The regions for saturation currents and retardation can be seen in Figure 22.

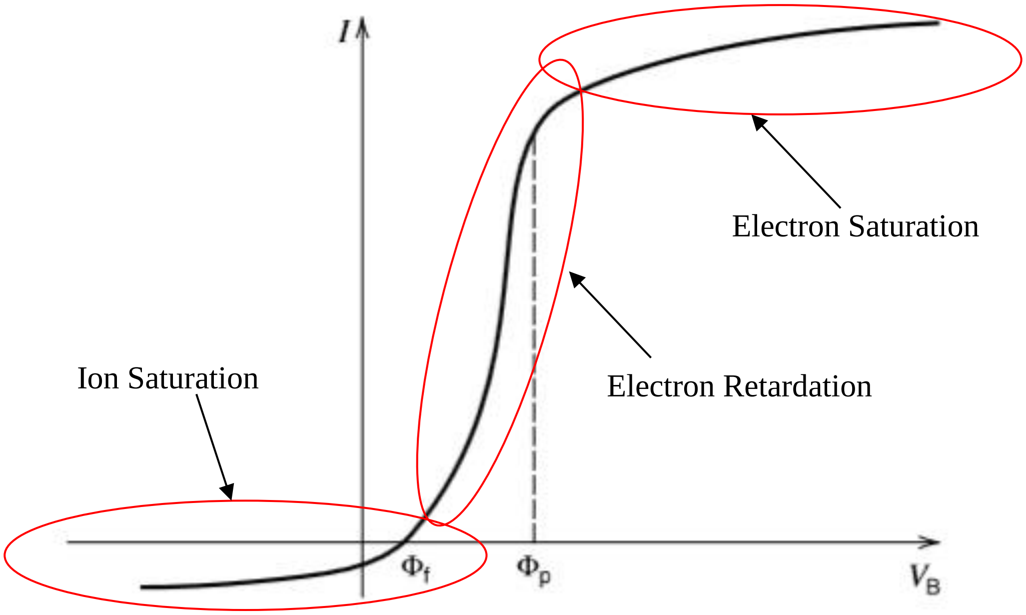

Figure 22. Ideal Langmuir probe current-voltage characteristic (heavy line) for a model plasma. Plasma and floating potentials displayed.

The analysis of single Langmuir probe data depends on the collisionality of the plasma. When operating in a collisional or collisionless regime, different analysis techniques are used. When collisional, the ion-neutral mean-free path is smaller than the Debye length. As the probe sheath thickness is on the order of a few Debye lengths, for every mean-free path, a collision occurs in the sheath in collisional plasmas. Collisionless plasma implies a the mean-free path is larger than the Debye length thus no collisions occur inside the sheath. The α_c is defined as, [43]

$$\alpha_c = \frac{\lambda_D}{\lambda_{mfp}} \tag{12}$$

where, $\lambda_D = [\varepsilon_0 kT_e/(ne^2)]^{1/2}$ is the Debye length, and λ_{mfp} is the ion-neutral mean-free path. The ion-neutral collisional mean free path can be determined using $\lambda_{mfp}=v_n/(n_e<\sigma v_e>)$ where the neutral particle velocity, v_n, and the cross section, $<\sigma v_e>$, for argon ion neutral collisions is known. For argon, the simple equation $\lambda_{mfp}=(330P)^{-1}$ where P is in Torr and λ_{mfp} is in centimeters can be used. The plasma can be considered collisional if $\alpha_c > 1$, and collisionless if $\alpha_c < 1$. For each type of collisionality regime, different equations are used for Langmuir probe diagnostics.

The electron temperature was determined from the inverse of the slope of a plot $\ln(I_e)$ against V. In a collisionless regime, equations,

$$I_0 = Aen_e\left(\frac{KT_e}{2\pi m}\right)^{\frac{1}{2}} \tag{13}$$

$$I_+ = Ane\left(-\frac{e\varphi}{8M}\right)^{\frac{1}{2}} \tag{14}$$

are used to calculate the electron and ion densities, respectively.

Here, n_e is the electron number density, n is the ion density, I_0 is the electron saturation current, I_+ is the ion saturation current, e is the magnitude of the electronic charge, *m* is the electronic mass, *M* is the ion mass, φ is the value of the DC potential, *k* is the Boltzmann constant, and *A* is the probe area [12]. In a collisional regime, the approach becomes more complex as it accounts for the effects of collisions and bulk convection. The collisional single Langmuir probe theory for collisional effects in a stationary plasma are presented here for completeness. Stationary plasma refers to the simplest case where ion transport to the probe is controlled by the normal diffusion processes. Three nondimensional numbers are used for this regime: the electric Reynolds number (R_e), a Debye ratio (α), and the probe bias voltage (χ) shown as, [44]

$$R_e = \frac{2r_p v_f}{\mu_i T_{eV}} \tag{15}$$

$$\alpha = \frac{\lambda_D}{r_p} \tag{16}$$

$$\chi = \frac{V_p}{T_{eV}} \tag{17}$$

With a stationary plasma and the calculation of the nondimensional parameters, plasma densities are calculated within two regimes. These regimes include a thin sheath or a thick sheath surrounding the probe. The thicknesses of the sheath are based relative to the radius of the probe. As the sheath becomes thicker, the collection becomes significantly larger leading to an over-calculation of density compared to the thin sheath [44]. The equations for plasma densities in these regimes are shown in the Table 2 [45], [46].

Table 2. Criteria and analytic plasma density solution for Langmuir probe regimes in a stationary plasma.

Regime	Criteria	Plasma Density
Thin Sheath	Re < 1, αχ << 1	$n_0 = \frac{I_{i,sat} \ln\left(\frac{\pi L}{4r_p}\right)}{2\pi L k \mu_i (T_e + T_i)}$
Thick Sheath	Re < 1, αχ >> 1	$n_0 = \frac{I_{i,sat} \ln\left(\frac{\pi L}{4r_p R_s}\right)}{2\pi L k \mu_i (T_e + T_i)}$ $R_s = 1 + 0.06\left[\frac{Z\lambda_{mfp} L V_p^2}{r_p^2 I_{i,sat}\sqrt{T_i MW_i}}\right]$

In Table 2, Z is the charge state, r_p is the probe radius, μ_i is the ion mobility, and MW_i is the molecular weight of the ion species.

3.4 Diagnostics – Double Langmuir Probe

For some experiments, a double Langmuir probe is used to measure the electron temperature and plasma number densities of the microplasma. While the single Langmuir probe successfully obtained the data for the width experiment; uncertainties have brought concern when using single probes in RF plasmas. Without proper compensation due to the RF microwave microplasma behavior, distortions in the data can lead to overestimated values of electron temperature. This occurs as RF interference has the effect of distorting the electron retardation region of the probe trace while shifting the floating potential towards more negative voltages. To solve this, an RF choke or a double probe can be implemented. This is primarily due to two reasons. First, the double probe typically collects significantly less current; this allows for true saturation to be achieved when a negative or positive potential is applied to the individual probes. “True” saturation reflects saturation occurring due to the characteristics of the plasma instead of external interference effects on the probe. The second reason is that both tips on the double probe are floating with respect to the discharge circuit. This allows the presence of a reference point. When operating the single Langmuir probe, the reference point is typically ground, in this instance, the vacuum chamber walls. With a completely collisionless environment, a clear path to ground is present when operating single Langmuir probes. However, with the use of a double probe, at least one of the tips will always be floating, which can act as a reference point to ground. With ground always present nearby, uncertainties involving the overestimation of electron temperatures and achieving true saturation can be prevented. Using a double probe leads to the acquisition of an ion saturation current in both negative and positive directions and the curve passing through the origin of zero voltage and zero current.

Similar to the single probe, the double probe was placed ~4 mm above the surface of the SRR or CSRR. The probe was built by inserting two isolated 0.127 mm diameter tungsten wires into a 2.39 mm diameter alumina tube, leaving a ~1 mm length of wire exposed for each tip of the double probe. An external bias voltage from -50 to 50 V was applied to the Langmuir probe with a Keithley 2400 sourcemeter to attract the ions or electrons to the exposed probe tips. The current at each voltage was measured to create the characteristic I-V curve which was analyzed to determine the plasma properties[41].

The double Langmuir probe is considered to be in the collisionless regime if the ratio of the Debye length λ_D to the ion-neutral collisional mean free path of the plasma λ_{mfp} is less than unity [12]:

$$\alpha_c = \frac{\lambda_D}{\lambda_{mfp}} < 1 \tag{18}$$

The ion-neutral collisional mean free path can be determined as $\lambda_{mfp}=1/(n_e\,\sigma)$, where n_e is the plasma number density and σ is the cross section for argon ion-neutral collisions [13]. For argon at standard temperature, the ideal gas equation of state can be used to simplify the mean free path (in centimeters) to $\lambda_{mfp}=1/(330\,p)$, where p is the pressure in torr. For the pressures and plasma properties in this work the plasma is in the collisionless regime [10] with α_c between 2.5×10^{-4} and 1.0×10^{-3}.

For the double probe shown in Fig. 22a, the current collected by the each of the two probe tips of equal area is given as

$$i_1 = i_0\left(1 - e^{\frac{e(V_1 - V_F)}{(kT_e)}}\right) \tag{19}$$

$$i_2 = i_0\left(1 - e^{\frac{e(V_2 - V_F)}{(kT_e)}}\right) \tag{20}$$

where $|I_{1i}| = |I_{2i}| = i_0$ are the ion saturation currents in Fig. 2b, e is the elementary charge, V_F is the floating potential, k is Boltzmann's constant, and T_e is the electron temperature. The currents collected by the probes are constrained such that $i_1 + i_2 = 0$ while the voltages applied to each probe tip satisfy the relationship $V_2 = V_1 - V$. Manipulation of the current collection equations (19) and (20) under these constraints allows us to write the double probe characteristic as

$$i_1 = i_0\, tanh\big(eV/(2kT_e)\big) \tag{21}$$

Finding the slope of the characteristic at V=0 permits us to solve for the electron temperature as

$$\frac{kT_e}{e} = i_0 \Big/ \left(2 \frac{di_1}{dV} \bigg|_{V=0} \right) \tag{22}$$

The ion saturation current based upon the Bohm criteria is

$$i_0 = exp(-1/2)\ en_e A \sqrt{\frac{kT_e}{m_i}} \tag{23}$$

where m_i is the ion mass. With the electron temperature already calculated from the data and the ion saturation current known through measurement, this equation can be rearranged to yield the number density in terms of known quantities as

$$n_e = i_0 \Big/ \left[\exp(-1/2)\ eA \sqrt{\frac{kT_e}{m_i}} \right] \tag{24}$$

In these equations, $I_{i,sat}$ is the average of the saturation currents, e is the magnitude of the electronic charge, m is the electronic mass, M is the ion mass, q is the electron charge, k is the Boltzmann constant, and A is the probe area [12]. Figure 23 shows a schematic of the current flow observed by the double probe when exposed to the bulk plasma and the typical current-voltage characteristic curve obtained when applying the bias voltage on each probe tip.

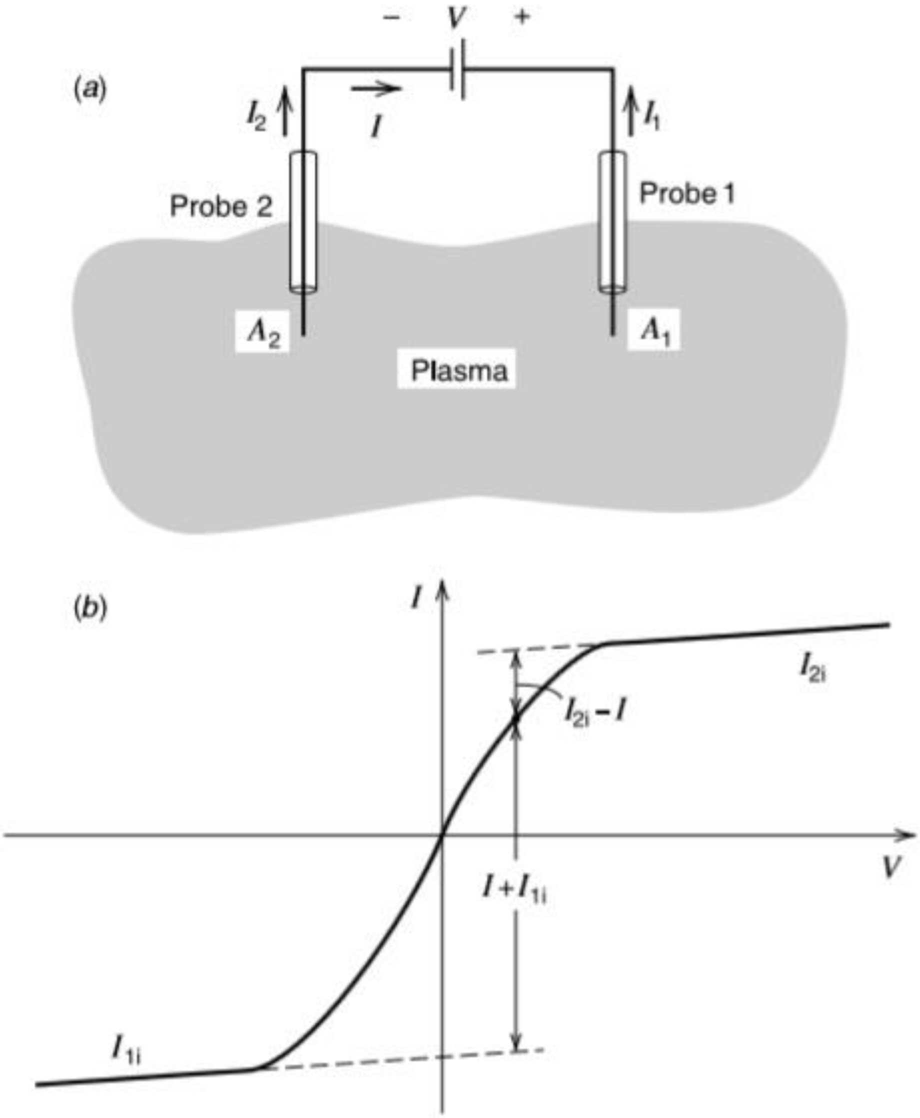

Figure 23. Schematic of double probe measurement. (a) definition of voltage and currents, (b) typical current-voltage characteristic [25]**.**

Similar to the single Langmuir probe data, the saturation regions can be observed and double probe theory can be used to determine the desired plasma properties. However, in a double probe, only the ion saturation is observed; while in single probe, ion and electron saturations are measured.

In both single and double Langmuir probe diagnostic techniques, it is important to consider the electron energy distribution function (EEDF). Typically, the assumption of a

Maxwellian energy distribution is made for conventional Langmuir probe theory. In Maxwellian plasmas, determining the electron temperature is simple and direct as the electron energy can be characterized by a single scalar value, shown in this section as T_e. This is particularly common in space plasmas discussed by Hoegy [47]. However, microplasmas are characterized by non-Maxwellian energy distribution functions [14]. This is due to the presence of additional electron populations significant in magnitude, leading to complexities in the determination of the electron temperature. However, in order to determine approximate values of the plasma properties, Maxwellian distribution must be assumed. This has been done by Cox for RF-generated argon plasmas comparing Langmuir probes to optical emission spectroscopy [12]. In this research, the determination of plasma properties is also conducted with the assumption of a Maxwellian distribution for simplicity.

3.5 Probe Mapping Technique

A probe mapping technique is also applied in order to obtain microplasma distribution data over the device. Using a two-axis Velmex stepper motor, a matrix of I-V curves is generated at each point of a 6x6 grid 4 mm above the resonator as shown in Figure 24. The plasma properties at each point are then determined. A total of 36 points were collected where each horizontal step is 5.6 mm while each vertical step is 4.1 mm. Each step collected from the Velmex stepper motor has a systematic uncertainty of ± 0.05˚, or for the utilized stepper motors, ±0.025 mm. It is detailed by Velmex Inc. that this error does not accumulate from step to step. This spacing was chosen to have one measurement location above both the inner and outer gaps.

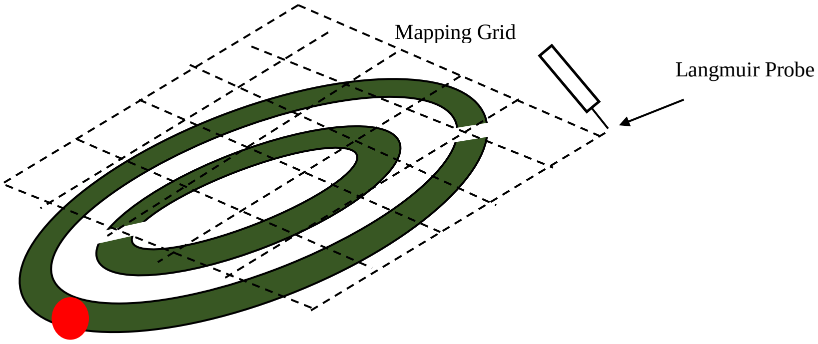

Figure 24. Sample Schematic of CSRR with gridded map showing points of current-voltage data acquisition.

Probe mapping is most effective in understanding the size and uniformity of the device. With the placement of the Langmuir probe known on the map, the overall area on a 2-dimensional plane of the microplasma can be determined. The distribution of the microplasma properties can also be determined to understand the uniformity of the plasma. The distribution of plasma around the discharge gap is unclear yet it is expected to have a peak in microplasma properties above the discharge gap. However, microplasma size and uniformity changes as microplasma properties are enhanced. A higher energetic plasma leads to increased ionization inducing a larger volume obtained by the microplasma. Essentially, observing the plasma properties over this area of the device can lead to an understanding as to how the plasma distributes. It is expected that a peak in electron temperature occurs near the discharge gap; however, when frequency is changed, the microplasma properties, size, and distribution, can be affected.

Each point shown on Figure 24 represents an I-V curve collected from the Langmuir probe. It is expected that every point that overlaps a discharge gap, a peak in the microplasma properties should be found.

3.6 ANSYS High Frequency Structure Simulator (HFSS)

The simulator software used to understand the electric and magnetic field behavior is known as ANSYS High Frequency Structure Simulator (HFSS). HFSS is a commercial software that uses a finite element method solver for electromagnetic structures. This finite element approach generates a meshing algorithm encompassing the oscillator structure and analyzes the electromagnetic activity when a microwave signal source is applied. This tool is commonly used for antenna designs that involve complex RF electronic circuits such as filters, transmission lines, and integrated circuit packages and printed circuit boards. Engineers use HFSS to design high-frequency, high-speed electronics found in communication systems, radar systems, satellites, and other high-speed RF and digital devices. Work on split-ring resonator simulations has been demonstrated using HFSS by previous researchers [6] proving this software to be useful in the research presented here. In this dissertation, electric and magnetic field simulations are generated in order to understand the behavior of the resonators and how the electromagnetic profiles can impact the plasma property results.

Chapter 4.

Results and Discussion

Research is formalized curiosity. It is poking and prying with a purpose.

– Zora Neale Hurston

4.1 Introduction

Three different experiments were done to better understand the relationship between the SRR and the microplasma properties. These experiments include 1) the effect of ring width, 2) the effect of adding a second nested ring, and 3) the effect of off-resonant operation on the nested ring design. Each experiment was accompanied by an HSFF electromagnetic model to help predict and understand the resonator behavior. Langmuir probe measurements were done for all experiments. The properties of interest are the electron temperature and the electron and ion densities. The thrust and specific impulse for a conceptual plasma microthruster can be determined theoretically from these properties. This is accomplished later in this dissertation.

4.2 Experiment 1: Width Effect on SRR Microplasma

A study on the impact of the change of the geometrical parameters on a split-ring resonator source is necessary to study and understand the relationship to the plasma properties. It is desirable to increase density and temperature for propulsion applications.

In the SRR width experiment, the width of the microstrip of the SRR was varied in order to determine the impact of the width on the microplasma properties. With a change in microstrip width, impedance in the resonator changes, leading to different wave propagations that can cause changes in the electric field used to generate the plasma and shape its characteristics. For the purpose of building a microthruster, this geometric parameter needed to be studied. Determining the width with the most improved performance in plasma properties can potentially be utilized for implementation in a micropropulsion design. The width of the ring of the SRR was varied from 1.5 mm to 6 mm and the microplasma properties of electron temperature and density were measured using a single Langmuir probe. Figure 25 below shows the 6 mm SRR operating on argon gas.

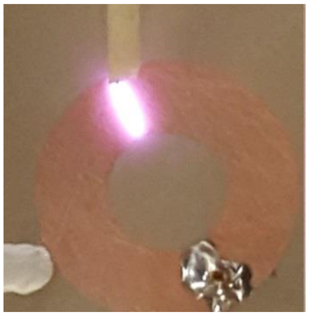

Figure 25. Operating SRR from UAH PRC.

The SRRs were tested at an argon pressure range of ~350 to 1000 mTorr, and using both collisionless and collisional methods resulted in plasma properties that gave collisionality values from 0.00025 to 0.001, placing the plasma in the collisionless regime. Thus the collisionless Langmuir probe equations were used. After the devices were fabricated, the resonant frequency was experimentally found as the frequency for the maximum forward power read by a Bird 7020 power sensor. The resonant frequency for each SRR was constant over the power range tested (4.7-11.34 W). The simulated and measured resonant frequencies along with the appropriate quality factors and phase angles are shown in Table 3.

Table 3. Theoretical Frequency, Quality Factor, and Phase Angle for all SRR Widths.

Width (mm)	**Design Frequency (MHz)**	**Quality Factor**	**Phase Angle (deg)**	**Simulated Resonant Frequency (MHz)**	**Measured Resonant Frequency (MHz)**
1.5	1000	53 ± 4%	20.98 ± 4%	1450	1240 ± 4%
3	1000	79	21.13	1280	1240
4.5	1000	85	23.40	1180	1173
5	1000	87	24.09	1190	1173
6	1000	90	25.39	1180	1174

Table 4 below shows the actual impedance measured by a network analyzer (Advantest R3767CH) and the theoretical gap voltage for each split ring resonator width. The gap voltage can be calculated from [9]

$$V_{gap} = 4\sqrt{\frac{Z_o Q}{\pi}}\sqrt{P_{in}} \tag{25}$$

Table 4. Actual Impedance Values.

SRR Width (mm)	**Actual Impedance (Ohms)**	**V_{gap} at 5 W (V)**
1.5	30.06 ±0.002%	201.4 ±0.002%
3	37.90	276.1
4.5	23.38	224.9
5	35.63	280.9
6	29.16	258.5

Representative uncertainties for the calculated and measured data in Table 3 and 4 are displayed in the corresponding first row and are consistent for all SRR devices. These values are based on the systematic error of the equipment utilized for collecting these measurements. Fabrication concerns can lead to the cause of the distinct values in actual impedance; however, with a change in width, a change in the capacitive behavior within the discharge gaps can occur. When designing SRRs, increasing the capacitance to provide a stronger resonance is common [48]. However, an important parameter examined in ring resonators is the resonant width [49]. Explored by Bilotti [50] in multiple ring resonators, distributed capacitance in an SRR can saturate based on geometric features, including the width. The same concept applied to single SRRs and CSRRs implies that a resonant width exists where impedance is best matched with the microwave system and device couples best with the applied microwave signal. For the case of the 3 mm ring, the best resonant width parameter is determined, reflecting the most enhanced resonance achieved at this frequency. Figure 26 shows the current-voltage data obtained for the SRR width experiment. The analysis for the current-voltage data is conducted following single Langmuir probe theory explained in the experimental approach section of this dissertation.

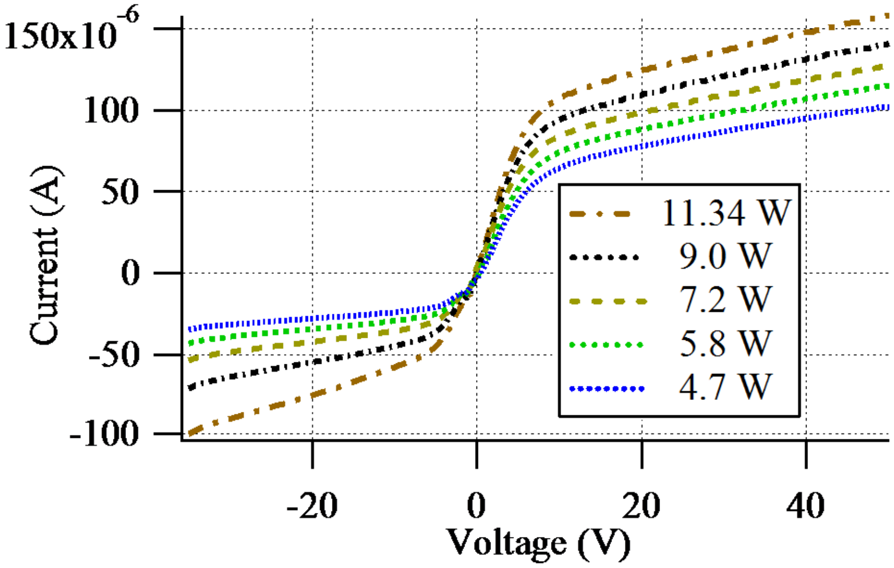

Figure 26. Current-Voltage Curve for SRR Width experiment.

4.2.1 Simulations Results

The electric fields in the microstrip of the SRRs were simulated with ANSYS HFFS [51]. A higher electric field should produce higher electron temperatures and plasma densities. Simulations shown in this section were performed for SRR widths from 1.5 to 6 mm. The results for the 4.7 W cases are shown here, with the other powers having the same trends with width. It is noted that the meshing algorithm applied by HFSS can result in skewed measurements if the solution frequency is off the true resonant frequency [6], [52]. With an imperfect mesh, certain anomalies can be observed in the electric field intensity. Thus the results obtained by HFSS are approximate. Comparing the measured impedance trends and the simulations, there is some agreement that 3 mm and 5 mm would peak in electric field intensity. This is due to impedances matching closer to 50 Ω. Figure 27 displays the maximum electric field strength in the microstrip along the inner edges of the discharge gap from the model. Simulation results for 1.5 through 6 mm rings can be found in Figure 28.

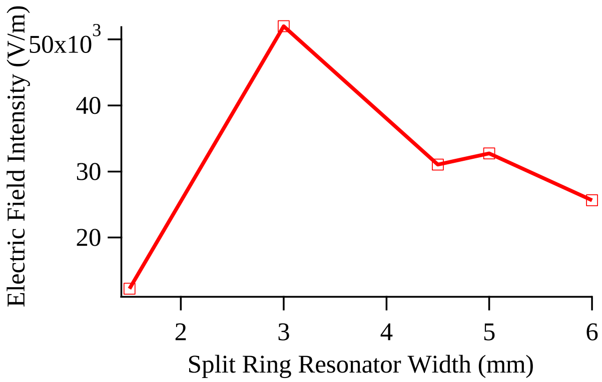

Figure 27. Simulation results of electric field intensity versus SRR width.

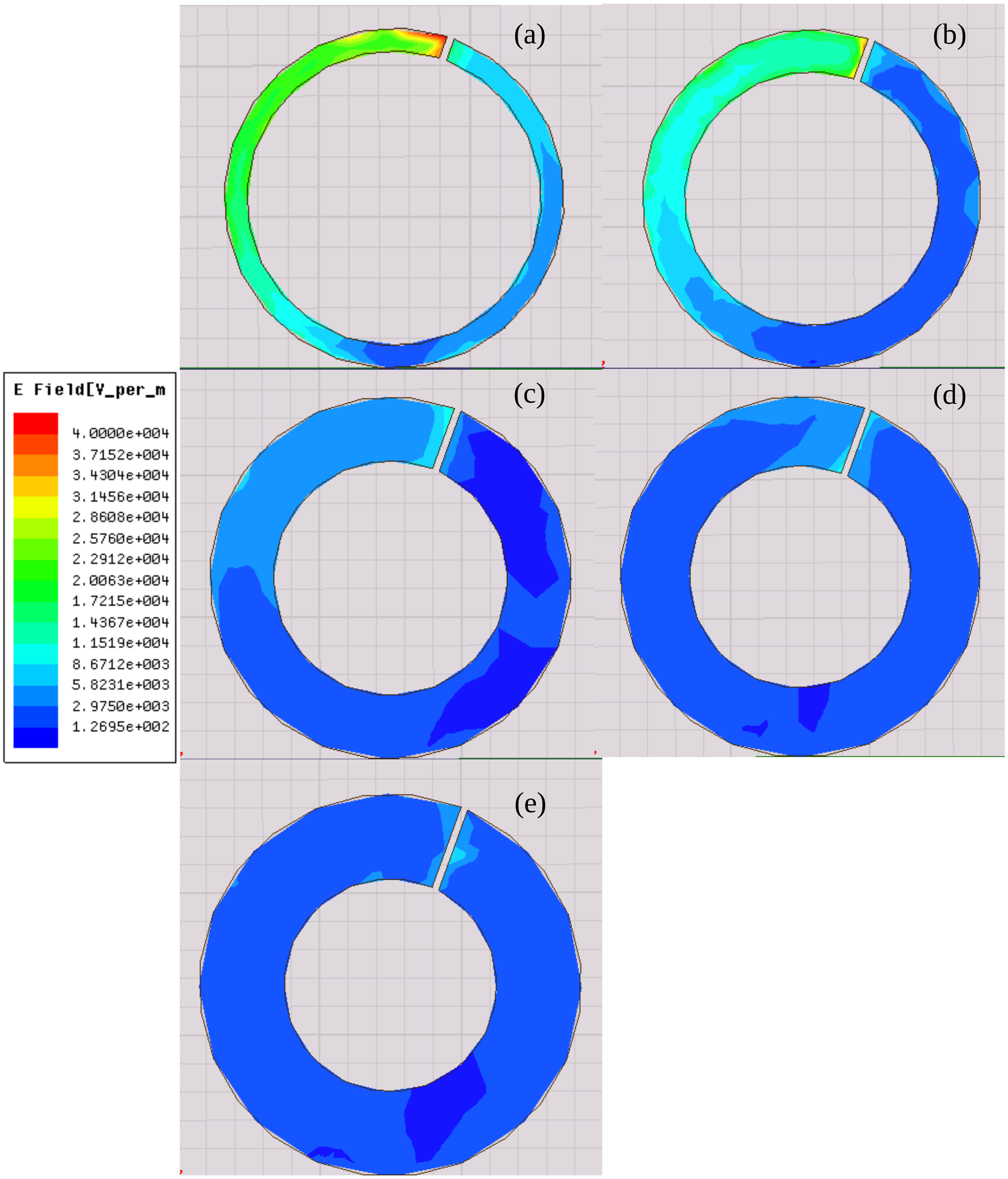

Figure 28. Split Ring Resonator EM Simulations for varying widths. (a) 1.5 mm, (b) 3 mm, (c) 4.5 mm, (d) 5 mm, (e) 6 mm [53]**.**

As seen from the simulation results in Figure 27, the gap electric field has a peak at 3 mm and decreases at smaller and larger widths. There is a minor peak at 5 mm as well. This non-linear behavior in the simulation results of electric field intensity for different SRR widths can be caused by the mismatching impedances. As the SRR width changes, the signal wavelength propagates differently. This explains the slightly different resonant frequencies in Table 3. This leads to changes in the electric field intensity distribution.

The higher the combination of impedance and quality factor, the larger the voltage, and thus electric field, is achieved. However, while Q increases with width, Z_o has a non-linear behavior with the same peaks at 3 and 5 mm as the electric field strength in Figure 27. It is known the microstrip width affects the impedance of the strip [9], and that fact is used to design stripline resonators for electronics. Control of these two parameters in SRRs to optimize the gap electric field is, however, not straight forward.

The magnitude of the electric field at the edge of the discharge gap also changes for different SRR widths. This can also be primarily due to the SRR width changing the impedance of the resonator for the same input power. This impacts the magnitude of the field throughout the microstrip and it can help explain the peak at 3 mm and the significant drop in electric field between 3 and 4.5 mm in Figure 28. It is observed that a slight increase in electric field intensity occurs at 5 mm. At the same time the 5 mm device has higher impedance relative to the 4.5 and 6 mm devices.

4.2.2 Temperature and Density Measurements

Figure 26 shows a set of raw Langmuir probe I-V curves for the 4.5 mm SRR over the power range tested. Mainly, the electron retardation region becomes steeper and the electron saturation current increases with power. This results in higher electron temperatures, which is expected for higher power. Similar curves were obtained for all SRRs tested at their respective resonant frequencies. The I-V curves in Figure 26 shows the electron saturation region occurs around 10 V and the ion saturation region around -5 V.

The electron temperature for each SRR as a function of power is shown in Figure 29. The uncertainty is estimated at 5% for electron temperature, but to avoid cluttering the graphs only one set of representative error bars are shown for the 1.5 mm case. The error bars were determined by collecting multiple I-V curves at the same operating conditions (power, width, etc.), and calculating the standard deviation amongst the multiple sets of microplasma property data. Determining the error bars for the electron temperature and plasma densities is conducted through the study of the variability in repeated measurements. After three consecutive runs per data point, an analysis to determine the plasma properties is performed, and the results, in a worst case scenario, change approximately 5% in the electron temperature and 20% in the plasma densities.

When selecting the data for the plot $\ln(I_e)$, the specific points of the electron saturation used were varied to obtain an uncertainty due to point selection. The low noise data obtained resulted in low uncertainty by these measures. Langmuir probes can however have innately high uncertainty of up to 50% due to the nature of the method and theory of analysis. However, without a second method for comparison, the innate uncertainty cannot be quantified and is taken as a uniform systematic error that does not affect the relative trends and behaviors between the different SRRs.

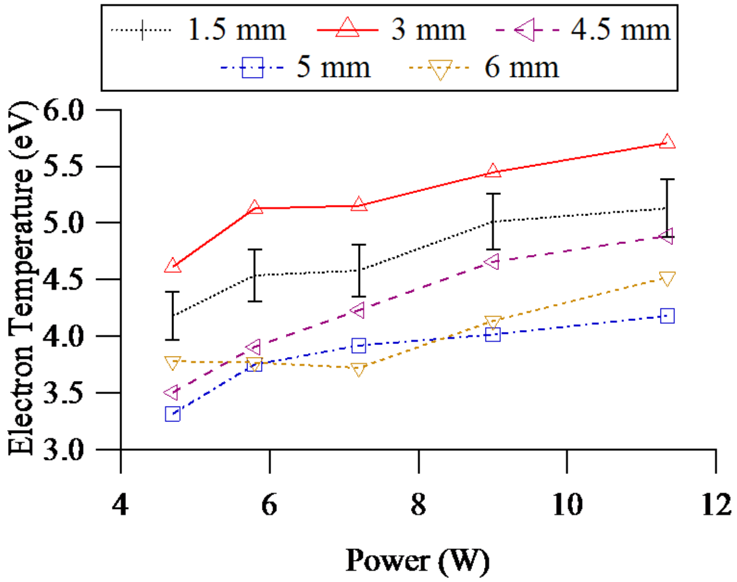

Figure 29. Electron temperature as a function of power for all SRR widths. 5% error bar shown on 1.5 mm.

From Figure 29, all devices increase in electron temperature with power and the 3 mm device had the overall highest electron temperature over the full power range, in agreement with the simulations as the 3 mm had the highest electric field intensity. This agreement is due to the 3mm having the best impedance matched with the 50 Ω microwave system. With the simulation shown previously, at 4.7 W, the 5 mm device was observed to have a slight local peak. This behavior is likely due to the higher impedance in the SRR at that width. At 4.7 W, the 5 mm may have given a locally high electric field, but the electron temperature values did not agree as the 5 mm device produced some of the lowest temperatures. Conversely, the simulation showed the 1.5 mm SRR has the lowest electric field strength along the gap, but it produced the second highest electron temperatures. This discrepancy for 1.5 mm may be due to the fringing electric fields that are not captured well by the HFSS meshing algorithm. It is likely the fringing fields play a large role in the amplification of the microplasma properties for thinner widths, but is not seen in the simulated electric fields. The higher electron temperature at 1.5 and 3 mm suggests that the electron temperature is a function of SRR width, similar to the resonant frequency, and that the trends cannot be directly predicted from field simulations. With a resonant width, optimum amplitude of the microwave signal is achieved due to better impedance matching. This leads to an increased performance of the SRR that can produce a higher electron temperature.

Comparing the measured electron temperature to Iza and Hopwood's work [6], the value obtained in this research is higher. With significantly less power, ~0.5 W, the electron temperature observed by Iza and Hopwood is 2 eV. At 11.34 W, the electron temperature found here is 5.6 eV. This increase is expected due to the higher input power. Berglund [27] obtained an electron temperature of 2.83 eV with 4.5 W. The results are thus comparable with other works. However, it is important to note that uncertainties with the single Langmuir probe data can still lead to an overestimation of electron temperature. More details can be found in the discussion.

The electron and ion densities as a function of the forward power for each SRR are shown in Figures 30 and 31.

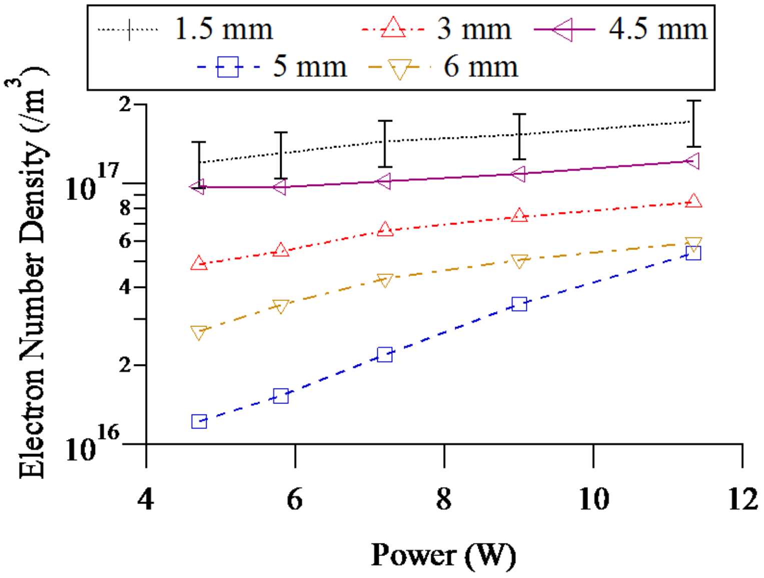

Figure 30. Electron number density over power for all SRR designs. 20% error bar on 1.5 mm.

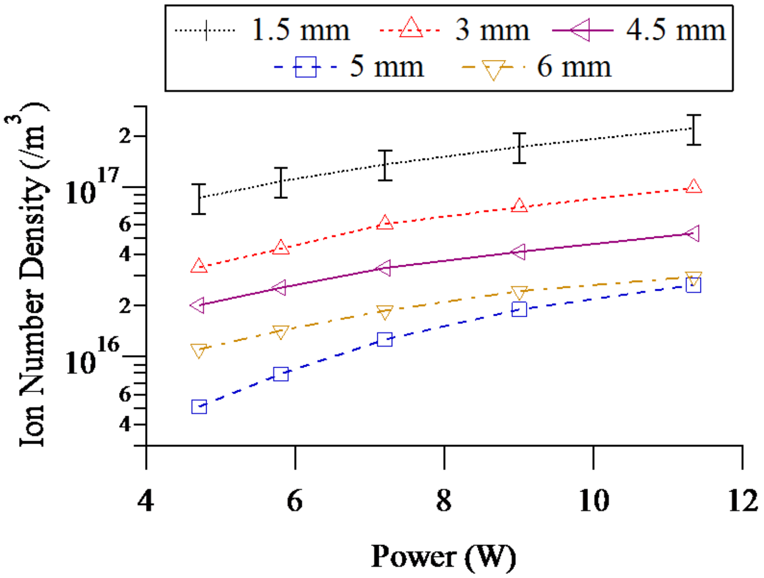

Figure 31. Ion number density over power for all SRR designs. 20% error bar on 1.5 mm.

With a 20% measurement uncertainty, determined from comparing repeated experiments, different conclusions comparing the plasma properties amongst the different rings can be obtained. However, the trends of the increasing plasma properties remained the same with an increase in power. The plasma densities experience a steady increase with power. Higher power produces higher electron temperatures which increases the ionization rate. The ion density compared to electron density shows some non-quasi-neutrality, though that may be due to uncertainty in the measurement. The ion and electron densities increase at a similar rate for all widths except for 5 mm, suggesting the change in ionization rate is mostly independent of width. As seen in Figures 28 and 29, the highest densities are achieved by the 1.5 mm SRR.

4.2.3 Discussion

When comparing the electron temperature and plasma density of the devices, there are some discrepancies. The 1.5 mm width had the highest plasma density while the 3 mm width obtaining the highest electron temperature. The 3 and 4.5 mm SRRs achieved the second highest ion and electron number density, respectively, while the 3 mm temperatures were significantly higher than the 4.5 mm. On the other hand, the 5 mm device had the lowest density and some of the lowest recorded electron temperatures. Overall, the trend appears to be a higher electron temperature produces a lower number density for the devices tested. It is important to take into consideration the impact on the conclusions from the resulting data due to the uncertainties. The goal of this research is to determine the highest performing devices. This would interchange between the 1.5 and the 3 mm device within the uncertainty bounds. A continuation of this research with an in-depth uncertainty analysis can lead to a proper conclusion on the best-performing device based on the microplasma properties determined.

As seen by Berglund [27], an electron temperature of 2.83 eV also obtained an ion density of 5.7 x 10^{17} /m^3. This plasma density data is higher compared to the 1.6 x 10^{17} /m^3 obtained here; however, the operating frequency of Berglund is significantly higher, 2.6 – 2.7 GHz, which may play a role into the variations. Zhu, while comparing probe theory to optical emission spectroscopy, determined electron temperatures from 1-4 eV with a argon, xenon, neon mixture at 13.56 MHz and 100 W [54]. Iza and Hopwood also obtained ion density measurements within the range of 2.0 x 10^{16} /m^3 to 1.2 x 10^{17} /m^3 with a power from 0.2 to 1.0 W. This was also accomplished at a range of pressures, from 100 mTorr to 400 mTorr [6].

The observations and comparisons made between the plasma properties of the various devices tested can be explained by the resonant frequency, impedance, and the other electrical properties of the SRR. As mentioned, the device is intended to be half the wavelength of the driving frequency and the input impedance into the SRR is 50 Ohms from the microwave source. However, the microstrip characteristic impedance and the quality factor is a driving factor in determining the voltage and thus electric field across the gap. As SRR width increases, the characteristic impedance has a non-monotonic behavior with highest values at 3 and 5 mm. The quality factor increases with width, but at a slow rate at large widths. The quality factor decreases in narrow microstrips due to increased conduction and radiation losses. Thus maximizing both quality factor and impedance to improve gap voltage and presumably plasma properties is not a simple matter of increasing width to maximize quality factor.

In this experiment, the 3 mm device proved to have a higher electron temperature while the 1.5 mm device had a higher density compared to the other widths. This is mainly due to the characteristic impedance as the quality factor for the 3 mm device was lower than the larger widths. The concept of resonance plays the primary role in this research. A resonant frequency was found and a unique quality factor was determined for each device to obtain the appropriate phase angle. Good resonant behavior is observed from the 3 mm, while the 1.5 mm device shows poor resonance, yet, obtains a higher plasma density. This may be due to the smaller widths generating a more compact plasma at a given power level. Thus while the smaller devices had a locally higher density, the larger devices may have a higher total density but over a larger volume. Spatial measurements are required to determine the extent of the plasma volume.

4.3 Experiment 2: Nested Ring CSRR

Understanding the microplasma generation behavior of single SRRs can be useful for the purpose of implementation into micropropulsion. However, with ignition focused at the outer ring discharge gap, it will create a spatially non-uniform plasma, which can decrease thruster performance. This led to the idea that with the use of a nested concentric ring subject to a coupling effect from the powered ring, a secondary ignition can occur. This secondary ignition can potentially improve plasma properties and provide uniformity to the plasma encompassing the entire device, simplifying a micropropulsion design. With the incorporation of a second nested SRR on the same substrate, impedance and resonant frequencies are affected. Also, as the larger SRR is powered, a coupling phenomenon is observed. The proximity coupling effect phenomenon is caused by the fringing fields emitted from the surface of the powered outer ring of the CSRR [6]. Fringing fields are the presence of electric fields along the edges of an antenna, in this case, the CSRR inner and outer diameters. Any nearby conducting material can generate its own electric field when exposed to fringing electric fields. Other research discusses this proximity coupling effect and the likeliness that it is due to nearby fringing fields [52], [53]. Gregorio discusses the fringing of the electric field and refers to it as the charge accumulation effect associated with the interaction between the transmission line and the end gap [28]. Based on this work, the inner-ring spacing can potentially be represented as a capacitive element in an electric circuit. Regardless, all indications relay that the fringing electric fields present play this role in a CSRR. Interestingly, CSRR work involving the development of a periodic array to study magnetic resonant frequencies also show inductances arise from the conducting rings and gap between inner and outer rings [55]. During operation, the plasma generated by the larger ring will propagate into the discharge gap of the second concentric harmonic SRR causing a second plasma ignition, thus increasing the net plasma volume. The plasma volume obtained from a single SRR is typically concentrated near the discharge gap, leading to a spatially non-uniform microplasma. Figure 32 shows the operating CSRR and SRR, observing the visible change in plasma volume with the operation of the CSRR compared to the SRR.

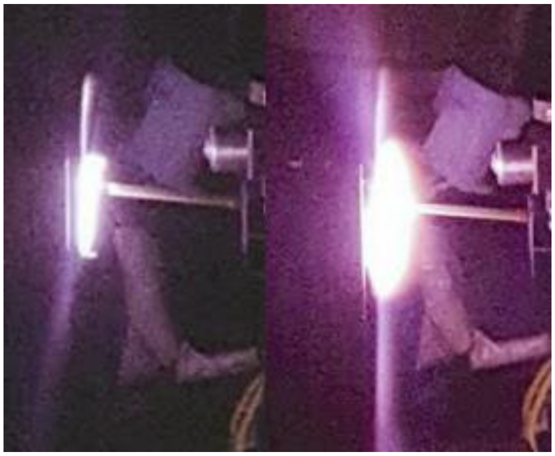

Figure 32. Photo of operating (a)SRR and (b)CSRR at ~10 W and 796 MHz.

As mentioned, this particular design can be useful when implemented inside a thruster chamber. With a second SRR oriented 180° from the original, the plasma can expand to a larger volume of the microthruster chamber. The plasma density will also increase as ionization is induced over a larger volume of gas. Figure 33 below displays a diagram of a notional concentric ring SRR [7]. The behavior in microplasma production has not yet been examined with concentric SRR devices. In fact, this dissertation presents the initial work using CSRR microplasmas.

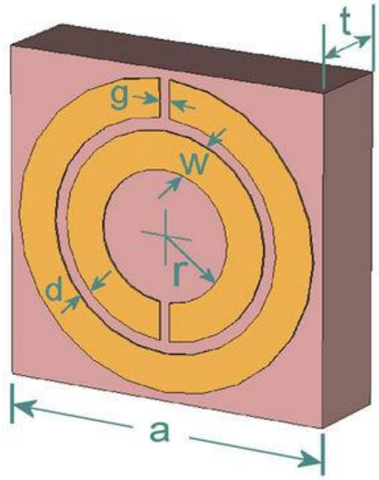

Figure 33. Concentric SRR design from Castro et. al.[7]**.**

The development of the concentric ring design provides new objectives for the improved operation of a microstrip resonator device. A new design parameter that can be focused on is the inner-ring spacing. The concentric ring should be a harmonic of the powered ring; however, by decreasing the inner-ring spacing, a stronger coupling between the concentric rings can be achieved [55]. This may assist the ionization process and produce a higher energetic plasma. In addition to this concept, the idea of nested rings draws the possibility that a third or fourth concentric ring can also induce an improved microplasma. This concept has been studied before with linear microstrip technology; however, utilizing a circular geometry may prove to have a significant advantage as the gap placements can be 180° from the previously nested ring. Figure 34 below provides a diagram for this concept.

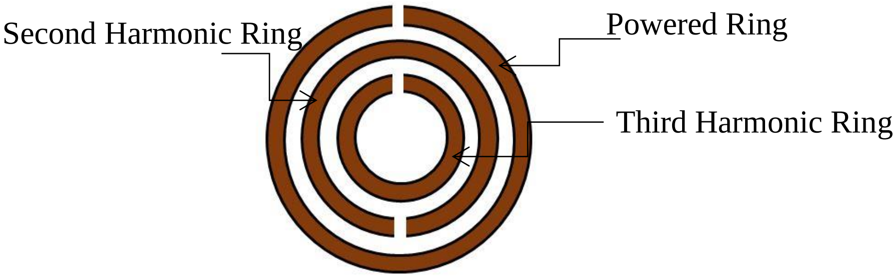

Figure 34. Multiple concentric ring concept design.

Design parameters such as frequency, geometric characteristics, dielectric constant and thickness, inner-ring spacing, etc., will all need to be considered to ensure optimization in microplasma production.

4.3.1 SRR and CSRR Device Characteristics

The SRR and CSRR devices in this work were fabricated on RT/Duroid 6010 laminate as the substrate. A nested harmonic ring is designed concentric with a primary SRR and is fabricated on the substrate for the CSRR configuration. The central conductor of an SMA connector is soldered to the primary SRR (outer ring) while the grounded body is soldered to the back plane. Figure 35 shows a schematic of the split ring resonator and the concentric split ring resonator designs. Both designs have the same outer-ring, the primary distinction is the implementation of the nested ring for the CSRR.

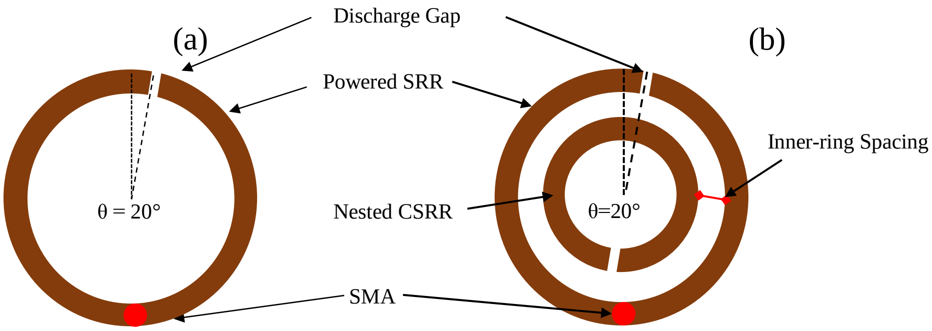

Figure 35. Schematic of SRR design (a) and CSRR design (b).

Similar geometrical characteristics are applied for the SRR and outer ring of the CSRR. A uniform 500 micron discharge gap was used for the SRRs and CSRRs. All devices were geometrically designed for an input microwave frequency of 700 MHz. However, this differs from the operational center frequency (796 MHz). This is likely due to manufacturing imperfections and impedance losses in the system. After the devices were fabricated, the resonant frequency was experimentally found as the frequency at the maximum forward power with a digital Bird power sensor. Resonant frequencies determined for the SRR and CSRR were 820 MHz and 790 MHz, respectively. However, 796 MHz was chosen as a center frequency where both devices achieved a microplasma for the experimentation. When designing the SRR based on the input microwave desired, the discharge gap is placed such that the microwave electric field is maximum at one end of the gap and minimum at the other end. The schematic of the SRR wave propagation can be seen in Figure 19. With this behavior, a maximum potential difference can be achieved across the gap necessary to achieve plasma ignition.

The nested CSRR exhibits similar geometrical characteristics of the powered SRR. The location of the secondary discharge gap of the nested ring is 180° from the powered ring discharge gap. Alternative discharge gap placements for the second ring are examined using HFSS; however, shifting the phase angle from 180° showed to decrease the overall electric field intensities. As the electromagnetic radiation is coupled from the outer ring to the inner ring, a signal then propagates to the secondary discharge gap of the nested ring potentially producing a second point of ionization.

4.3.2 Simulation Results

The CSRR was designed based on simulations in ANSYS High Frequency Structure Simulator (HFSS). The phase angle and inner ring spacing were adjusted in the model to obtain maximum gap electric fields. It is unclear if the theoretical design equations developed for a single SRR is applicable to a CSRR. However, the impedance of an SRR and CSRR is experimentally determined and the impact of the nested ring onto the quality factor is examined. All electrical characteristics for both devices are presented in this dissertation. The quality factor can be found from Equation (4). Methods for calculating attenuation factor can be found in reference [40].

As the microwave propagates through the outer powered SRR, the electric field intensity behavior can be modeled using HFSS. When the outer ring is powered, an electric field buildup is also observed in the isolated inner ring of the CSRR. This is likely due to a proximity electromagnetic coupling effect fringing from the powered ring onto the nested ring. The inner ring spacing was varied using HFSS to determine at what distance the coupling will continue to be observed without building peak electric field intensities around the circumference of the ring. Some examples of this case is shown in Figure 36 where the inner-ring spacing is substantially small that the only interactions of the E-field observable are within the inner ring space. This case is also documented in the Appendix displaying peak electric field values obtained for the same device while varying inner-ring spacing. For the purpose of this research, 1 mm spacing was used due to fabrication limitations and results from the simulations. Utilizing a 1 mm spacing is sufficient for effective proximity coupling while maintaining peak electric field potentials near the discharge gaps.

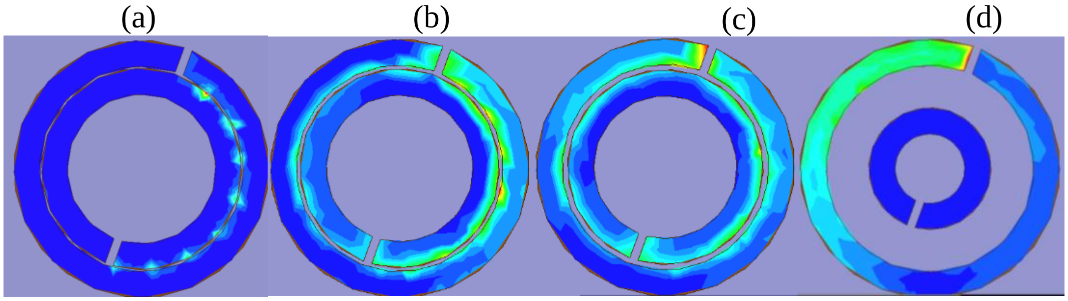

Figure 36. CSRR with 0.1 mm (a), 0.2 mm (b), 0.3 mm (c), and 5 mm (d), inner-ring spacing, inducing interactions along circumference of the inner ring spaces. Same color scale for all figures.

Conceptually, when operating at the resonant frequency, plasma ignition should occur within the discharge gaps of the primary and secondary SRR. This multiple ignition behavior was first observed with linear resonator arrays by Zhang[8]. As one linear resonator is ignited, any other resonators in proximity achieved an ignition. This phenomenon propagated along a linear resonator array showing multiple ignitions using a propagating coupling effect. A disadvantage of this linear resonator array structure is the dissipating microplasma generated along the array as losses occur in the electromagnetic field waves due to the coupling to multiple devices. This work uses the same coupling effect, but with a compact CSRR. With a circular geometry, the discharge gaps in all concentric rings can contribute to the same microplasma versus having multiple ignitions across an array.

A 700 MHz single SRR is setup within HFSS and given an input power of 10 W. Figure 37a and Figure 37b shows the vector plot of the electric field for the SRR and CSRR at 796 MHz, respectively. This was chosen for consistency between the operational frequencies in the plasma property data and the simulations. An inner-ring spacing of 1 mm is setup for the CSRR. All other geometrical characteristics of the CSRR are replicated from the SRR device. Figure 38a and 38b show the spatial profile of the electric field intensities for the SRR and CSRR, respectively. From the figures, it is clear the electric field intensity peaks at the discharge gaps of both devices within their respective ring. This includes the powered ring and the nested ring for the CSRR. Even though the outer ring geometries between the SRR and CSRR are the same, the electric field intensities of the SRR are larger than the CSRR. The electric field intensity at the discharge gap for the SRR peaks at 4.69 x 10^4 V/m. For the powered ring of the CSRR, the gap electric field reached 3.37 x 10^4 V/m. The nested ring of the CSRR obtained a gap electric field intensity of 8.44 x 10^3 V/m. It is important to understand these results are generated specific to a CSRR with 1 mm inner-ring spacing. This value was chosen as it seemed to perform the best when ranging the spacing from 0.1 mm to 5 mm. At 0.1 mm, the device has a strong interaction along the circumference of the rings, where higher electric field intensity is observed, as seen in Figure 36. However, this circumference interaction minimizes the power delivery to the discharge gap. Closer to 5 mm, the interaction becomes minimal and the nested ring has no electric field.

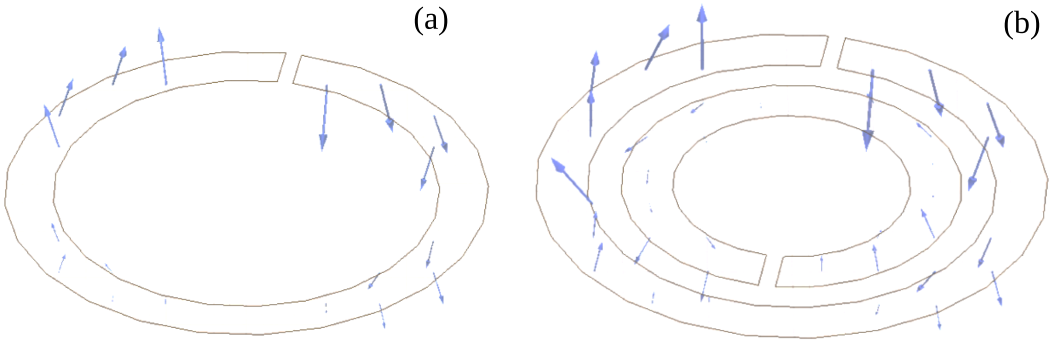

Figure 37. a) Single SRR with vector plot operating at 796 MHz. b) CSRR with vector plot operating at 796 MHz.

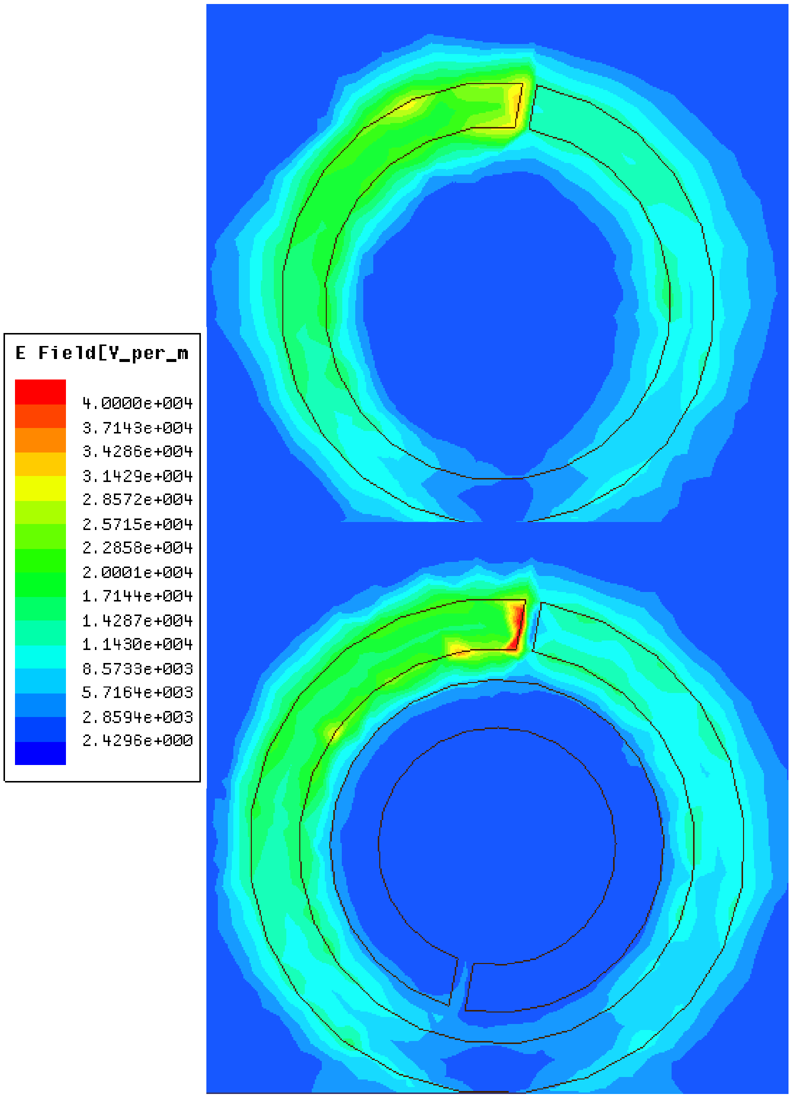

Figure 38. a) SRR HFSS Electric Field Intensity Simulation at 796 MHz. b) CSRR Electric Field Intensity Simulation at 796 MHz.

The proximity to the powered ring appears to have the largest impact on the coupling effect. As the powered ring is given a microwave signal and the electric field is produced along the ring, a fringing field effect is emitted from the surface of the SRR[6]. Any conducting material within the fringing fields is susceptible to generating its own electric field within its structure. Once the nested ring sees this source, the field is propagated to the discharge gap as if it was its own SRR. Other research agrees that the proximity coupling is likely due to the fringing electric fields from the powered ring to any sort of nearby conducting material [56]. Both devices exhibit rapid change in electric field intensity at the gap. This corresponds to the magnitude of the microwave encountered at each end of the discharge gap.

The vectors in Figure 37 correspond to the electric field output from the microstrip. The vector directions are travelling in a wave that is 180° out of phase near the discharge gaps. The magnitude of the vectors increases from one end of the discharge gap to the other, while propagating along the ring. This is expected as the microwave propagation can be represented by a standing wave around the ring displaying the potential difference across the gap as shown in Figure 19. The nested ring also exhibits the opposing field direction at the gap, though it is opposite from the powered ring. Combining the vector profile and the spatial analysis, it is apparent the CSRR obtains a larger potential difference at the primary discharge gap. It is important to note that the maximum electric field magnitude calculated by HFSS of the SRR corresponds to the electric field not directly at the discharge gap, but on the inside surface of the left end where ionization does not occur. Thus the actual SRR gap field strength is lower than Figure 38's legend would indicate. The electric field intensities recorded at the higher powered edge of the discharge gap for the SRR primary is 2.98×10^4 V/m while the CSRR primary and secondary discharge gaps are 3.37×10^4 V/m and 4.22×10^3 V/m, respectively. Also, the gap potential change within the gaps is observed higher for the CSRR compared to SRR. These magnitudes are calculated to be 3.83×10^4 V/m and 4.22×10^4 V/m for the SRR and CSRR, respectively.

Magnetic field simulations obtained show significant impact of the nested ring on the induced magnetic field behavior. As shown in Figure 39, the SRR magnetic field vectors travel across the device from the left to right side. For the CSRR, the majority of the magnetic field vectors travel through the ring towards the direction of the operating microplasma. This change in magnetic field direction reflects the current direction while propagating through the ring. Using right-hand rule, it is apparent that in the SRR, the propagation of the wave current on the left and right side of the SMA input travel in the same direction, going away from the discharge gap. The CSRR assumes a current propagating in one direction around the loop, counterclockwise for the primary and secondary rings. The change in wave direction is likely due to the asymmetrical structure as a phase angle is present in both devices. However, a CSRR has symmetrical characteristics due to the presence of the nested ring. As transmittance of the microwave occurs from the discharge gap of the primary ring to the secondary ring, the secondary ring represents a symmetry structure with no phase shift, leading to one-direction wave propagation. Wave propagation of a SRR can be manipulated to travel in arbitrary trajectories according to Sun [31]. In this experiment, the microwave is inputted directly into the operating device. The magnitude of the CSRR magnetic field is larger than the SRR, likely due to the superposition of the magnetic field from the primary and secondary rings. Also, the magnitude of the magnetic field is likely to have sufficient impact on the operating microplasma. The peak intensities in Figure 39 reflect the magnetic field activity near the SMA connector which is not shown. The majority of the ring shows magnetic field magnitudes of approximately 500 A/m (6 G) and 940 A/m (12 G) for the SRR and CSRR, respectively.

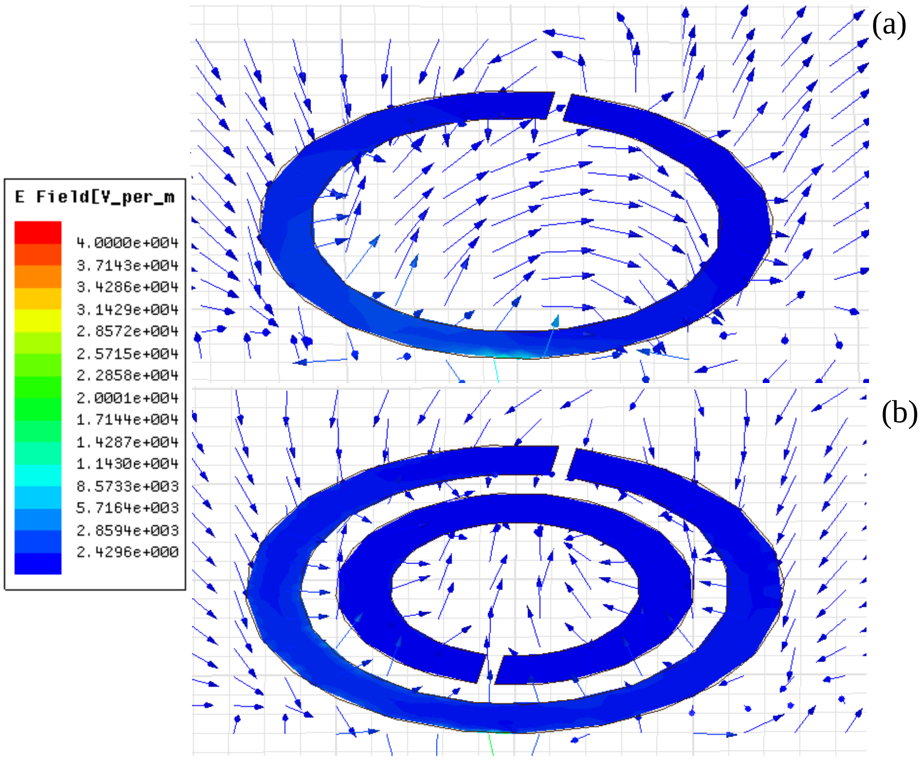

Figure 39. Magnetic field vector simulations of a) SRR and b) CSRR.

4.3.3 SRR vs. CSRR Discharge Gap Probe Measurements

A primary focus of this research is to understand the impact of the coupling effect induced by the concentric ring on the generated microplasma. The CSRR microplasma volume was visually observed to expand. Double Langmuir probe measurements were taken above the discharge gaps of the outer rings in both configurations to determine if the CSRR produces higher temperatures and/or densities. From the experimental measurements of our densities, it was determine that with an argon pressure of ~350 mTorr, collisionality values varied from 0.001 to 0.025, placing the plasma in the collisionless regime [41]. Table 1 shows the results from the probe at the gaps.

Table 5. CSRR vs SRR Plasma Properties with ~10 W at ~350 mTorr-Ar at 4 mm above the outer gap.

Plasma Property	SRR	CSRR
Operating Frequency (MHz)	796	796
Quality Factor	49	71
Electron Temperature (eV)	8.2	9.5
Plasma Number Density (/m^3)	1.2 x 10^{17}	8.5 x 10^{16}

It is important to acknowledge that with the addition of the nested ring, a significant shift in the resonant frequency is observed. The presence of the additional ring changes the electrical characteristics of the device, in particular, the impedance. The impedance for the SRR and CSRR was measured using a network analyzer. The SRR impedance was found to be 48.9 Ω while the CSRR was 56 Ω at 796 MHz. It is noted that these devices show significantly improved impedances compared to Experiment 1; likely, this is due to improved fabrication methods and the lower frequency requirements. With lower frequencies, larger wavelengths are delivered to the device, meaning larger resonator structures must be fabricated. With a larger structure, the increased length of the resonator leads to an increase in inductance, improving the magnetic energy stored in the resonator [50]. With increased capacitance, via balancing the resonant width, and increased inductance, the strength and bandwidth of the resonance can be preserved [48]. As capacitive and inductive elements also contribute to the impedance of the resonator, the impact of using lower frequency ring resonators is observed in Experiment 2, showing better matching impedances.

For the purpose of conducting a comparison between the devices, the SRR and CSRR were operated at the same frequencies. From Table 5, the electron temperature and plasma densities are the primary focus. The electron temperature decreases by ~1 eV in the SRR. This is unexpected as the SRR produced some higher electric field intensity values, particularly near the outer ring discharge gap. However; the potential change at the discharge gap of the outer ring for the CSRR seems to be significantly larger considering the vector and spatial profiles. The coupling effect enhances the plasma properties as the electric field propagates into the nested ring. This occurs as the increased impedance of the device operating at the same frequency enables the microwave to reach higher magnitude in potential in the capacitively coupled discharge gap. It is observed from physical inspection the microplasma produced by the CSRR, while larger in volume, exhibited a lower density in comparison to the SRR. Higher plasma populations are expected as the distribution of electric field propagating into the nested ring provides a secondary point of ignition for the plasma generated by the powered ring. However, this distribution also decreases the overall magnitude of the electric field, reducing the energy delivered necessary for producing ions. With the increased electric field activity in the CSRR due to the coupled nested ring, the population densities are affected. Based on the vector formation plots, the electric field shifts the population distribution similarly as the visible plasma volume grows.

4.3.4 Electron Temperature Measurements

Probes distribution plots were developed to understand the distribution of the plasma properties over the area of the SRR and CSRR. Multiple distribution plots were obtained comparing the two devices and observing the impact of the nested ring in the CSRR. Figure 40 and 41 displays the electron temperature data for the SRR and CSRR, respectively, while operating at 796 MHz. The contour plots show two points of ionization for the CSRR, due to the operation of the secondary nested ring. Better uniformity is also observed in the CSRR with the operation of a secondary gap. The electron temperature profile of the CSRR exhibited a secondary peak with a lower magnitude compared to the primary ring peak. Corresponding to the simulation, the electric field intensity for the CSRR decreased compared to the SRR, yet a higher potential change is observed in the primary discharge gap. This likely results in an increase in electron temperature as a larger oscillating electric field energy is applied from the device. The coupling effect caused by the presence of the nested ring may absorb energy from the powered ring, leading to lower electric field intensities. This is also demonstrated by the impedance change. A shift in impedance changes the behavior in the microwave propagation leading to a larger potential difference at the gap, regardless of the lower observed intensities. This is again observed in the voltage gap equation developed by Iza and Hopwood. The secondary ignition also leads to a more uniform plasma. The coupling effect is also observed in the linear resonator work by Zhang [8]. The total power delivered by the microwave source circuit to the plasma is distributed amongst multiple points of ionization. However, as Zhang's research utilized an array of resonators, the plasma noticeably dissipates further down the array. Here, a ring offers a geometrical advantage allowing better microwave and microplasma coupling.

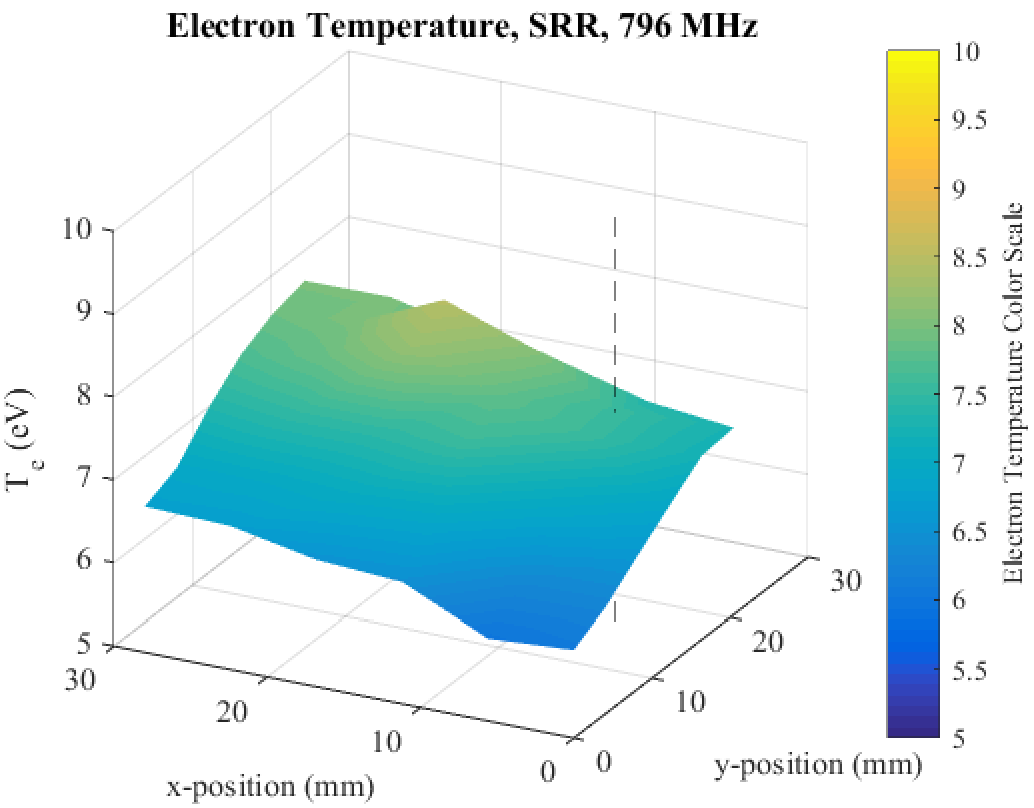

Figure 40. SRR Electron Temperature Distribution Contour Plot at 796 MHz with ~10 W.

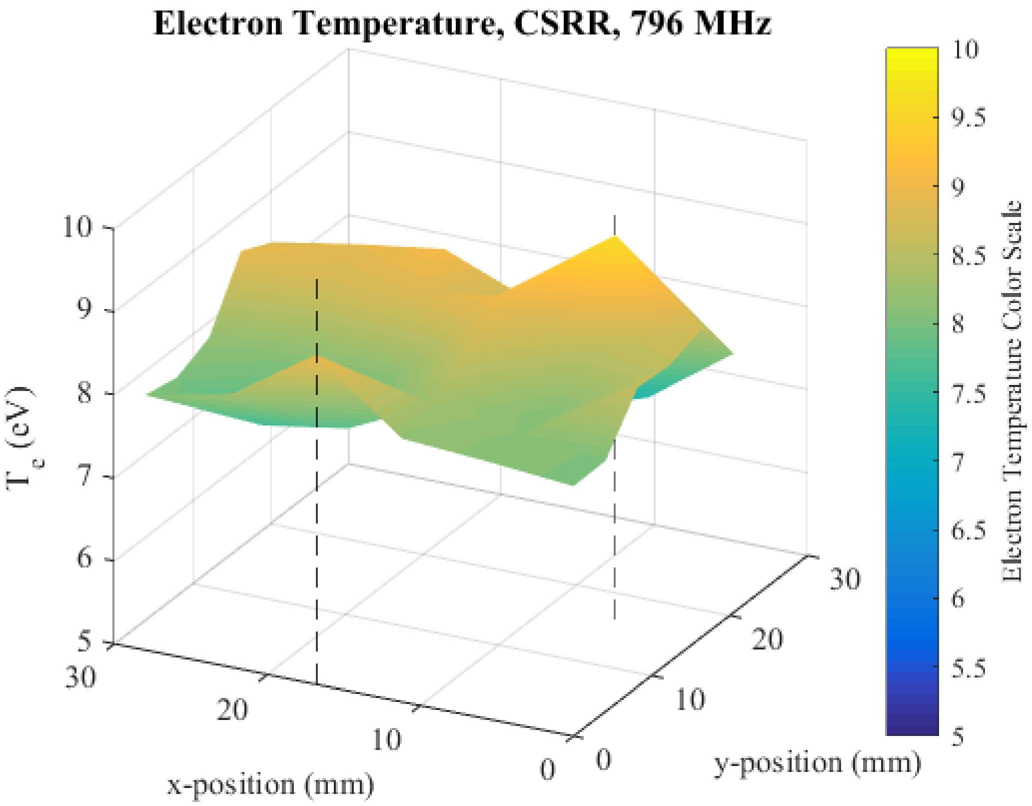

Figure 41. CSRR Electron Temperature Distribution Contour Plot at 796 MHz with ~10 W.

4.3.5 Plasma Number Density Measurements

Figure 42 and 43 display the plasma number density data distribution plots obtained at 796 MHz for the SRR and CSRR, respectively. The density displayed a different behavior to the electron temperature as the peaks favored the center of the device.

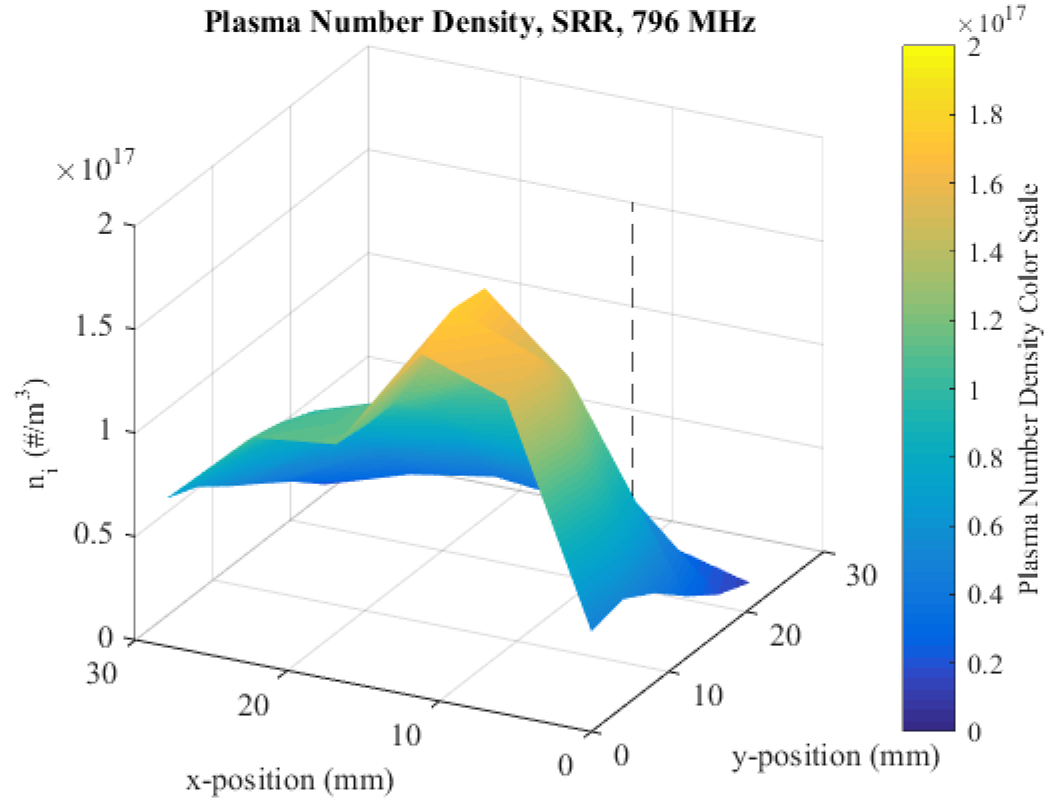

Figure 42. SRR Plasma Number Density Distribution Contour Plot at 796 MHz with ~10 W.

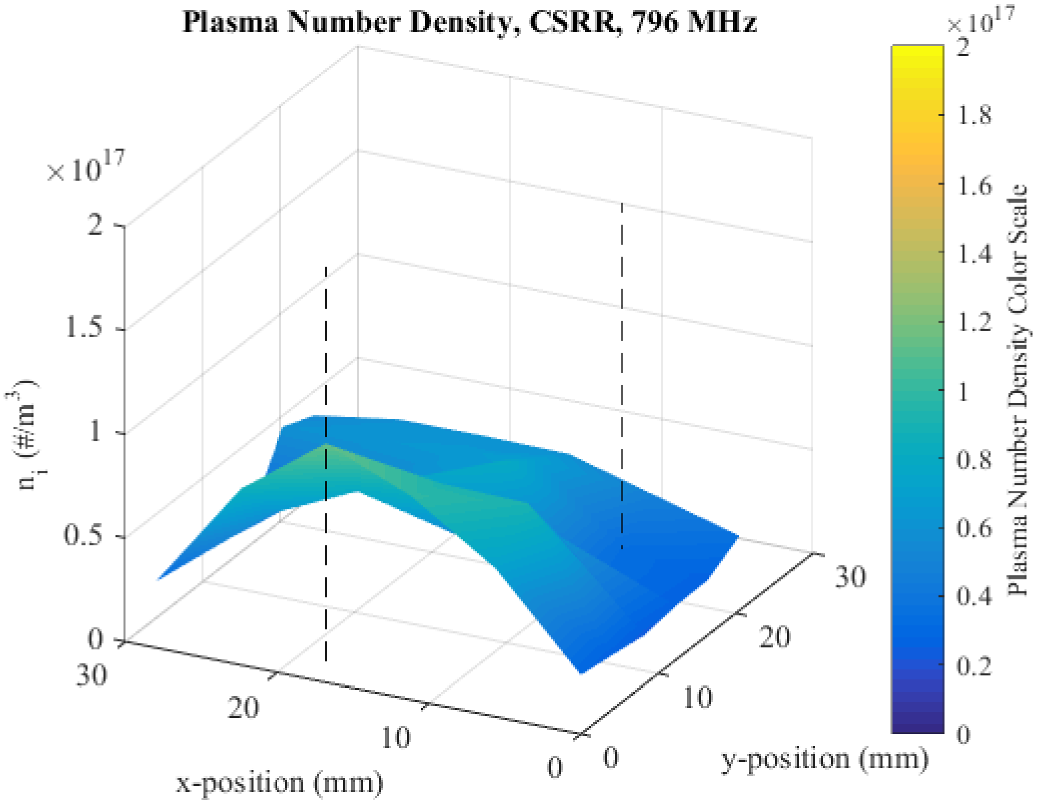

Figure 43. CSRR Plasma Number Density Distribution Contour Plot at 796 MHz with ~10 W.

With the plasma production distributed above the device, the SRR produced a significant amount of particles favoring the center of the device. This is also observed with the population of the CSRR with some activity near the secondary gap. This can be understood with the activity of the magnetic field as it propagates differently on each device. The magnitude of the magnetic field is weaker for the SRR compared to the CSRR; therefore, as the plasma becomes magnetized, the electron Larmor radius decreases for stronger magnetic fields. This is expressed in the equation, $L=mv/qB$, where L is the Larmor radius, m is the mass of the electron, v is the thermal velocity of the electron corresponding to the plasma properties obtained, and B is the given simulated magnetic field strength. Larger B leads to smaller radii pulling the plasma closer to the magnetic field lines, justifying the physical shift of the plasma population. As stronger magnetic field lines are determined closer to the secondary gap, the plasma population favors this area. With weaker magnetic fields from the SRR, larger radii are achieved and with magnetic field lines crossing the center of the device, plasma populations are subject to favor this area. Another consideration with the simulated magnetic field strengths is the magnitude of the Larmor radius produced; this is comparable to the inner radial dimension of the device (~8.5 mm) possibly factoring into the presence of plasma population near the center.

4.3.6 Discussion

The probe measurements clearly show a second point of ionization occurs at the discharge gap of the nested CSRR. This is presented by the double peaks in the electron temperature data. As the microwave inputs into the powered ring, this outer ring behaves as a single SRR. Fringing fields emitted from the outer ring transmit to the inner nested ring of the CSRR. With the higher electric field intensities observed near the discharge gap of the powered ring, it is likely the majority of the proximity coupling between the rings occurs at this gap. Using HFSS, the nested ring dimensions are assigned to ensure the microwave signal is in phase with the secondary discharge gap. With the coupled transmission, the microwave now propagates throughout the nested ring leading to the production of the second point of ionization. The advantage in this geometry is a compact plasma volume compared to a linear array. This may be useful for processes requiring an energetic microplasma with an expanded volume but compact physical size. However, further research is required in order to achieve uniformity across the device as there are significant maximums and minimums in the plasma properties. With the operation of the

CSRR, a more uniform plasma in terms of electron temperature has been observed. These results suggest that the coupling behavior can extend into more nested rings, thereby creating more points of ionization.

This will also lead to a disseminating electric field leading to an overall decrease of intensity throughout the device. This is observed in the HFSS simulations. Compared to the SRR, the CSRR achieves higher electron temperatures due to larger potential changes within the discharge gaps, regardless of lower electric field intensities. Yet, the SRR achieves higher plasma number densities as the presence of electric field directly above the antenna can potentially counter the density measurements. With this understanding, CSRRs produce higher energy microplasmas compared to SRRs by inducing an impedance change in the microwave leading to a higher potential difference across the discharge gap. This is observed in conjunction of the spatial and vector analysis as high magnitude vectors in opposition are observed in the CSRR; this is not observed for the SRR as a large peak is observed on one end of the discharge gap. This combined with a secondary point of ionization due to the coupling phenomenon leads to an expanded and distributed microplasma.

With electric field activity such as fringing fields non-perpendicular to the device, plasma populations above the conducting antennas can physically shift due to the electrostatic forces. This explains the areas within the profiles that show shifts in electron temperature or plasma densities. Vector formations showing the continuous propagation of electric fields away from the discharge gap causes the change in this plasma property profile. Metamaterials, such as CSRRs, have shown to manipulate electromagnetic fields into desired configurations [32]. Other research also looks at the interaction of electric and magnetic fields when running with a TM (transverse mode) wave, referring to high frequency and microwave signals [31]. However, exploration with the presence of a plasma is limited. With the dynamic electrical properties of a plasma, it is expected that the particles can be physically manipulated by the emitting fields from the CSRR. Lower energy particles are more susceptible to be physically shifted as less energy from the electric field is required.

4.4 Experiment 3: Frequency Effect on CSRR Microplasma

When operating a resonator structure, there is a particular resonant frequency where optimal operation occurs. CSRRs have shown a capability to operate at off-resonant frequencies meaning a microplasma can be sustained over a small frequency range. This leads to the importance of the effect of frequency on the microplasma properties of a CSRR, particularly for practical satellite applications. In telecommunications, 2.2 – 2.29 GHz is a standard frequency band (S-band) used for downlinks communications by modern satellites. If an CSRR-based thruster is designed to operate at those frequencies, it becomes possible to directly use existing on-board communications equipment to power the thruster, thus reducing system mass. Operating at these high frequencies reduces the physical size of the CSRR to ~ 1.3 cm in diameter, which allows for arrays of CSRRs for increased plasma production and thus thrust, or reduces the size and thus mass of a single CSRR thruster. However, while the CSRR-based thruster can be designed for a resonant frequency of say 2.25 GHz, the actually allowed operating frequency of the transmitter may vary within the S-band range. Thus understanding how the microplasma changes at slightly off-resonant frequencies is needed.

It is important to note that due to capabilities within our lab, the desired communications frequencies of 2 GHz could not be achieved. The design of the CSRR was shifted to be below our capable operating frequency (1000 MHz) sufficiently so that frequency variations and ranges can be experimented. The CSRRs from Experiment 2 were thus used with a resonant frequency of 796 MHz with a frequency range of ±10 MHz. This is done to obtain a perspective of the impact of the variation of frequency while operating a CSRR. An increase in electron temperature and plasma densities is expected as a higher frequency leads to higher energetic particles [25], [57].

4.4.1 Simulation Results

ANSYS HFSS was used to model the electric field behavior as the microwave propagates through the CSRR at the different frequencies. Theoretically, microplasma generation is only possible when operating at the resonant frequency. However, the results obtain here shows that ionization can occur over a range of frequencies off resonant.

Figure 44 shows the HFSS simulation results at 10 W for a frequency range from 786 to 806 MHz along with the corresponding vector plots. The electric field distribution plots show the field intensity peaks at the discharge gaps of both rings and the vector plots show the directional behavior of the electric field as it propagates around the primary and secondary rings. The values for these electric field intensities are tabulated in Table 6. Figure 45 shows the vector profile of the electric field simulations.

Table 6. Electric field intensities in the discharge gaps of the CSRR primary and secondary rings.

Frequency	CSRR – Primary (V/m)	CSRR – Secondary (V/m)
786	3.11×10^4	3.89×10^3
796	3.37×10^4	4.22×10^3
806	2.99×10^4	3.75×10^3

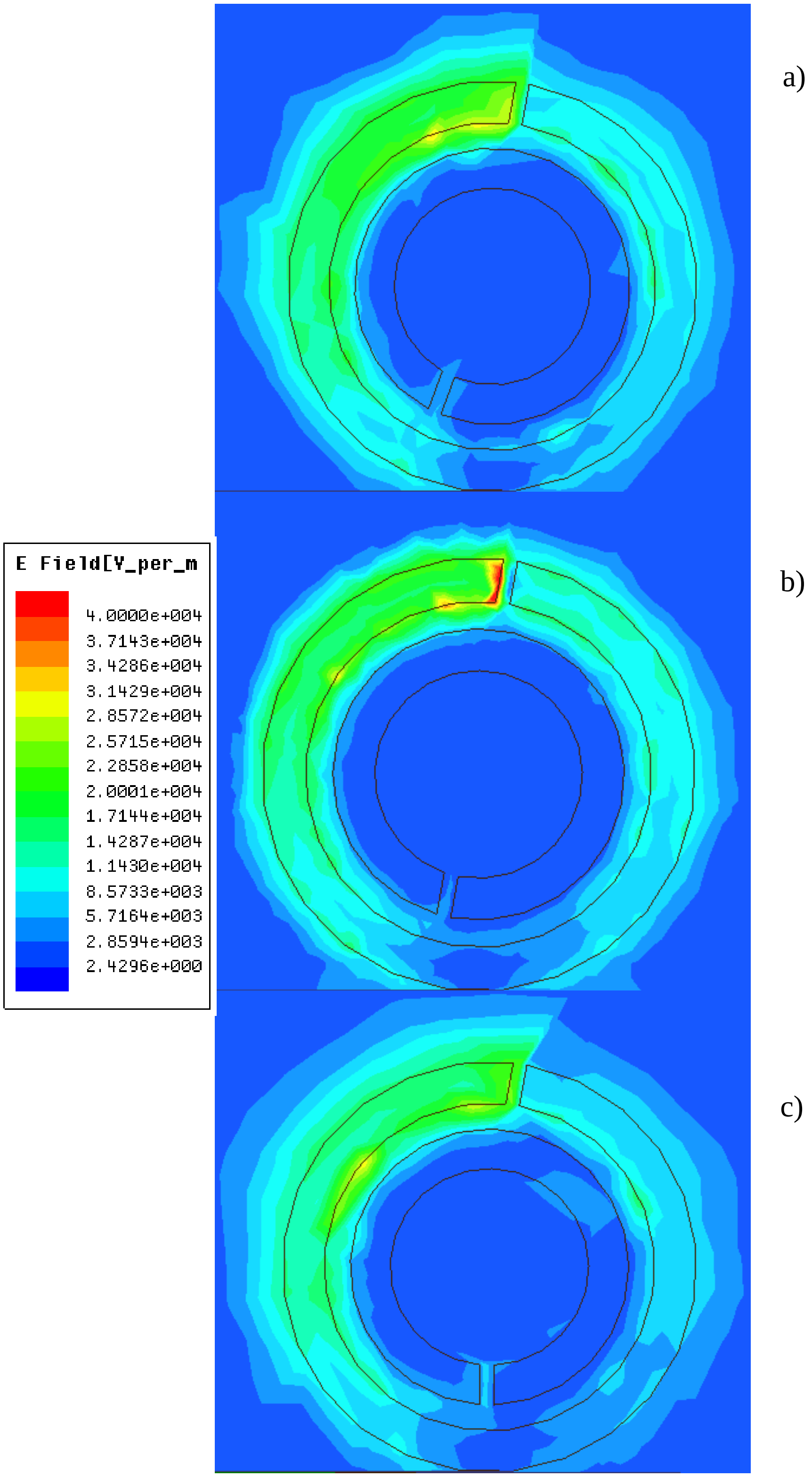

Figure 44. HFSS Spatial Simulations of CSRR with varying frequency. a) 786 MHz, b) 796 MHz, c) 806 MHz.

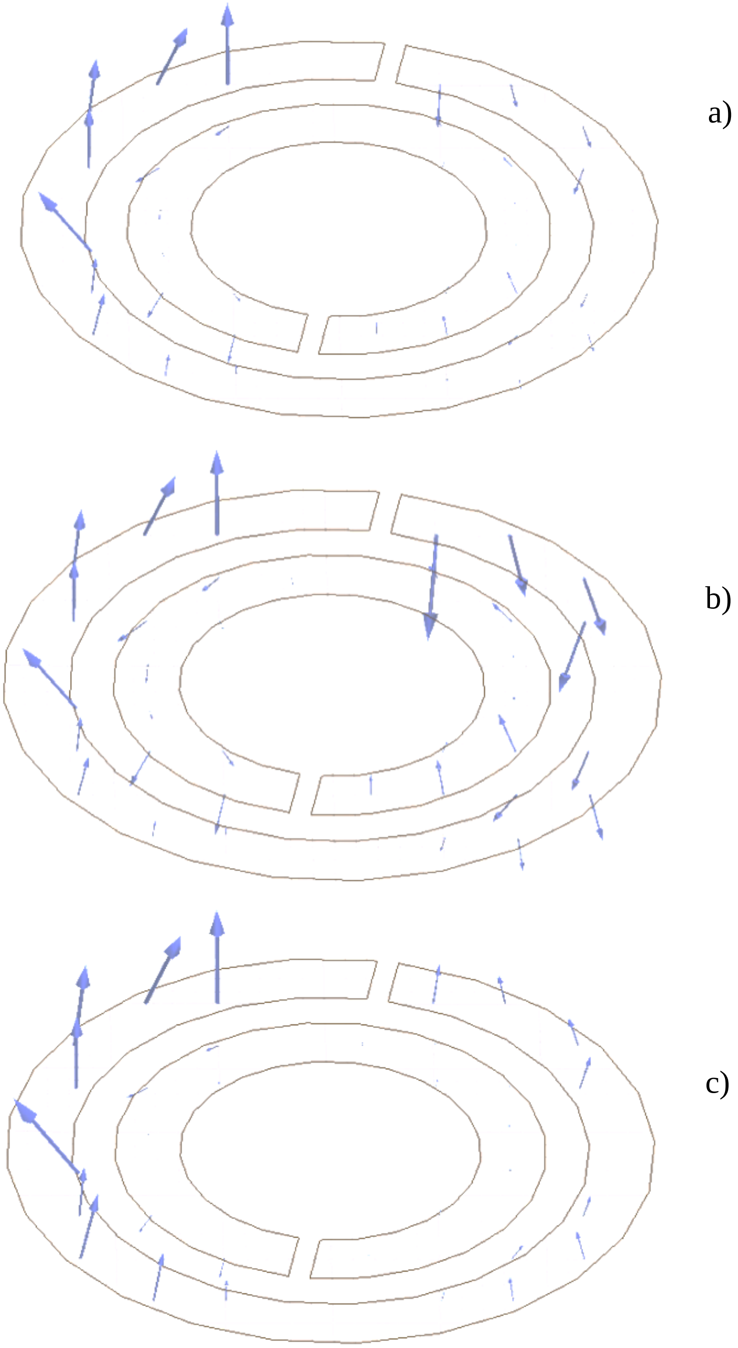

Figure 45. HFSS Vector Simulations of CSRR with varying frequency. a) 786 MHz, b) 796 MHz, c) 806 MHz.

With the Langmuir probe data obtained for CSRR sources ranging in frequency, or while operating various concentric rings, the production of the microplasma can be understood. With an increase in frequency, the oscillations of the electrons within the atoms are expected to lead to an increase in ionization. Hence, with an increase of resonant frequency of the CSRR, the optimal operation of the source is predicted to generate a higher energetic microplasma with higher electron temperatures and plasma densities. However, the limitations on the frequency range are unclear. Within the frequency capabilities of the PERL, the change in microplasma production must be understood against frequency in order to continue to determine an optimal production in microplasma. The possibility of saturation in microplasma properties exists after operating a device at a high enough frequency. This would imply that the CSRRs become frequency independent. This was observed in the modeling of electron temperature conducted by Abdel [58].

Essentially, operation of the CSRR over a frequency range including the resonant frequency can lead to a better understanding of the microplasma properties with respect to frequency for one CSRR source. It is expected that a normal distribution curve is obtained when analyzing the microplasma properties with respect to frequency with the peak existing at resonance.

4.4.2 Electron Temperature Measurements

The CSRR was able to operate at off-resonant frequencies as low as 786 MHz and as high as 806 MHz. Beyond ±10 MHz did not produce consistent plasma generation, indicating there is a limit to the off-resonant ignition. The electron temperature was determined at the three different frequencies from the double Langmuir probe data. Figure 46 displays the electron temperature data while operating the lower off-resonant frequency of 786 MHz. Figure 47 shows the electron temperature operating at resonance, 796 MHz. Figure 48 shows the electron temperature at the higher-off resonant frequency of 806 MHz. Consistently, the probe distribution plots obtained for 796 MHz and 806 MHz show a distribution exhibiting the occurrence of a secondary ignition. Corresponding to probe mapping technique, the peaks found in the distribution distribution plots seem to occur near both discharge gaps of the CSRR.

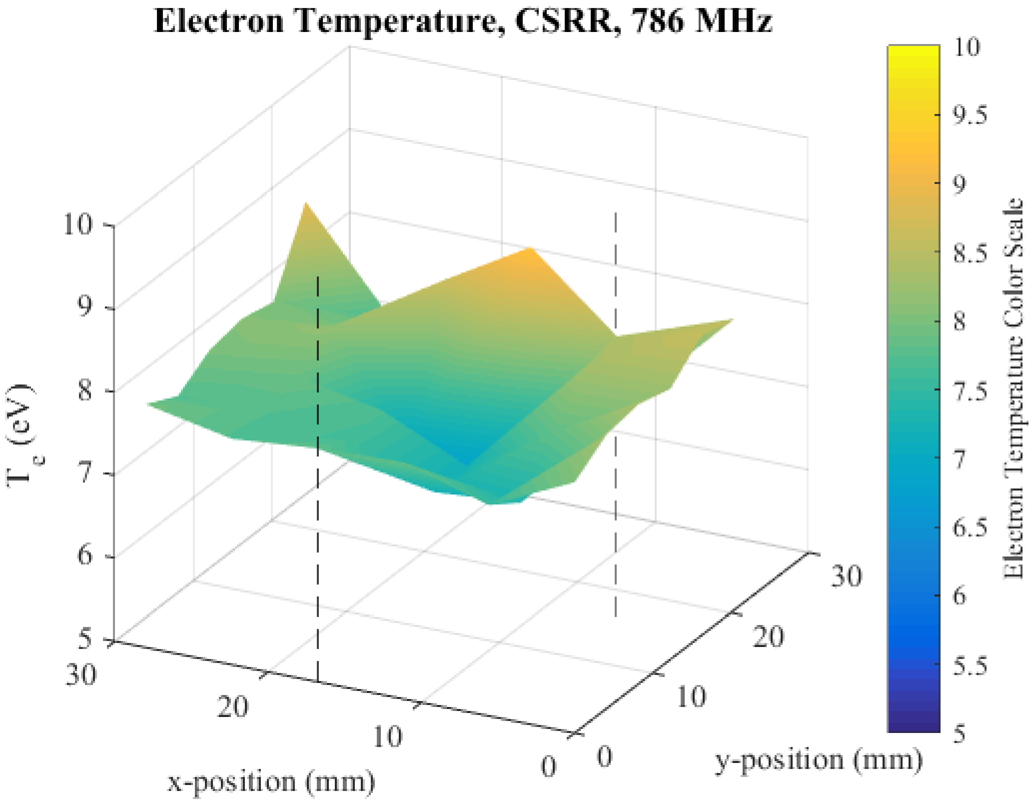

Figure 46. CSRR Electron Temperature Map at 786 MHz with ~10 W.

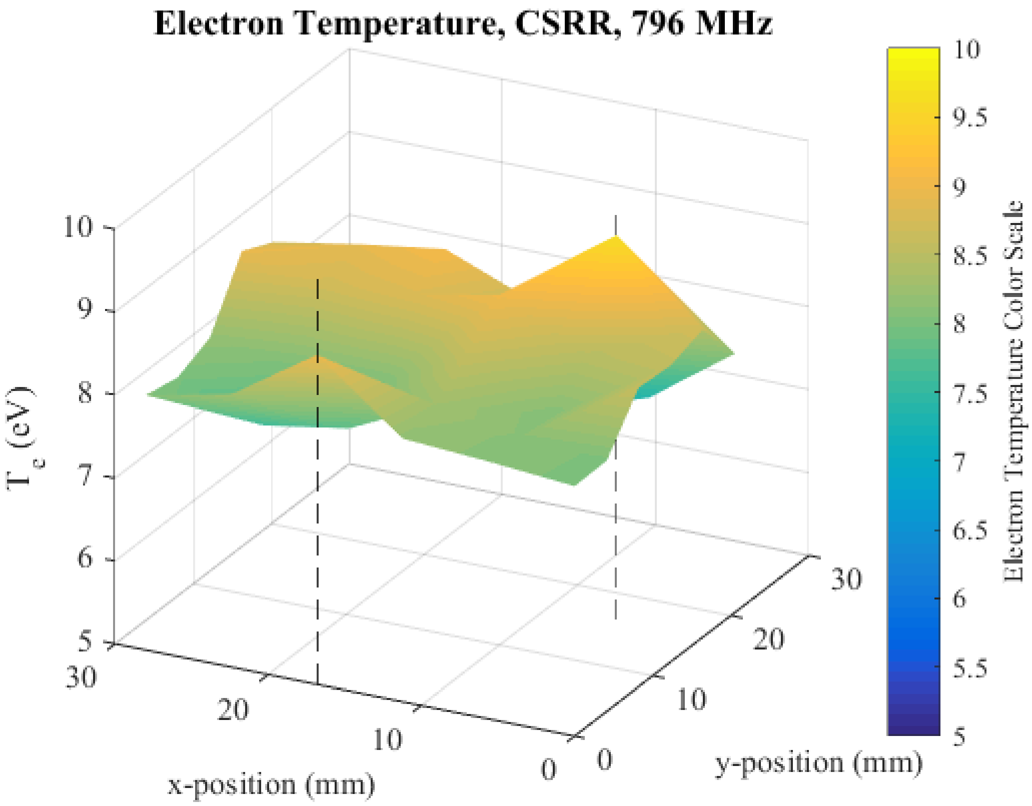

Figure 47. CSRR Electron Temperature Map at 796 MHz (resonance) with ~10 W.

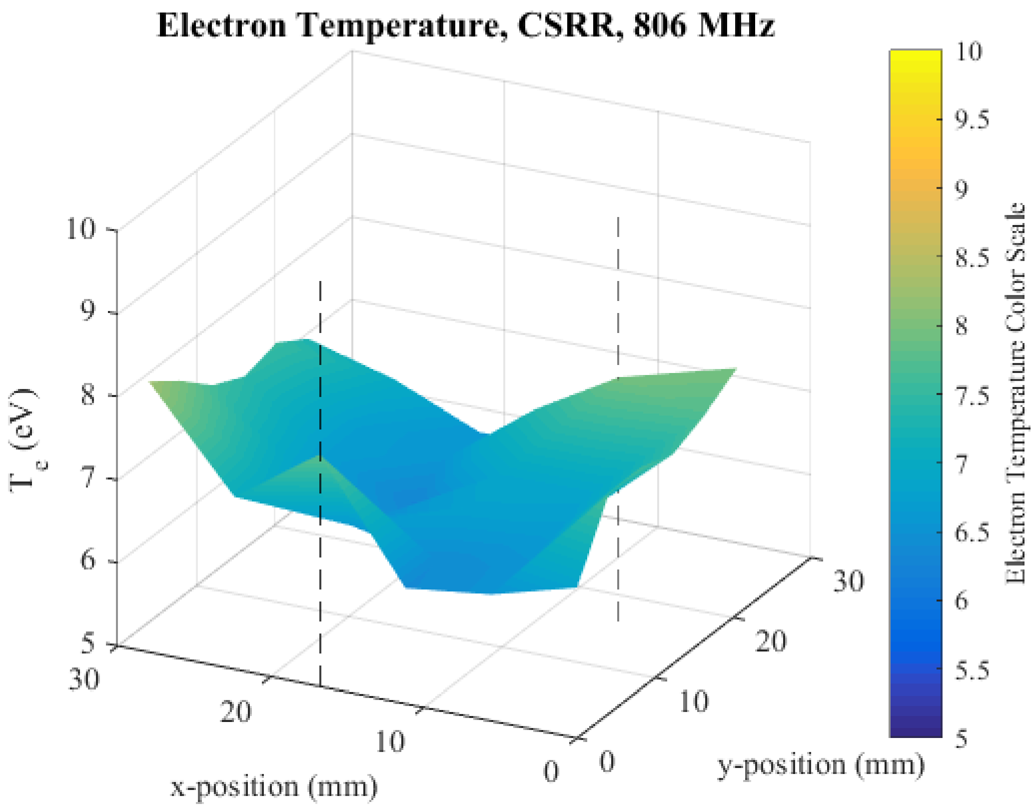

Figure 48. CSRR Electron Temperature Map at 806 MHz with ~10 W.

For 796 MHz and 806 MHz, a peak on the probe distribution map above both discharge gaps is observed. This indicates that a secondary ignition has occurred at the gap of the nested ring. At 786 MHz, the peak seemed offset from the primary discharge gap. As expected, the plasma properties measured at the secondary peaks are lower than the primary peak located at the powered ring discharge gap. It is clear, the operation at off-resonant frequencies impacts the overall plasma properties. Overall, the electron temperature decreases at off-resonant frequencies (8.5 eV @ 786 MHz, 7.6 eV @ 806 MHz and 9.5 eV at resonance).

4.4.3 Plasma Number Density Measurements

Figures 49, 50, and 51 display the plasma number density data distribution plots obtained at 786, 796, and 806 MHz respectively. The maximum plasma number density is observed to decrease as frequency increases. The peaks of the plasma density also favor the center of the device instead of the discharge gaps where an electric field is present, similar to the previous results with the CSRR.

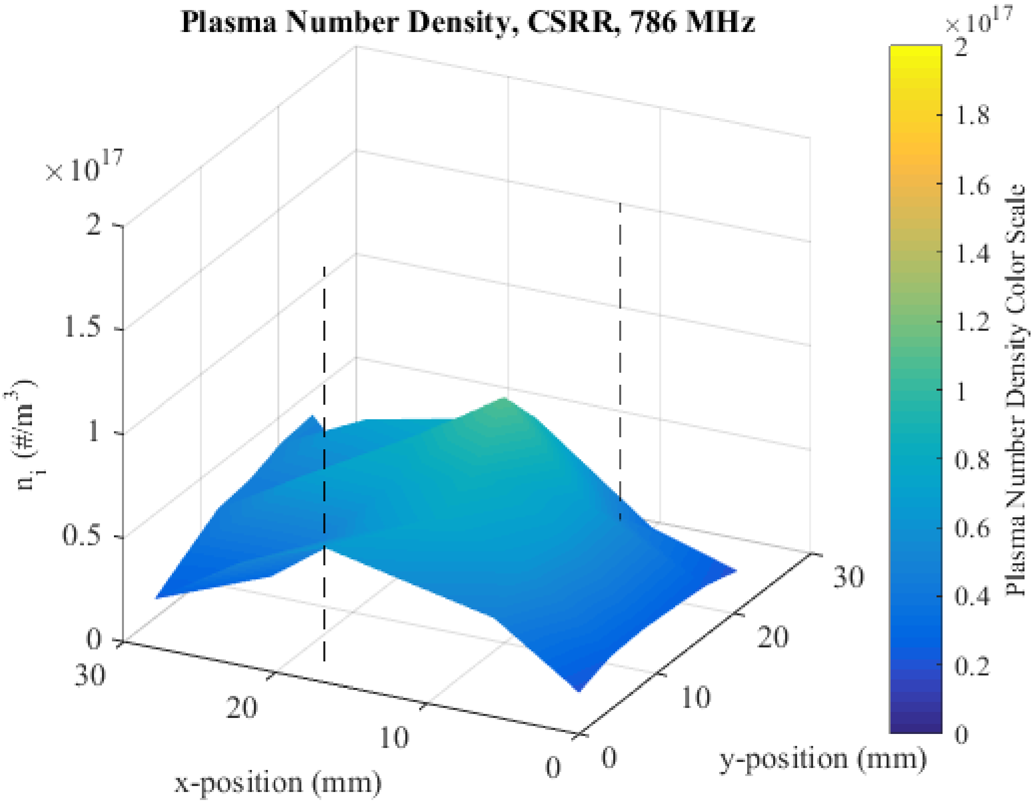

Figure 49. CSRR Plasma Number Density Map at 786 MHz with ~10 W.

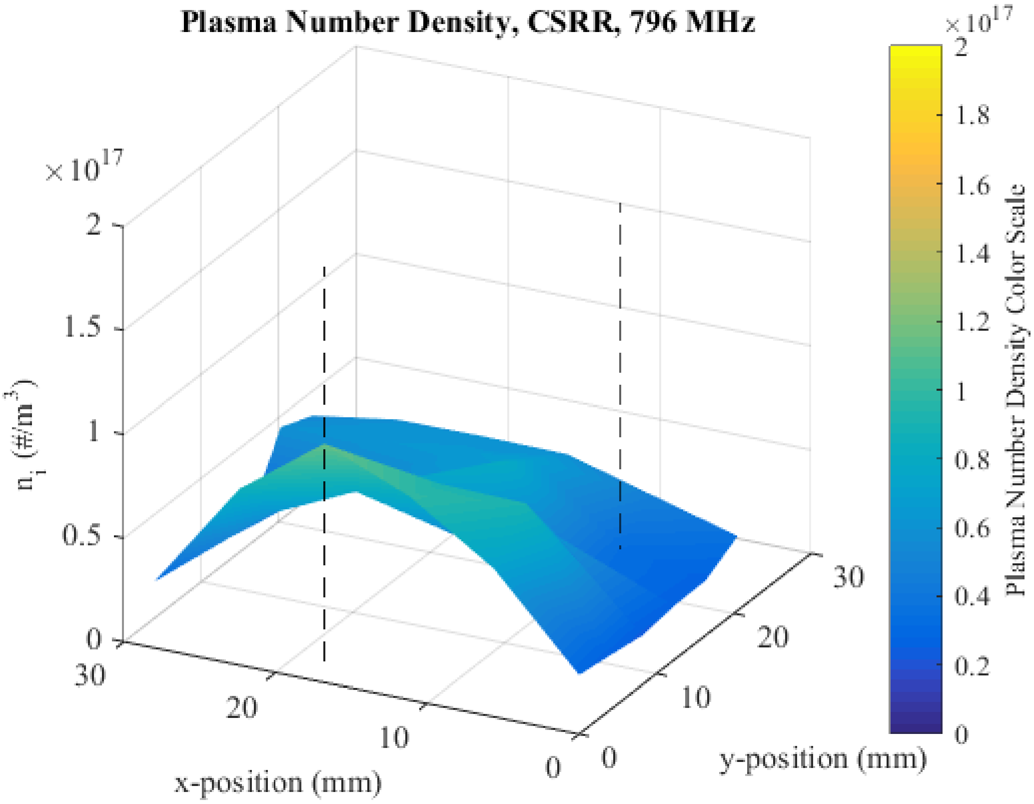

Figure 50. CSRR Plasma Number Density Map at 796 MHz with ~10 W.

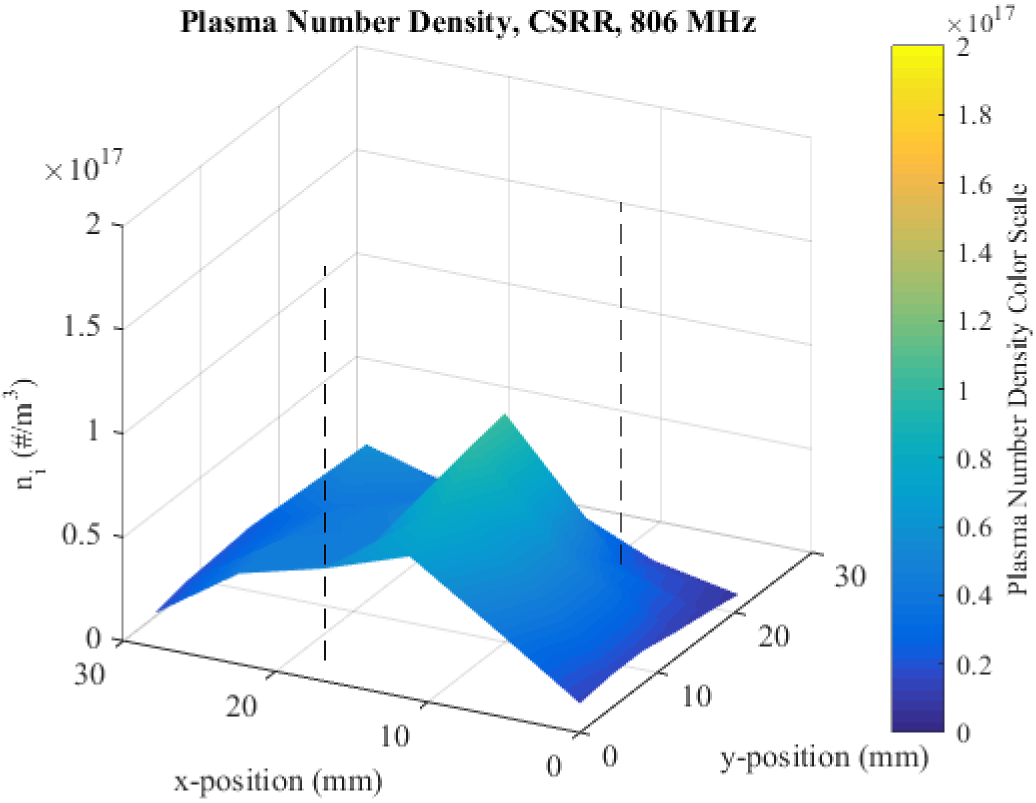

Figure 51. CSRR Plasma Number Density Map at 806 MHz with ~10 W.

According to the electron temperature plots, the higher energetic electrons are above the discharge gap. This is expected as the greatest potential change is observed at the discharge gaps of the CSRR. Lower energy electrons are likely to be found away from the discharge gap, and based on the resulting data, a larger population of lower energy particles exist compared to higher energy particles. This is apparent as the peaks of the plasma number densities are shifted from the discharge gap. Areas with higher densities yet lower electron temperatures are due to the interaction with the electric field, similarly with the fringing field vectors explained in Experiment 2. At the higher frequency, decreased plasma populations occurs due to the mismatching impedances of the microwave with the device leading to lower potential differences at the discharge gaps. This is in correlation to the measured electron temperature values. A slightly increased plasma number density is measured at the lower frequency. This signifies a presence of a larger plasma population produced by higher energy electrons near the discharge gap favoring the center of the device. This behavior is observed at the center frequency yet is not as significant as the lower frequency. With increased electron temperature results exhibiting some uniformity throughout the device, plasma number density seems to produce measurements comparable to the lower frequency near the secondary discharge gap and the center of the device. However, at the primary discharge gap, a significant drop off in plasma number density measurement occurs. Likely, this is a result of the magnetic field activity. With a change in frequency, the magnitude of the magnetic field strength changes from 9.1 G, to 11.8 G, to 15.6 G when going from 786 MHz, 796 MHz, and 806 MHz, respectively. The magnetic field strength directly impacts the electron Larmor radius as the plasma becomes magnetized. Increased B causes a decrease in the electron Larmor radius, meaning the plasma becomes pulled closer to the magnetic field lines. Varying from 9.1 to 15.6 G, the Larmor radius can change at a significant 5 mm, or about a quarter the width of the outer ring. This justifies the changes in the profiles of the plasma number densities as the operating frequency changes.

Essentially, as the frequency changes, the potential difference within the gap is impacted as the direction of the electric field emitting from the device changes. At the center frequency (resonance), opposing vectors are expected as this provides a larger potential difference near the gap. This trend continues into the lower operating frequency but not for the higher operating frequency. Understanding this begins with the mismatching impedances between the circuit and the CSRR. Mismatching impedances lead to significant reflections in the transmission line. The magnitude for the electric field vectors reduce as reflection from the device into the circuit increases. This behavior occurs as the CSRR exhibited higher impedances of 56 Ω compared to the circuit impedance of 50 Ω. Figure 52 provides an illustration on the behavior of the wave when it encounters the impedance change. The amplitude of the transmitted wave in the after-illustration is a representation of the electric field vectors.

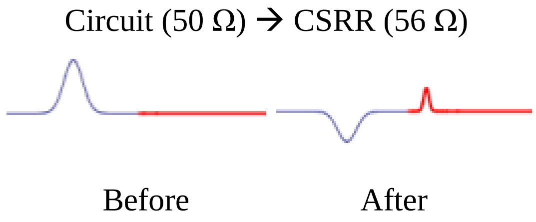

Figure 52. Illustration of impedance mismatching in transmission line from circuit (blue) to CSRR (red).

Higher reflection coefficients are also achieved by off-resonant operations [59]. As frequency is varied, a higher reflection coefficient is obtained in the higher operating frequency range compared to the lower operating frequency range, leading to the increased severity in the behavior of the electric field at 806 MHz. This severity leads to a transition from opposing vectors to unidirectional electric field vectors propagating above the CSRR. An example of varying reflection coefficients depending on frequency is also shown by Iza [6]. Figure 53 shows the reflection coefficient of Iza’s SRR. The first plot shows the behavior of reflection coefficient at wider frequency ranges. When zoomed in the second plot, an asymmetrical behavior is observed causing higher reflection coefficients at the lower operating frequency (-10 MHz) compared to the higher operating frequency (+10 MHz). This is reversed for our CSRR experiment.

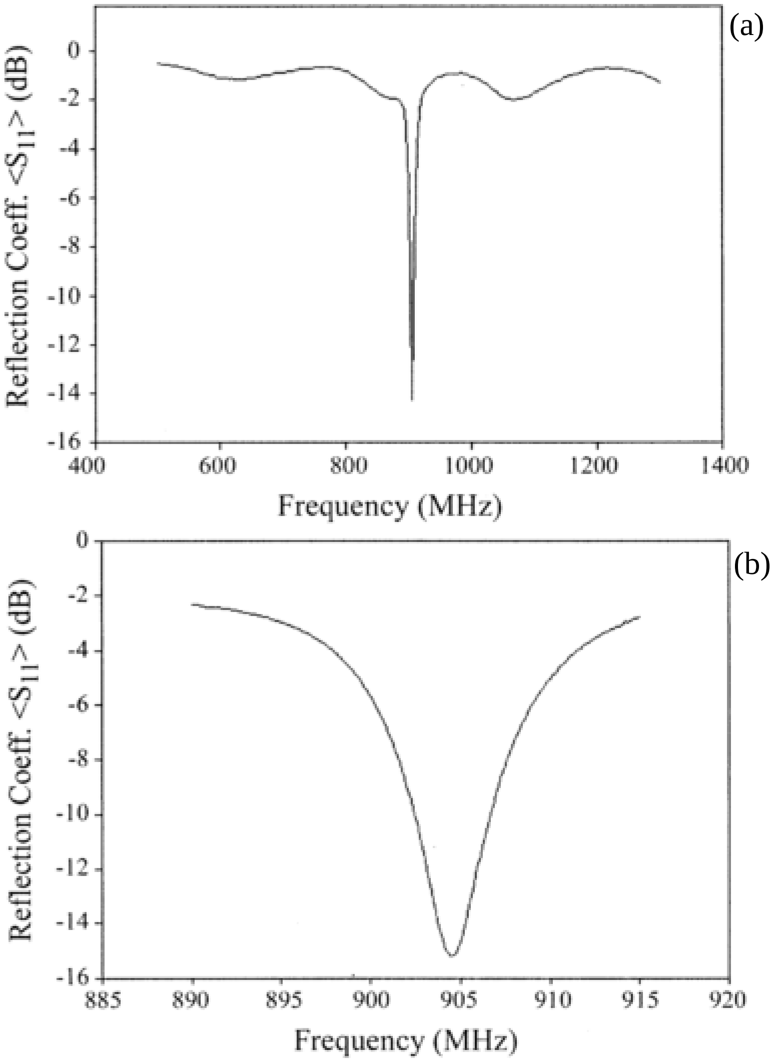

Figure 53. Reflection coefficient (s_{11}) plots produced by Iza over (a) wide frequency range, 500 to 1300 MHz and (b) narrow frequency range, 890 to 915 MHz. Measured with a HP8714ET network analyzer[6]**.**

Regardless of the unidirectional electric field vector behavior, sufficient potential difference across the discharge gap allowed ionization at 806 MHz.

Another consideration when varying frequencies are the thermal resonant and stability behaviors for oscillatory structures. These devices are subject to have a temperature coefficient that can reflect the changes in resonant frequency as temperature changes. With off-resonant frequencies, off-impedance behaviors usually lead to resistive loading such as heat on the antennas. Temperature buildups can potentially lead to resonant frequency changes. This is not including what can happen to the impedance due to natural thermal expansion in the materials. Zhang's research involved the determination of the relative temperature dependence of a dielectric's resonant frequency using parameters such as the lattice constant, dielectric constant, and magnetic permeability for microwave dielectric ceramics [60]. As long as the coefficient is at zero or near-zero, the performance of the resonator over a range of temperatures should show consistency. It is unclear if this work can be applied to microstrip resonator devices. The impact of temperature and thermal behaviors on split-ring resonators is an area that can be explored.

4.5 Microstrip Microplasma MicroThruster (3MT) Concept

With the enhanced understanding of the SRR/CSRR, theoretical application into a ion grid micropropulsion device is also feasible. Multiple concentric SRR ring with an operating frequency similar those used by communication bands can be potentially be an effective device in space propulsion. The 3MT has the potential to become a low-cost, simple solution for micropropulsion. In particular, the SRR was examined for application to a miniature ion engine. Other miniature ion engines have been designed using RF [61], [62], microwave [63], [64], and electron-impact ionization [65]. The SRR is an ideal candidate for miniature ion engine implementation due to its inherent small size and confined plasma volume. Using the electron temperature and plasma densities measured, with the assumption of a uniform temperature and density distribution, a theoretical performance for such a miniature ion engine can be calculated. The ion grid diameter is taken to be 3 cm, approximately equal to the mean diameter of the SRRs. The physical grid parameters such as aperture size, grid thickness, and grid spacing are taken from the 3 cm MiXI thruster used by Wirz [66],[4]. The aperture size for the grid sets A used by Wirz is 340 μm for the screen grid and 220 μm for the accelerator grid. The grids were developed using a 100 μm-thick molybdenum and the nominal grid spacing was 300 μm. The theoretical performance of an ion engine is given by

$$T = \gamma I_b \sqrt{\frac{2MV_b}{e}} = \gamma J_b A_g T_s \sqrt{\frac{2MV_b}{e}} \tag{26}$$

$$I_{SP} = \frac{\gamma}{g_0} \sqrt{\frac{2eV_b}{M}} \tag{27}$$

Here, T is thrust, I_{SP} is the specific impulse, I_b is the ion beam current, γ is the thrust correction factor that accounts for plume divergence and multiply charged ions, T_s is the screen grid transparency equal to 48.7% based on the MiXI screen grid, J_b is the current density, A_g is the area of the grid, M is the ion mass, and V_b is the beam voltage [4]. Ion engines typically have low plume divergence due to the grid alignment. We will assume a conservative $\gamma = 0.7$ and $V_b = 1000$ V for this analysis. The current density is obtained from the Bohm velocity ($J = 0.61 n_0 e v_B$) assuming all ions that approach the grid sheath are accelerated. The maximum thrust is produced by the 1.5 mm SRR due to its high ion density. The proposed SRR argon ion engine produces 0.18 - 0.25 mN of thrust for 4.7-11.34 W of power at a fixed 5015 seconds of specific impulse. The specific impulse is constant as it is mathematically a function of beam voltage, which is set at a constant 1000 V in this analysis.

A simple analysis was also done with a xenon plasma. A xenon SRR ion engine theoretically produces 0.21 - 0.26 mN of thrust for 4.7-11.34 W of power at a fixed 2736 seconds of specific impulse. Ion engines such as the MiXI typically use xenon as propellant. Xenon is heavier and has a lower ionization energy than argon. Thus the use of xenon with the SRR could lead to higher densities and thrust but lower specific impulse. The effect of the resonator width should have similar or greater differences for xenon as the main difference between the two species is their ionization energy, which is influenced by the gap electric field. The thrust values are comparable to the similarly sized 3 cm MiXI thruster's 0.1-1.55 mN, and the specific impulse may be comparable on the low end ranging from 1764-3184 s. Overall, the MiXi showed better thruster performance compared to an SRR ion engine. However, using the higher plasma number densities obtained from the CSRR double Langmuir probe measurements, thrust values are determined to be 1.99 mN. The calculated performance does not account for ion engine operational parameters such as perveance and net-to-voltage ratio, thus likely over predicts the real performance, especially specific impulse.

A second consideration for an SRR-based miniature ion engine is the interaction between the SRR surface electric field and the fields generated by the ion optics. In this aspect, the proposed thruster is similar to existing RF ion engines such as the European RIT [67] where the ion optics do not interfere with the plasma generation. However, instead of using an external RF coil around a dielectric chamber to generate the plasma, the SRR's "coil" is inside the chamber. This creates a greatly possibility of electrical interference, though the effect should minor as the plasma facing screen grid is typical 10-20 volts below the spacecraft and SRR potential. Thus there should only be a small electric field that is generated inside the chamber to repel electrons from the grid.

Additionally, since the SRR surface waves are mostly confined to the ring, suitable separation between the SRR and the screen grid should prevent interference.

The results indicate the use of the SRR for plasma generation can produce thrust on par with existing miniature ion engines and additionally removes the need for internal magnetic structure or a discharge cathode which is a life limiter for ion engines.

Other considerations, such as the impact on the electric field due to the grid bias voltage, has not be accounted; however, an MiXI ion engine as characterized here is expected to have no impact on the performance or microplasma production of the SRR. This is primarily due to the operations of the SRR which rely strictly on the high-frequency microwave producing a change in potential across the discharge gap confined to the device. The only known possible impact that can be induced on the microplasma of a designed SRR is the resonant frequency, input power, and reservoir pressure.

Chapter 5.

Conclusion

Research is formalized curiosity. It is poking and prying with a purpose.

– Zora Neale Hurston

This work has shown the impact of geometric and operational changes on microplasmas generated by microstrip resonator devices. Changing geometric features, such as the width of the device, and varying operational characteristics, such as frequency, leads to intriguing microplasma behaviors. The potential of generating an improved microplasma with increased plasma properties using a nested concentric ring is studied. One of the first experiments involved measuring the electron temperature and plasma number densities for these argon microplasmas from variable width SRR devices. This contributed the further understanding of microwave propagation in a ring resonator while discovering the resonant width dimension at a certain operating frequency. An example of this involves the decreasing of SRR width. Decreasing this dimension can increase characteristic impedance which leads to a decrease in quality factor due to radiation and conduction losses. Microwave propagation through a device with increased impedance relative to the microwave system can lead to increased reflection coefficients. Matching impedances between the resonator and microwave system is desirable to ensure best possible performance can be achieved. For microstrip transmission lines, an increase in strip width leads to a decrease in characteristic impedance, also impacting the plasma properties. Essentially, the SRR width plays a significant role in the resulting plasma properties and microwave behavior. This information can even lead to understandings in the behavior of the electric field intensity profiles observed by the simulations; however, the electric field is not a direct predictor of the plasma behavior.

Another study of the plasma properties of a SRR and a CSRR microplasma was conducted. The coupling effect in the CSRR is observed to be primarily induced by the fringing electric fields in proximity to the nested ring of the CSRR. This leads to the determination of the inner ring spacing for the CSRR, assigned a dimension of 1 mm to mitigate electric field coupling between the edges of the ring. The primary source of the electromagnetic coupling for the nested CSRR occurs at the discharge gap of the powered SRR as a peak electric field is achieved here when operating at resonance. With the coupling effect allowing the nested ring to behave as its own SRR, a secondary microplasma is generated at the discharge gap of the nested ring. This leads to an impact in the plasma properties. This study proved that an increase in electron temperature is observed in the CSRR compared to the SRR; however, a decrease in plasma number density occurs in the CSRR. A contribution from this CSRR research includes the ability to generate devices the multiple points of ionization potentially leading to increased plasma uniformity and plasma properties. Essentially, the ability to propagate an electric field with the utilization of space waves leading to the buildup of energy in a nested ring inducing the secondary point of ionization is a significant conclusion and contribution from this research. This feature is desirable in micropropulsion implementation.

A frequency variation study of the CSRR was conducted to understand how the microplasma changes when operating at off-resonance. Also for micropropulsion, the ability to operate over a range of frequencies is essential as a safeguard to ensure the propulsion device is not limited to one frequency. This means it is important to fully understand what performance of plasma properties to expect when operating at off-resonant frequencies. As expected, resonance leads to higher electron temperatures but some fluctuations are observed in the plasma density measurements. The lower operating frequency showed an increase in plasma density from the probe mapping data. Near the discharge gaps, higher energy electrons are found, however, increased population densities are determined favoring regions between both discharge gaps. As mentioned, with further investigation of the proximity coupling effect in CSRRs, the use of multiple nested rings and multiple points of ionization can provide plasma property uniformity. This is favorable for certain in-space micropropulsion systems. This uniformity is a trade-off for higher plasma properties only above the discharge gaps of the rings.

In review, the resonant microplasma thruster can be designed based off the knowledge we can gain from the SRR/CSRR. When considering an ionized gas flow accelerated through the device using an electric field, we will attempt to produce thrust. This concept will then be used as a basis to develop higher thrusts by reforming the SRR/CSRRs design in multiple ways. This includes adding multiple rings, changing the width of the ring, or focusing on the thickness of the microstrip on the substrate. Developing an ability to operate the device at higher frequency bands similar to communication frequencies can also prove beneficial when implementing into a spacecraft.

5.1 Future Work

With this new understanding on the microstrip microplasma generation and characteristics of the plasma properties impacted by geometrical and/or operational change in parameters, a study on the implementation of this microstrip microplasma source in micropropulsion can be achieved. Overall, this research can lead to a substantially more effective method for maneuvering and stabilizing in space when implementing this technology in micropropulsion systems for small satellites.

Knowing the microplasma from a CSRR can be produce higher plasma densities and uniform electron temperatures, electromagnetic or electrostatic acceleration mechanisms may be most effective. Due to the complexity of an electromagnetic thruster, electrostatic may be preferable. With a design of a gridded ion engine utilizing the CSRR as the plasma source, a new type of microstrip resonator microthruster can be achieved. Work involving placing this device on a torsional balance thrust stand and using the appropriate sensors can be done to obtain thrust measurements. These measurements can then be placed against the plasma densities to visually show how thrust corresponds to the plasma density. With an increased plasma density, a higher population of ions to be accelerated is expected. This theoretically implies increased thrust. With the ability to achieve certain thrust measurements that may potentially have a competitive advantage over other thrusters today, we can show how effective this low cost propulsion solution really is. In order to observe the full impact of frequency on plasma properties, a plasma volume analysis is required. With a change in microwave coupling to the CSRR, peak measurements can be obtained not only through a two-dimensional plane above the device, but throughout a three-dimensional analysis of the plasma volume. Unfortunately, this type of analysis is outside our capability.

Appendix A

Energy Delivered to the Plasma

The input power from the signal generator to the device is consistently ~10 W. An important consideration of this power delivery understands how much is needed to generate the plasma. In order to properly compare the power required to generate the plasma and the input power, we need to calculate the power of the plasma. A simple approach of $P=VI$ is utilized where the power is calculated by the voltage and the current in the discharge gap and plasma. Using the derived equations from Iza and Hopwood [6], the gap voltage is determined using the experimental parameters for quality factor and impedance. The current of the plasma is determined from the population density and the charge of the ions. Table 7 shows the parameters for both devices and how the resonator behaves when delivering the energy to the plasma.

Table 7. Input power compared to power required to generate plasma

Device	Q	Z_0 (Ω)	P_{in} (W)	V_{gap} (V)	Density (#/m^3)	Current (A)	Power (mW)
SRR	49	48.9	10	349	7.92×10^{16}	8.56×10^{-6}	0.272
CSRR	71	56	10	450	6.60×10^{16}	6.05×10^{-6}	0.321

It is observed that a higher current can be produced by the SRR due to the higher peaks in plasma number densities; however, with the high gap voltages induced by the CSRR, due to its higher quality factor, more energy is calculated to be delivered to the plasma. This higher quality factor is due to the attenuation factor of the device; which can be a representation based on input power and power losses. With the CSRR, more power is delivered to the plasma due to the improved microwave coupling caused by the change in impedance of the device.

Appendix B

Uncertainty Analysis

Conducting an uncertainty analysis to quantify the error in the data is a necessary process to verify the conclusions of this research. With each data set, there are 36 map locations in the matrix representing the distribution of plasma above the device. Three separate data sets, or 36-point sweeps, are averaged to produce the final set that was analyzed. This led to the analysis of 108 current-voltage curves (36 x 3 = 108) to determine the electron temperature and plasma number densities per experiment. The variation among the three sweeps was used to determine the uncertainty of the probe measurement. The experiments included the analysis of the SRR at 796 MHz and the CSRR at 786, 796, and 806 MHz. With a 95% confidence interval, the uncertainty quantification has been individually calculated for the SRR and the CSRR. All data sets used are obtained from the double probe theory implemented into the experimental approach.

One of the first sources observed for uncertainties is the equipment used. As each frequency was established by the signal generator or the amount of power is applied to the device, systematic error can be observed. Table 8 documents the systematic error determined from the specifications of the equipment used; including the signal generator, the Baratron capacitance pressure meter, and the stepper motor for the positioning of the double Langmuir probe.

Table 8. Systematic error from equipment used in this research.

	Systematic Error
Frequency	±500 Hz
Power	±0.001 W
Pressure	±0.025 Torr
Steps	±0.025 mm

The following tables document the percentage uncertainty analysis calculated from the three individual data sets using a 95% confidence interval.

From Tables 9-12, the equation for the 95% confidence interval used to determine the percentage uncertainty analysis is written as, $\bar{x} \pm 1.96\frac{\sigma}{\sqrt{n}}$. Here, $\bar{x}$ represents the mean, σ is the standard deviation, and n is the number of observations. Based on the information in the tables, it is observed that a varying percentage no more than 9.6% is determined. With an increase in the number of observations, this percentage uncertainty analysis is expected to decrease as an increase in samples leads to a more accurate result. Regardless, operating with a ~10% uncertainty allows us to justify our conclusions discussed in this dissertation.

Table 9. 95% Confidence Interval for CSRR plasma number density at 796 MHz.

CSRR Plasma Number Density - 796 MHz				
Point	Data	Standard Deviation	Uncertainty Analysis	Percentage
1	5.27E+16	6.94E+14	7.85E+14	1.5%
2	5.90E+16	4.69E+15	5.31E+15	9.0%
3	5.93E+16	3.35E+15	3.79E+15	6.4%
4	5.88E+16	2.69E+15	3.05E+15	5.2%
5	4.73E+16	1.30E+15	1.47E+15	3.1%
6	3.59E+16	2.19E+15	2.48E+15	6.9%
7	5.90E+16	3.92E+15	4.43E+15	7.5%
8	6.16E+16	1.96E+15	2.22E+15	3.6%
9	6.43E+16	2.49E+15	2.82E+15	4.4%
10	6.81E+16	1.27E+15	1.43E+15	2.1%
11	3.43E+16	1.06E+15	1.20E+15	3.5%
12	2.65E+16	2.04E+14	2.31E+14	0.9%
13	2.82E+16	3.59E+14	4.07E+14	1.4%
14	4.92E+16	3.39E+15	3.83E+15	7.8%
15	6.04E+16	6.94E+14	7.85E+14	1.3%
16	7.97E+16	4.25E+15	4.80E+15	6.0%
17	3.56E+16	4.90E+14	5.54E+14	1.6%
18	2.60E+16	1.84E+15	2.08E+15	8.0%
19	3.08E+16	1.06E+15	1.20E+15	3.9%
20	5.61E+16	4.78E+15	5.41E+15	9.6%
21	7.27E+16	2.99E+15	3.39E+15	4.7%
22	5.17E+16	1.78E+15	2.01E+15	3.9%
23	6.32E+16	4.70E+15	5.32E+15	8.4%
24	2.36E+16	9.39E+14	1.06E+15	4.5%
25	3.04E+16	7.06E+14	7.99E+14	2.6%
26	6.12E+16	1.31E+15	1.48E+15	2.4%
27	8.01E+16	2.45E+14	2.77E+14	0.3%
28	9.20E+16	1.80E+15	2.03E+15	2.2%
29	9.10E+16	1.14E+15	1.29E+15	1.4%
30	2.61E+16	1.06E+15	1.20E+15	4.6%
31	3.20E+16	7.76E+14	8.78E+14	2.7%
32	8.50E+16	4.29E+15	4.85E+15	5.7%
33	1.15E+17	3.67E+15	4.16E+15	3.6%
34	9.81E+16	3.23E+15	3.65E+15	3.7%
35	7.12E+16	4.90E+14	5.54E+14	0.8%
36	2.83E+16	1.27E+15	1.43E+15	5.1%

Table 10. 95% Confidence Interval for CSRR electron temperature at 796 MHz.

CSRR Electron Temperature - 796 MHz				
Point	Data	Standard Deviation	Uncertainty Analysis	Percentage
1	8.99	0.34	0.39	4.3%
2	9.02	0.63	0.71	7.8%
3	8.39	0.52	0.59	7.0%
4	8.18	0.57	0.65	7.9%
5	8.13	0.37	0.42	5.2%
6	8.35	0.16	0.18	2.2%
7	9.55	0.56	0.63	6.6%
8	8.90	0.18	0.21	2.3%
9	8.43	0.28	0.31	3.7%
10	8.10	0.29	0.33	4.1%
11	9.67	0.10	0.11	1.2%
12	8.52	0.20	0.23	2.7%
13	9.11	0.29	0.32	3.6%
14	9.15	0.19	0.21	2.3%
15	9.29	0.56	0.63	6.8%
16	9.48	0.74	0.83	8.8%
17	8.04	0.21	0.24	3.0%
18	7.68	0.37	0.42	5.4%
19	8.13	0.16	0.18	2.2%
20	7.73	0.21	0.24	3.1%
21	8.50	0.24	0.27	3.2%
22	8.46	0.62	0.70	8.3%
23	8.29	0.35	0.40	4.8%
24	8.98	0.46	0.52	5.8%
25	8.83	0.39	0.44	5.0%
26	8.85	0.52	0.59	6.7%
27	8.95	0.56	0.64	7.1%
28	9.19	0.78	0.89	9.6%
29	8.50	0.68	0.77	9.0%
30	7.82	0.31	0.35	4.5%
31	8.66	0.34	0.39	4.4%
32	9.07	0.48	0.54	6.0%
33	9.33	0.49	0.56	6.0%
34	8.51	0.22	0.25	2.9%
35	8.63	0.41	0.46	5.3%
36	7.82	0.18	0.21	2.6%

Table 11. 95% Confidence Interval for SRR plasma number density at 796 MHz.

SRR Plasma Number Density - 796 MHz				
Point	Data	Standard Deviation	Uncertainty Analysis	Percentage
1	1.86E+16	3.31E+14	3.74E+14	2.0%
2	3.18E+16	4.49E+14	5.08E+14	1.6%
3	3.89E+16	3.35E+14	3.79E+14	1.0%
4	3.49E+16	1.69E+15	1.91E+15	5.5%
5	2.25E+16	1.27E+15	1.43E+15	6.4%
6	1.25E+16	4.90E+14	5.54E+14	4.4%
7	3.19E+16	5.31E+14	6.01E+14	1.9%
8	5.48E+16	1.22E+15	1.38E+15	2.5%
9	6.67E+16	2.02E+15	2.29E+15	3.4%
10	6.85E+16	3.65E+15	4.13E+15	6.0%
11	4.22E+16	2.76E+15	3.12E+15	7.4%
12	1.86E+16	7.55E+14	8.55E+14	4.6%
13	4.28E+16	2.45E+15	2.77E+15	6.5%
14	7.76E+16	1.42E+15	1.61E+15	2.1%
15	9.42E+16	7.59E+15	8.59E+15	9.1%
16	1.27E+17	4.49E+15	5.08E+15	4.0%
17	8.60E+16	5.63E+15	6.38E+15	7.4%
18	2.97E+16	1.63E+15	1.85E+15	6.2%
19	5.34E+16	7.72E+14	8.73E+14	1.6%
20	9.83E+16	4.25E+15	4.81E+15	4.9%
21	1.12E+17	7.06E+15	7.99E+15	7.1%
22	1.74E+17	2.45E+15	2.77E+15	1.6%
23	1.39E+17	7.35E+15	8.32E+15	6.0%
24	4.31E+16	3.02E+15	3.42E+15	7.9%
25	6.50E+16	1.06E+15	1.20E+15	1.8%
26	1.05E+17	4.00E+15	4.53E+15	4.3%
27	1.12E+17	9.14E+15	1.03E+16	9.2%
28	1.76E+17	8.57E+15	9.70E+15	5.5%
29	1.61E+17	5.63E+15	6.38E+15	4.0%
30	5.21E+16	3.76E+15	4.25E+15	8.2%
31	7.12E+16	2.04E+15	2.31E+15	3.2%
32	1.09E+17	6.09E+15	6.89E+15	6.3%
33	1.14E+17	8.05E+15	9.11E+15	8.0%
34	1.66E+17	5.18E+15	5.87E+15	3.5%
35	1.52E+17	7.35E+15	8.32E+15	5.5%
36	4.84E+16	3.47E+15	3.93E+15	8.1%

Table 12. 95% Confidence Interval for SRR electron temperature at 796 MHz.

SRR Electron Temperature - 796 MHz				
Point	Data	Standard Deviation	Uncertainty Analysis	Percentage
1	8.07	0.03	0.04	0.5%
2	7.77	0.09	0.11	1.4%
3	7.75	0.01	0.01	0.1%
4	7.01	0.21	0.24	3.4%
5	7.54	0.07	0.08	1.1%
6	7.06	0.08	0.09	1.2%
7	7.96	0.03	0.03	0.4%
8	8.31	0.12	0.14	1.7%
9	7.53	0.38	0.43	5.8%
10	7.63	0.20	0.22	2.9%
11	8.34	0.32	0.36	4.4%
12	7.32	0.04	0.05	0.7%
13	7.64	0.02	0.02	0.3%
14	7.44	0.18	0.20	2.7%
15	7.31	0.37	0.42	5.7%
16	6.41	0.49	0.55	8.6%
17	7.46	0.04	0.05	0.6%
18	6.90	0.00	0.00	0.1%
19	7.20	0.06	0.07	1.0%
20	7.66	0.08	0.09	1.1%
21	7.63	0.07	0.08	1.1%
22	6.84	0.30	0.34	4.9%
23	7.22	0.13	0.15	2.0%
24	7.50	0.37	0.42	5.5%
25	8.10	0.48	0.55	6.7%
26	7.13	0.07	0.08	1.2%
27	7.95	0.38	0.43	5.4%
28	6.81	0.03	0.04	0.5%
29	6.78	0.20	0.22	3.3%
30	7.77	0.61	0.69	8.9%
31	7.71	0.39	0.44	5.8%
32	8.32	0.65	0.74	8.9%
33	8.72	0.73	0.83	9.5%
34	7.11	0.27	0.30	4.2%
35	7.17	0.48	0.55	7.6%
36	7.51	0.59	0.67	8.9%

Appendix C

Concentric Ring Discharge Gap Placement

When considering the development of the nested ring in the CSRR, it is observed that the orientation of the nested ring has been presented to be best at 180˚ from the powered ring discharge gap. This is expected as the phase angle implemented into the powered ring is intended to maximize microwave coupling from the circuit to the device. This leads to the understanding that no extra phase shift is required as the microwave propagates to the nested ring. Considering the powered ring discharge gap as the primary source of energy leading to the electric field buildup in the nested ring, the secondary discharge gap is logically 180˚ in phase with this the primary gap.

In order to check this, simulations are conducted at varying discharge gap angles, ±10˚ from 180˚. The simulations showed in Figure 54 displays the behavior of the electric field as the nested ring gap angle is impacted. With the change in gap angle, the reflection from the nested ring increases leading to an impact on the propagation of the microwave in the powered ring, decreasing the electric field intensities.

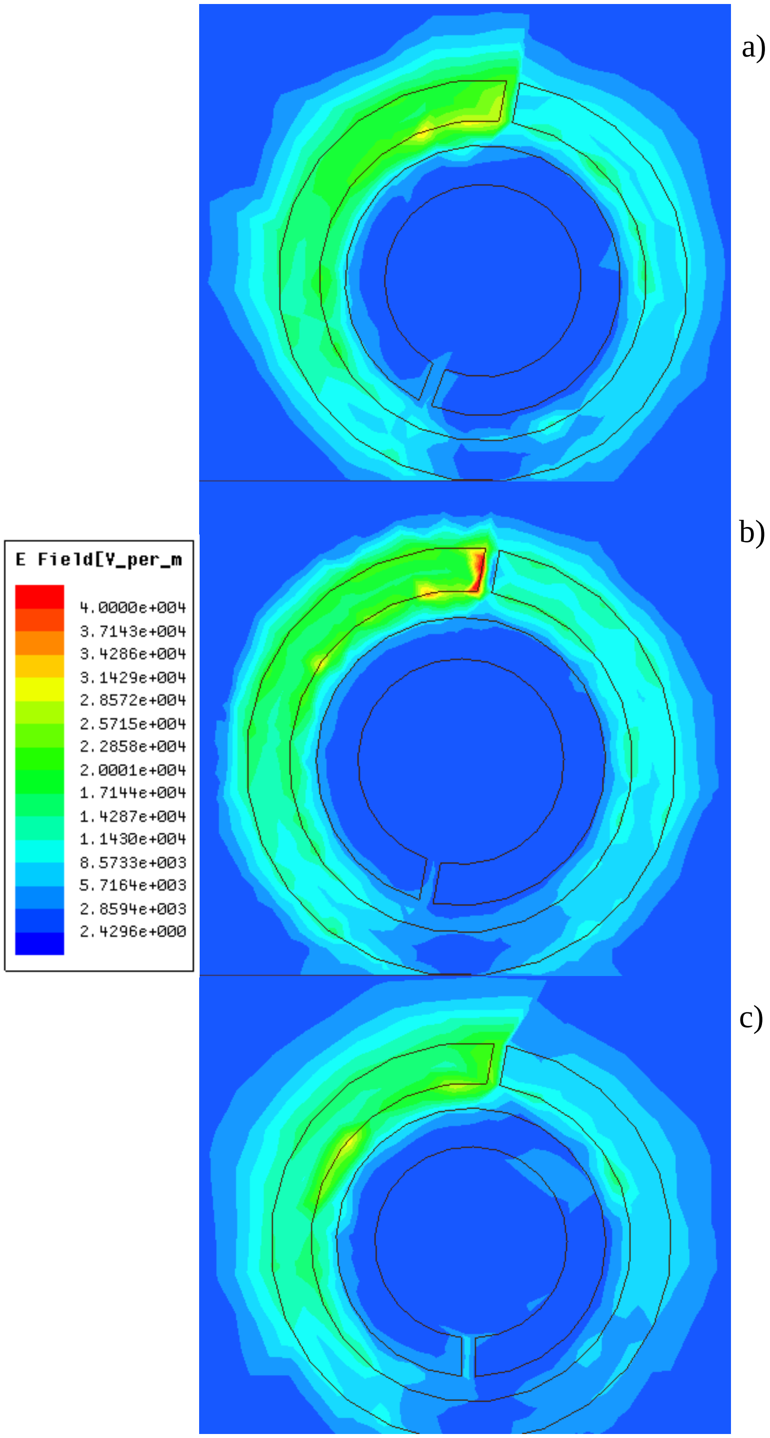

Figure 54. HFSS simulations with varying nested ring discharge gap angles. a) -10 deg, b) 0 deg, c) +10 deg.

WORKS CITED

[1] Y. Takao, T. Takahashi, K. Eriguchi, and K. Ono, “Microplasma thruster for ultra-small satellites: Plasma chemical and aerodynamical aspects,” *Pure Appl. Chem.*, vol. 80, no. 9, pp. 2013–2023, 2008.

[2] M. M. Micci, S. G. Bilén, and D. E. Clemens, “History and current status of the microwave electrothermal thruster,” *Prog. Propuls. Phys.*, vol. 1, pp. 425–438, 2011.

[3] K. G. Xu, “Micro-Propulsion Concepts Utilizing Microplasma Generators,” pp. 1–12, 2013.

[4] D. M. Goebel and I. Katz, “Fundamentals of Electric Propulsion: Ion and Hall Thrusters,” *Fundam. Electr. Propuls. Ion Hall Thrusters*, pp. 1–507, 2008.

[5] C. Williams, B. Doncaster, and J. Shulman, “2018 Nano / Microsatellite Market Forecast, 8th Edition,” 2018.

[6] F. Iza, J. A. Hopwood, S. Member, and J. A. Hopwood, “Low-Power Microwave Plasma Source Based on a Microstrip Split-Ring Resonator,” *IEEE Trans. Plasma Sci.*, vol. 31, no. 4, pp. 782–787, 2003.

[7] P. J. Castro, J. J. Barroso, and J. P. L. Neto, “Experimental Study on Split-Ring Resonators with Different Slit Widths,” *J. Electromagn. Anal. Appl.*, vol. 05, no. 09, pp. 366–370, 2013.

[8] Z.-B. Zhang and J. Hopwood, “Linear arrays of stable atmospheric pressure microplasmas,” *Appl. Phys. Lett.*, vol. 95, no. 16, p. 161502, 2009.

[9] F. Iza and J. Hopwood, “Split-ring resonator microplasma: microwave model, plasma impedance and power efficiency,” *Plasma Sources Sci. Technol.*, vol. 14, no. 2, pp. 397–406, May 2005.

[10] K. H. Becker, K. H. Schoenbach, and J. G. Eden, “Microplasmas and applications,” *J. Phys. D. Appl. Phys.*, vol. 39, no. 3, pp. R55–R70, 2006.

[11] D. Mariotti, Y. Shimizu, T. Sasaki, and N. Koshizaki, “Gas temperature and electron temperature measurements by emission spectroscopy for an atmospheric microplasma,” *J. Appl. Phys.*, vol. 101, no. 1, p. 013307, 2007.

[12] T. I. Cox, V. G. I. Deshmukh, D. a O. Hope, a J. Hydes, N. S. J. Braithwaite, and N. M. P. Benjamin, “The use of Langmuir probes and optical emission spectroscopy to measure electron energy distribution functions in RF-generated argon plasmas,” *J. Phys. D. Appl. Phys.*, vol. 20, no. 7, pp. 820–831, 2000.

[13] M. J. Kushner, “Modeling of microdischarge devices: Pyramidal structures,” *J. Appl. Phys.*, vol. 95, no. 3, pp. 846–859, 2004.

[14] A. Papadakis, S. Rossides, and A. C. Metaxas, “Microplasmas: A Review.,” *Open Appl. Phys. J.*, vol. 4, pp. 45–63, 2011.

[15] Y. V. Pan, “Micro-Scale Cell Patterning on Nonfouling Plasma Polymerized Tetraglyme Coating by Protein Microcontact Printing,” *Plasmas Polym.*, vol. 7, no. June 2002, pp. 36–43, 2002.

[16] T. Kikuchi, Y. Hasegawa, and H. Shirai, “Rf microplasma jet at atmospheric pressure: Characterization and application to thin film processing,” *J. Phys. D. Appl. Phys.*, vol. 37, no. 11, pp. 1537–1543, 2004.

[17] T. Cserfalvi, P. Mezeit, and P. Apai, “Emission studies on a glow discharge in atmospheric pressure air using water as a cathode,” *J. Phys. D. Appl. Phys.*, vol. 26, no. 12, pp. 2184–2188, 1993.

[18] D. Mariotti and R. M. Sankaran, “Microplasmas for nanomaterials synthesis,” *J. Phys. D. Appl. Phys.*, vol. 43, no. 32, p. 323001, 2010.

[19] K. Shimizu, M. Blajan, and T. Kuwabara, “Removal of indoor air contaminant by atmospheric microplasma,” *IEEE Trans. Ind. Appl.*, vol. 47, no. 6, pp. 2351–2358, 2011.

[20] Y. C. Hong and H. S. Uhm, “Microplasma jet at atmospheric pressure,” *Appl. Phys. Lett.*, vol. 89, no. 22, pp. 2004–2007, 2006.

[21] M. a. Lieberman and A. J. Lichtenberg, *Principles of Plasma Discharges and Materials Processing: Second Edition*. 2005.

[22] S. Ishii, “Microplasma as a New Science and Technology,” *IEEE Trans Fund Mater.*, no. 3.

[23] T. Yokoyama, S. Hamada, S. Ibuka, K. Yasuoka, and S. Ishii, “Atmospheric dc discharges with miniature gas flow as microplasma generation method,” *J. Phys. D. Appl. Phys.*, vol. 38, no. 11, pp. 1684–1689, 2005.

[24] C. Wu, A. R. Hoskinson, and J. Hopwood, “Stable linear plasma arrays at atmospheric pressure,” *Plasma Sources Sci. Technol.*, vol. 20, no. 4, p. 045022, 2011.

[25] J. Kim and K. Terashima, “2.45 GHz microwave-excited atmospheric pressure air microplasmas based on microstrip technology,” *Appl. Phys. Lett.*, vol. 86, no. 19, p. 191504, 2005.

[26] J. Hopwood, F. Iza, S. Coy, and D. B. Fenner, “A microfabricated atmospheric-pressure microplasma source operating in air,” *J. Phys. D. Appl. Phys.*, vol. 38, no. 11, pp. 1698–1703, Jun. 2005.

[27] M. Berglund, M. Grudén, G. Thornell, and a Persson, “Evaluation of a microplasma source based on a stripline split-ring resonator,” *Plasma Sources Sci. Technol.*, vol. 22, p. 055017, 2013.

[28] J. Gregório, L. L. Alves, O. Leroy, P. Leprince, and C. Boisse-Laporte, “Microwave microplasma sources based on microstrip-like transmission lines,” *Eur. Phys. J. D*, vol. 60, no. 3, pp. 627–635, Sep. 2010.

[29] P. Gay-balmaz, O. J. F. Martin, and I. Introduction, “Electromagnetic resonances in individual and coupled split-ring resonators,” vol. 92, no. 5, pp. 2929–2936, 2002.

[30] H. Kim, S. Parsons, and J. Hopwood, “Spatially adjustable microplasma generation in proto-metamaterials using microwave radiative power transfer,” *Plasma Sources Sci. Technol.*, vol. 27, no. 1, 2018.

[31] J. Sun, R. Wang, L. Sun, and J. Zhou, “TM-wave propagation controlled by split ring resonator array.,” *Opt. Express*, vol. 18, no. 15, pp. 15643–8, 2010.

[32] J. B. Pendry, D. Schurig, and D. R. Smith, “Controlling electromagnetic fields. Supporting info,” *Science (80-.).*, vol. 312, no. 5781, pp. 1780–1782, 2006.

[33] D. Shrekenhamer, W. Xu, S. Venkatesh, D. Schurig, S. Sonkusale, and W. J. Padilla, “Experimental realization of a metamaterial detector focal plane array,” *Phys. Rev. Lett.*, vol. 109, no. 17, pp. 24–28, 2012.

[34] P. In, “Progress In Electromagnetics Research, Vol. 142, 625–638, 2013,” vol. 142, no. July, pp. 625–638, 2013.

[35] O. Sakai, S. Yamaguchi, a. Bambina, a. Iwai, Y. Nakamura, Y. Tamayama, and S. Miyagi, “Plasma metamaterials as cloaking and nonlinear media,” *Plasma Phys. Control. Fusion*, vol. 59, no. 1, 2017.

[36] S. W. Janson, H. Helvajian, W. W. Hansen, and L. J. Lodmell, “Microthrusters for Nanosatellites,” *Int. Conf. Integr. Micro Nanotechnol. Sp. Appl. 2nd, Pasedena*, pp. 1–17, 1999.

[37] K. Nishiyama and H. Kuninaka, “Discussion on Performance History and Operations of Hayabusa Ion Engines,” *Trans. Japan Soc. Aeronaut. Sp. Sci. Aerosp. Technol. Japan*, vol. 10, no. ists28, p. Tb_1–Tb_8, 2012.

[38] L. Garrigues and P. Coche, “Electric propulsion: Comparisons between different concepts,” *Plasma Phys. Control. Fusion*, vol. 53, no. 12, 2011.

[39] J. Hopwood, A. R. Hoskinson, and J. Gregório, “Microplasmas ignited and sustained by microwaves,” *Plasma Sources Sci. Technol.*, vol. 23, no. 6, p. 064002, 2014.

[40] L. Changhong and L. Long, “A New Characteristic Impedance Perturbation Method for Finding Attentuation Constants.” 2001.

[41] P. R. Smy, “The use of Langmuir probes in the study of high pressure plasmas,” *Adv. Phys.*, vol. 25, no. 5, pp. 517–553, 1976.

[42] R. L. Merlino, “Understanding Langmuir probe current-voltage characteristics,” *Am. J. Phys.*, vol. 75, no. 12, p. 1078, 2007.

[43] T. E. Sheridan and J. Goree, “Collisional plasma sheath model,” *Phys. Fluids B Plasma Phys.*, vol. 3, no. 10, p. 2796, 1991.

[44] K. G. Xu and S. J. Doyle, “Measurement of atmospheric pressure microplasma jet with Langmuir probes,” *J. Vac. Sci. Technol. A Vacuum, Surfaces, Film.*, vol. 34, no. 5, p. 051301, 2016.

[45] C. H. Su and R. E. Kiel, “Continuum theory of electrostatic probes,” *J. Appl. Phys.*, vol. 37, no. 13, pp. 4907–4910, 1966.

[46] R. E. Kiel, “Continuum electrostatic probe theory for large sheaths on spheres and cylinders,” *J. Appl. Phys.*, vol. 40, no. 9, pp. 3668–3673, 1969.

[47] W. R. Hoegy and L. H. Brace, “Use of Langmuir probes in non-Maxwellian space plasmas,” *Rev. Sci. Instrum.*, vol. 70, no. 7, pp. 3015–3024, 1999.

[48] A. K. Horestani, C. Fumeaux, S. F. Al-Sarawi, and D. Abbott, “Split ring resonators with tapered strip width for wider bandwidth and enhanced resonance,” *IEEE Microw. Wirel. Components Lett.*, vol. 22, no. 9, pp. 450–452, 2012.

[49] S. R. Resonators, “Ring Resonators : Theory and Modeling,” 1969.

[50] F. Bilotti, A. Toscano, and L. Vegni, “Design of spiral and multiple split-ring resonators for the realization of miniaturized metamaterial samples,” *IEEE Trans. Antennas Propag.*, vol. 55, no. 8, pp. 2258–2267, 2007.

[51] B. Wu, B. Li, T. Su, and C.-H. Liang, “Study on Transmission Characteristic of Split-ring Resonator Defected Ground Structure,” *PIERS Online*, vol. 2, no. 6, pp. 710–714, 2006.

[52] F. Iza and J. a Hopwood, “a Tmospheric M Icroplasma S Ource B Ased on a M Icrostrip S Plit- R Ing R Esonator,” no. December, pp. 10–11, 2007.

[53] R. A. Dextre and K. G. Xu, “Effect of the Split-Ring Resonator Width on the Microwave Microplasma Properties,” *IEEE Trans. Plasma Sci.*, vol. 45, no. 2, pp. 215–222, 2017.

[54] X.-M. Zhu and Y.-K. Pu, “Optical emission spectroscopy in low-temperature plasmas containing argon and nitrogen: determination of the electron temperature and density by the line-ratio method,” *J. Phys. D. Appl. Phys.*, vol. 43, no. 40, p. 403001, 2010.

[55] K. Aydin, I. Bulu, K. Guven, M. Kafesaki, C. M. Soukoulis, and E. Ozbay, “Investigation of magnetic resonances for different split-ring resonator parameters and designs,” *New J. Phys.*, vol. 7, pp. 168–168, 2005.

[56] J. Hong and M. J. Lancaster, “Couplings of Microstrip Square Open-Loop Resonators for Cross-Coupled Planar Microwave Filters,” *IEEE Trans. Microw. Theory Tech.*, vol. 44, no. 12, pp. 2099–2109, 1996.

[57] M. S. Yildiz, N. Ünaldi, and M. Celik, “Geometry Optimization of a 2.45 GHz Microwave Electrothermal Thruster Resonant Cavity,” *Sp2014_2980822*, pp. 1–7, 2014.

[58] E. Abdel-Fattah and H. Sugai, “Electron heating mode transition observed in a very high frequency capacitive discharge,” *Appl. Phys. Lett.*, vol. 83, no. 8, pp. 1533–1535, 2003.

[59] D. Pozar, *Microwave Engineering Fourth Edition*. 2005.

[60] S. Zhang, H. Sahin, E. Torun, F. Peeters, D. Martien, T. DaPron, N. Dilley, and N. Newman, “Fundamental mechanisms responsible for the temperature coefficient of resonant frequency in microwave dielectric ceramics,” *J. Am. Ceram. Soc.*, vol. 100, no. 4, pp. 1508–1516, 2017.

[61] D. Feili, B. Lotz, S. Bonnet, B. K. Meyer, and H. W. Loeb, “µNRIT-2 . 5 - A New Optimized Microthruster Of Giessen University,” *Iepc2009*, no. August, pp. 1–9, 2009.

[62] T. A. Trudel, S. G. Bilen, and M. M. Micci, “Design and performance testing of a 1-cm miniature radio-frequency ion thruster,” in *31st International Electric Propulsion Conference*, 2009, pp. 20–25.

[63] D. P. Lubey, M. M. Micci, P. Taunay, U. Student, and E. Design, “Design of the Miniature Microwave-Frequency Ion Thruster,” *32nd Int. Electr. Propuls. Conf.*, pp. 1–8, 2011.

[64] H. Koizumi and H. Kuninaka, “Performance evaluation of a miniature ion thruster u1 with a unipolar and bipolar operation,” in *32nd International Electric Propulsion Conference*, 2011.

[65] R. Wirz, J. Polk, C. Marrese, and J. Mueller, “Experimental and computational investigation of the perfromance of a micro-ion thruster,” in *39th AIAA Joint Propulsion Conference*, 2002, no. AIAA-2003–4722.

[66] P. Chabert, J. Arancibia Monreal, J. Bredin, L. Popelier, a. Aanesland, T. Lafleur, K. Takahashi, C. Charles, R. W. Boswell, C. Böhm, J. Perrin, a. Aanesland, a Meige, P. Chabert, I. G. Mikellides, D. M. Goebel, J. S. Snyder, I. Katz, D. a. Herman, C. C. Wang, S. Roy, K. Takahashi, C. Charles, R. W. Boswell, T. Kaneko, R. Hatakeyama, a. Lejeune, G. Bourgeois, S. Mazouffre, F. Glass, J. Howard, B. Blackwell, a. Fruchtman, C. Charles, Y. Yasaka, A. Fukuyama, A. Hatta, R. Itatani, J. P. Boeuf, L. Garrigues, I. G. Mikellides, I. Katz, D. M. Goebel, J. E. Polk, K. K. Jameson, D. D. Blackwell, D. N. Walker, S. J. Messer, W. E. Amatucci, Y. Takao, H. Kataharada, T. Miyamoto, H. Masui, N. Yamamoto, H. Nakashima, A. Tsuji, Y. Yasaka, H. Takeno, A. Plasma, T. Co, and R. Wirz, “TOPICAL REVIEW A review of recent laboratory double layer,” *Phys. Plasmas*, vol. 14, no. 7, pp. 2652–2658, 2009.

[67] H. J. Leiter, H. J. Leiter, R. Killinger, R. Killinger, H. Bassner, H. Bassner, J. Müller, J. Müller, R. Kukies, and R. Kukies, “Development of the Radio Frequeny Ion Thruster RIT XT – A Status Report,” *Physics (College. Park. Md).*, pp. 1–8, 2001.